CWI Tracts

Centrum voor Wiskunde en Informatica
Centre for Mathematics and Computer Science
P.O. Box 4079, 1009 AB Amsterdam, The Netherlands

The CWI is a research institute of the Stichting Mathematisch Centrum, which was founded on February 11, 1946, as a nonprofit institution aiming at the promotion of mathematics, computer science, and their applications. It is sponsored by the Dutch Government through the Netherlands Organization for the Advancement of Research (N.W.O).

CWI Tract 60

Vacillation and predictability properties of low-order atmospheric spectral models

H.E. de Swart

Centrum voor Wiskunde en Informatica
Centre for Mathematics and Computer Science

1980 Mathematics Subject Classification: 34C35, 35P10, 60J70, 76C15, (76E30).
ISBN 90 6196 368 0
NUGI-code: 811

Preface

The atmospheric circulation, which possesses a finite range of predictability, seems to show vacillation behaviour: it irregularly fluctuates between three different weather regimes. In this tract a contribution is made to a better understanding of the vacillation and predictability properties of the atmosphere. This is done by considering three spectral models of the barotropic potential vorticity equation, which consists of three, six and ten components, respectively. These models are analysed by mathematical methods originating from the theory of dynamical systems. Furthermore, attention is given to the problem of how to model the effect of small-scale turbulent motions on the dynamics of the long atmospheric waves.

The investigations were supported by the Netherlands Foundation of the Technical Sciences (STW), future Technical Science Branch of the Netherlands Organization for the Advancement of Pure Research (NWO). I should like to thank my project leaders, Dr. J. Grasman and Dr. J.D. Opsteegh, for their stimulating and critical supervision. Besides, the continuous support of prof. Dr. J.T.F. Zimmerman is greatly acknowledged. My interest in the nonlinear dynamics was stimulated by Dr. E. Källen (University of Stockholm), who also read most of this manuscript carefully and critically. Dr. E.J. Doedel (Caltech, Pasadena) gave permission to use his software package AUTO to solve my bifurcation problems. Last but not least, I thank mrs. M. Middelberg and the members of the artstudio of the Royal Meteorological Institute for their assistence in preparing the text and the figures.

H.E. de Swart

CONTENTS

I. Introduction and summary

I.1. Variability of the planetary waves

The weather has a significant influence on daily life. Consequently, there is great public interest in understanding the atmospheric circulation and in weather forecasts. Although the qualitative dynamics of the circulation are nowadays rather well understood, forecasting has remained a difficult task. So far only short-range forecasts (up to a few days) are successful in the sense that they are distributed for public purposes. Nevertheless, it is well-known that occasionally substantial differences between predicted and actual flow states occur. These differences become worse when forecasts are extended to the medium and long range (weeks to months). This problem has been studied systematically by comparing output of numerical models with observed circulation patterns (Hollingsworth et al., 1980). It appears that each scale of motion has its own time scale of error growth. For example, the characteristic error-doubling time for large-scale phenomena ($\mathcal{O}(10^6 m)$) is of the order of a few days. Principal causes for this error growth were previously sought in an inaccurate specification of the initial state and in limitations of the model to incorporate correctly certain physical processes and boundary conditions. However, nowadays it is known that there is a limit to the predictability of the atmospheric circulation which cannot be enlarged by more and better observations. In order to obtain a more clear comprehension of this fundamental property we briefly describe the dynamics of the circulation.

Basically, the driving mechanism is the inhomogeneous radiation input from the sun, which causes a heat surplus in the tropical areas and a heat deficit near the poles. As can be seen from figure 1.1 these differences create a meridional temperature gradient in the midlatitudes. It is remarkable that this gradient is not present in the tropics, indicating that we have to distinguish between the dynamics in both areas. This supposition is also supported by the

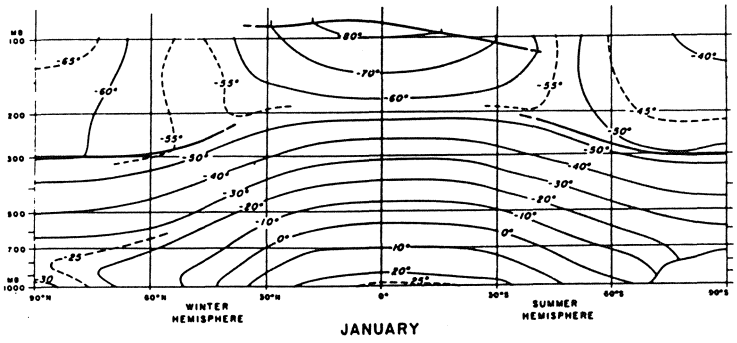

FIGURE 1.1 Mean temperature distribution, averaged around latitude circles, for January. Heavier lines show approximate mean tropopauses. From PALMÉN and NEWTON (1969).

different heights of the tropopause separating the troposphere (where vertical temperature gradients are negative) from the stratosphere (where vertical temperature gradients are positive). The difference in dynamics is to a considerable extent due to the fact that the Coriolis force (induced by the rotation of the earth) acting on a moving fluid is of minor importance in the tropics because of the earth's curvature. In low latitudes a direct convective circulation occurs: warm air is ascending near the equator, it cools and spreads out. After descending near the 30° latitudes it flows back to the equator. In midlatitudes the meridional temperature gradient gives rise to slopes of the pressure levels which would force the air to move polewards. However, globally a balance is established between the pressure gradient force and the Coriolis force, resulting in quasi-horizontally westerly winds. This so-called geostrophic balance applies to the flow outside the frictional boundary layer which is situated near the earth's surface.

From a daily weather-map it can immediately be seen that this flow is not zonally symmetric. It has a wave-like structure in which several length scales are present. In the first place we have the planetary waves with a typical length scale of 10000 km. These semi-permanent structures are forced by the thermal differences between land and ocean and the large-scale topographic variations, called the orography. In particular the Himalaya and the Rocky Mountains are important for the excitation of ultra-long waves. It appears that this planetary-scale flow is unstable: initially small perturbations may increase their amplitudes, thereby withdrawing energy from the basic flow. These disturbances, called transient eddies, appear on the weather-map as high- and low-pressure cells and are responsible for what we experience as 'weather'. They have a typical length scale of 1000 km and their life (a few days) is much shorter than that of the planetary waves (order of weeks). Place and time of the occurrence of new eddies are in general unpredictable.

Model studies have demonstrated that the geographical distribution of the planetary waves largely determines the development of and the tracks followed

by the transient eddies (FREDERIKSEN, 1983). There is also an opposite effect, as argued by OPSTEEGH and VERNEKAR (1982) and HOSKINS et al. (1983), i.e., transient eddies are capable of forcing and altering the planetary waves. The consequences for the predictability of the atmospheric circulation were systematically studied by LORENZ (1969a,b). In these studies equations are derived describing the evolution of the distribution of errors over different scales of atmospheric motion. These error equations are integrated using the observed spectral distribution of kinetic energy. It appears that, due to nonlinear interactions, arbitrarily introduced errors are transferred to all scales of motion. Furthermore, error doubling times decrease linearly when scales of motion with decreasing length scales are considered. This leads to the conclusion that the atmosphere possesses an intrinsic finite range of predictability of about two weeks.

Obviously, it is not possible to predict the actual flow state of the atmosphere over a large time interval with a sufficiently large probability. Therefore, it becomes worthwile to distinguish between weather regimes, which are clusters of states representing nearly the same flow pattern. This was for instance done by BAUR et al. (1944). They published a catalogue of large-scale atmospheric circulation patterns over Central Europe, which they called Grosswetterlagen. Later on HESS and BREZOWSKY (1969) classified these weather types into three categories: a zonal (high-index) regime with strong westerlies and small wave amplitudes, a meridional (low-index) regime with large waves embedded in a weak zonal flow and an intermediate regime of transitional type. Typical flow configurations for these regimes are shown in figure 1.2. The situation in figure 1.2c is that of a persistent anticyclone over Middle Europe, which blocks the standard passage of depressions. The dynamics of these blockings have been the subject of many recent studies, see the review in BENZI et al. (1986a). The concept of Grosswetterlagen has only regional significance. Examples of high- and low-index situations for the global atmospheric flow are discussed in PALMÉN and NEWTON (1969), DOLE (1986) and REINHOLD (1987). Although the terminology weather regimes is clear from an intuitive point of view, their existence has never been convincingly demonstrated by a systematic data analysis; only recently some indications have been found (BENZI et al. 1986b).

Once we have accepted the presence of weather regimes, the atmospheric circulation can be considered as a system which shows vacillation behaviour: it irregularly fluctuates between different preferent states. This index cycle, known to meteorologists for a long time (NAMIAS, 1950), is caused by the interactions between the quasi-stationary planetary waves and the transient synoptic-scale eddies. Within the framework of long-term weather forecasting it is important to obtain a better understanding of the dynamics responsible for this vacillatory behaviour. In this tract a contribution is made in understanding the dynamics of weather regimes by analysing the dynamical properties of highly simplified atmospheric models.

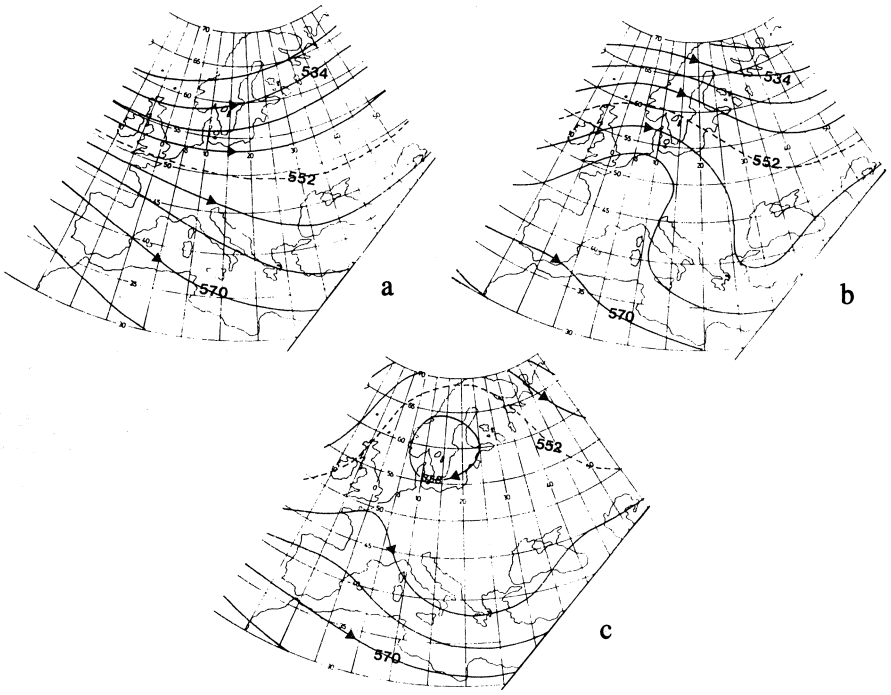

FIGURE 1.2. Geographical distribution of the height (in geopotential decameters) of the 500 mb level for the Wz (a), HM (b) and HFa (c) winter Grosswetterlagen, which are of zonal, mixed and meridional type, respectively. The isohypses are approximate streamlines of the flow; arrows indicate the flow direction. From VAN DIJK et al. (1974).

I.2. THE USE OF SPECTRAL MODELS

In order to study the variability of the atmosphere, one has in principle to consider the full equations of motion. This problem is too complicated to deal with analytically. However, WALLACE and BLACKMAN (1983) showed that the variability is mainly concentrated in the low-frequency part of the atmospheric waves (time scales of at least a few days, horizontal length scales of the order 1000 km and more). It is demonstrated in section II.1 that for these scales the equations of motion reduce to one nonlinear partial differential equation. It describes the evolution of a fundamental quantity called the quasi-geostrophic potential vorticity. Furthermore, all state variables governing the motion (velocities, temperature, pressure, density, potential vorticity) can be expressed in terms of a streamfunction. We have taken the simplest, barotropic version where we assume that the fluid has no vertical structure: it actually behaves as one layer. Some motivation for doing this follows from the observations that

the quasi-stationary atmospheric waves have a pronounced equivalent barotropic structure (BLACKMAN et al., 1979; DOLE and GORDON, 1983; BRANSTATOR, 1987).

The resulting barotropic potential vorticity equation is still difficult to handle, mainly because of its nonlinear structure. It can be studied in two different ways. A conventional method is finite difference approach. In this case the equation is considered on a grid, derivatives are replaced by finite differences and the resulting system is solved numerically. Another method is the spectral approach where explicit use is made of the boundary conditions to the potential vorticity equation. Here the streamfunction, as well as other variables depending on the spatial coordinates (topography, external forcing), are expanded in eigenfunctions of the Laplace operator. Each eigenfunction satisfies the boundary conditions and is orthonormalized with respect to the domain average. Substitution of these expansions in the potential vorticity equation yields an infinite number of coupled nonlinear ordinary differential equations, called a spectral model. It describes the time evolution of the modal amplitudes. Since in practice it is not possible to consider the dynamics in an infinite dimensional phase space, the expansions are truncated at a finite number (say N) of terms. Projecting the partial differential equation onto the resolved modes, which is called a Galerkin projection, we obtain a finite-dimensional dynamical system of the type

$$\dot{x} = f_\mu(x)+F(t) \quad \text{in} \quad \mathbb{R}^N. \tag{1.1}$$

Here a dot denotes differentiation with respect to time, $x=(x_1,x_2,...,x_N)$ represents the resolved modal amplitudes and $f_\mu(x)$ is an N-dimensional vectorfield depending on x and on parameters $\mu=(\mu_1,\mu_2,...,\mu_m)$. Furthermore the N components of vector $F(t)$ are forcing terms which describe the effect of the neglected modes on the dynamics of the resolved modes and $\mathbb{R}^N$ is the N-dimensional phase space. We also note that the original barotropic potential vorticity equation with boundary conditions is an approximation to the dynamics of the circulation. Thus, the forcing terms also account for the effect of physical processes not incorporated in the model. In that case the $F(t)$ are defined by the condition that the projection of the actual atmospheric circulation onto the N resolved modes is described by the solutions of (1.1). From a mathematical point of view spectral models can in principle be analysed with techniques originating from the theory of dynamical systems, which are discussed in GUCKENHEIMER and HOLMES (1983) and THOMPSON and STEWART (1986). As we wish to study the dynamics of the quasi-geostrophic atmospheric circulation in a systematic way, we adapt the spectral approach in this tract. Its application to the barotropic potential vorticity equation is discussed in section II.2.

In practice Eqs. (1.1) are often considered with the $F(t)$ a priori put equal to zero. Then, truncation has a similar effect as the introduction of finite differences in the sense that the small scales are removed. This is done because it this follows from observations that generally most energy is contained in only a few modes (the long waves). We argue that this may be due to an

intrinsic property of quasi-geostrophic turbulent flow: there is an energy cascade from the small scales to the larger scales (TENNEKES, 1985; PEDLOSKY, 1987). In a paper by CONSTANTIN et al. (1985) the truncation problem for the Navier Stokes equations is studied from a formal point of view. They found that for large times a finite mode expansion could be selected such that qualitative agreement is obtained with the exact solution in the sense that they have equivalent stability and attractor properties. Furthermore they showed that

$$N_s \gtrsim (kl_D)^{-d} \tag{1.2}$$

is a sufficient condition for the truncation number in order to obtain such qualitative agreement. Here k^{-1} is a typical length scale of the flow, L_D is a dissipation length scale and d the dimension of the flow. Generally N_s will be a large number, ($\mathcal{O}(10^6)$ for quasi-geostrophic motion) but we remark that (1.2) is not a necessary condition. The numerical results of FRANCESCHINI et al. (1984) for a truncated spectral model of the Navier-Stokes equations in two dimensions indicate a stabilization of qualitative behaviour at $N \sim 100$. Although it is not yet clear whether these results are applicable to the quasi-geostrophic potential vorticity equation, they at least demonstrate that truncated spectral models can be useful. In principle we would like to investigate the dynamical properties of such models. We are particularly interested in the asymptotic solutions of (1.1) (in the limit $t \to \infty$) with $F(t)=0$, in dependence of parameter values and initial conditions which are realistic for the atmosphere. However, we remark that it is not possible to carry out such an analysis systematically since the systems have a complicated dynamics due to the large number of nonlinear terms in the equations.

Therefore, as a first step, it becomes worthwhile to consider low-order spectral models, in which only a few modes are retained, and study in what sense they reflect features like transitions between weather regimes and a finitely predictable motion. An important advantage is that their properties can be analysed completely, whereas from the results indications may be found how to consider more complicated models as well as real data. It follows from (1.2) that the truncation resulting in deterministic low-order spectral models cannot be physically motivated. Nevertheless, we emphasize once more that their analysis may increase our understanding of the atmospheric dynamics.

The structure of the vectorfields studied in this tract is such that small volume elements always shrink and that solutions are bounded. Consequently, for $t \to \infty$ trajectories tend to sets of limit points with zero volume in phase space. These may include regular sets, such as stationary points (corresponding to equilibrium patterns), limit cycles (oscillating flow), invariant tori (quasi-periodically oscillating flow), as well as irregular sets which are strange attractors (chaotic flow). As discussed in section II.2 these sets of limit points are determined from a (numerical) bifurcation analysis of the spectral models. Since there are many free parameters in the problem it is necessary to use physical arguments in order to uncover their essential features. The spectral model mimics a typical characteristic of the atmospheric circulation if trajectories irregularly vacillate between different preferent regions in phase space.

Therefore, we are particularly interested in the occurrence of multiple unstable regular solutions and strange attractors. We expect trajectories to follow a strange attractor and to visit alternately regions in phase space close to the regular solutions. If on the other hand the system tends to a regular set of limit points, the truncation is apparently too severe. Thus more modes should be included in the spectral expansions in order to obtain a better representation of the atmospheric dynamics. Another possibility is to take account for the effect of small-scale eddies on the long waves. This can be done by adding specific forcing terms to the equations which provide for the occurrence of vacillation.

I.3 Review of subsequent chapters

We now discuss some previously obtained results. The fact that Galerkin projection techniques resulting in the system (1.1) can be applied to partial differential equations, collect a spectral model. It describes the dynamics of large-scale atmospheric flow was first realized by Silberman (1954). Later on a number of other spectral models have been developed, see the review in De Swart (1988). It appears that already extremely low-order deterministic spectral models show qualitative features of the atmospheric circulation. In section II.3 a three-component model, first derived by Charney and DeVore (1979), is discussed. This has either one or three equilibria, depending on the choice of parameter values. The streamfunction distributions associated with the three equilibria resemble the circulation patterns shown in figure 1.2. Based on this agreement Charney and DeVore (1979) suggest that equilibria of spectral models may indicate large-scale preferent states of the atmospheric circulation. The presence of multiple equilibria is due to a physical mechanism called topographic instability. However, no finitely predictable flow and no vacillation behaviour is obtained: the asymptotic states are always stationary. A higher-order model, consisting of six components, is studied in Charney and DeVore (1979) and Yoden (1985). The asymptotic behaviour is more complicated: apart from stationary points, periodic and chaotic orbits are found. However, no index cycles occur: solutions remain in a specific regime forever. So far the 25-component model of Legras and Ghil (1985) is the only low-order quasi-geostrophic barotropic spectral model which allows for internally generated transitions between different preferent regimes.

A different way to simulate an index cycle was proposed by Egger (1981). He added stochastic perturbations of the white-noise type to the spectral equations of the three component model They are intended to represent the influence of the neglected modes on those retained in the model. The noise forces this system to visit alternately the attraction domains of the two stable equilibria. However, no justification is given for the choice of white noise forcing. Lindenberg and West (1984) and recently Kottalam et al. (1987) have derived explicit expressions for the forcing terms in spectral models of the barotropic potential vorticity equation. They show that Eqs. (1.1) are formally a system of stochastic differential equations but the characteristics of the $F(t)$ are difficult to model. Generally, the random terms appear to be

nonstationary, nonMarkovian and nonGaussian and their intensities depend in a complicated way on the state of the system. Moreover, the $F(t)$ also contain dissipative terms which balance the rapid fluctuations. With these results in mind we formulate the following questions with respect to low-order spectral models of the barotropic potential vorticity equation:

- Which physical mechanisms are responsible for the occurrence of chaos and vacillation?
- How many modes are at least required in the spectral expansions to result in a 'minimum-order' model allowing for chaos and vacillation?
- Given this minimum-order model, what can we learn from it about qualitative and quantitative aspects of the predictability of the circulation?
- Which parametrization scheme should be chosen for the forcing terms $F(t)$ in Eqs. (1.1) in order to let this model represent a dynamics comparable to that of the circulation (a closure problem)?

In chapter III we consider the six-component model originally derived by CHARNEY and DEVORE (1979). Although it has been the subject of several studies (cf. YODEN, 1985) many of its properties are unknown. Apart from topographic instability it allows for another physical mechanism which is barotropic instability. The latter is related to the triad interaction between a zonal flow mode and two wave modes. A systematic analysis is presented of the asymptotic solutions of the model for two free parameters which control the topographic and barotropic instability mechanism, respectively. It appears that, depending on parameter values and initial conditions, the long-term behaviour can be either stationary, periodic, quasi-periodic or chaotic. A scenario is found which leads to the generation of strange attractors. It involves for specific parameter values the occurrence of homoclinic orbits which connect an unstable stationary point with itself. For nearby parameter values chaotic orbits exist which move in small tubes around the homoclinic orbits, in agreement with the theory of SILNIKOV (1965). The chaotic motion, characterized by a positive Lyapunov exponent, describes irregular flow predictable on a time scale given by the reciprocal of this exponent. However, despite its interesting properties, the model cannot represent transitions between different weather regimes. This is due to the absence of barotropic wave triads which describe interactions between three different wave modes.

Before considering a spectral model which includes a wave triad we study in chapter IV the effect of random perturbations on the three- and six-component models. In spite of the results of KOTTALAM et al. (1987) discussed previously we have taken white and coloured noise as a parametrization of the forcing terms. This choice is motivated by the results of EGGER and SCHILLING (1983, 1984) and KRUSE and HASSELMAN (1986) who showed, using atmospheric data, that the $F(t)$ in (1.1) have a coloured-noise character. A method is discussed by which analytical expressions for the expected residence times in the attraction domains of the deterministic stable equilibria are derived. It differs with respect to the one used by DE SWART and GRASMAN (1987) such that it can be applied to six-dimensional spectral models. During a transition, the system will remain for some time in a neighbourhood of an unstable equilibrium. This

indicates that unstable equilibria may have some relevance for the atmospheric dynamics. Furthermore the alternation of preferent states is studied with a discrete-state Markov model. Transition probabilities are derived from the characteristic residence times of the stochastically forced dynamical system. The eigenvalues of the master equations of the Markov model yield information about the time scale over which the effect of the initial state is present in the system.

The ten-component model discussed in chapter V can be considered as a minimum-order deterministic spectral model of the atmospheric circulation. For specific parameter values it represents a finitely predictable flow vacillating between three preferent weather regimes, which are of high-index, low-index and transitional type. This behaviour is possible on account of the presence of a wave triad which provides for a direct interaction between two distinct scales of motion: a planetary scale and a synoptic scale. In phase space the trajectories follow a strange attractor and the preferent regions are close to unstable periodic orbits of the model. The fractal dimensions of the strange attractor estimate the actual number of degrees of freedom of the chaotic flow. The reciprocal of the sum of all positive Lyapunov exponents defines a time scale on which the motion is predictable on the average. Local predictability properties are investigated by solving the linearized error equations along a principle orbit of the model. It is argued that the eigenvalues of this system determine the average error growth on a specific time interval while the corresponding eigenvectors determine the geographical distribution of the errors. Finally forcing terms, added to a six-component subsystem of the 10-component model, are calculated such that the solutions of both models are equivalent. It is found that, although these forcing terms have a stochastic nature, they cannot be parametrized by the simple processes used in chapter IV. This result is in agreement with that of KOTTALAM et al. (1987). We remark that it does not contradict the results of EGGER and SCHILLING (1983, 1984) since the latter authors also take into account the effect of physical processes not incorporated in the model.

parametrization scheme of the forcing terms				
number of components ↓	none	white noise	coloured noise	deterministic noise
3	s. II.3	Ch. IV	Ch. IV	-
6	Ch. III	Ch. IV	-	s. V.6
10	Ch. V	-	-	-

TABLE 1.1. Distribution of cases studied in this tract (s.: section, Ch.: chapter.)

Summarizing, we note in this tract three different spectral models are considered consisting of three, six and ten components, respectively. Apart from analysing their internal dynamics we have investigated the effect of different forcing terms which were added to the spectral equations in order to account for the influence of the neglected modes and physical processes. They are a white-noise forcing, a coloured-noise forcing and a forcing computed from time series of a higher-order spectral model, respectively. In table 1.1 a survey is presented of the cases studied in this tract.

A discussion about the validity of spectral models as a description of the large-scale atmospheric circulation is presented in chapter VI. It is argued that for future investigations the analysis of multi-level spectral models of the quasi-geostrophic potential vorticity equation will be useful. These models allow for the occurrence of baroclinic instability which is an important physical mechanism in the atmosphere.

II: Quasi-geostrophic motion: method of analysis

II.1. Derivation of the potential vorticity equations

In this section a simple model of the large-scale atmospheric flow will be formulated including most relevant physical processes. The derivation we shall present is based on a multiple-scale analysis and was first discussed by Pedlosky (1984). The modification introduced here is that we shall consider motions in the atmosphere instead of in the ocean, consequently the thermodynamics will be different and compressibility effects cannot be neglected a priori.

In general, the state of the atmosphere is determined by the three-dimensional velocity vector $\vec{u}$, pressure p, density ρ, temperature T and by the specific humidity, which is the mass of water vapour per unit mass of moist air. We shall start from the equations of motion neglecting humidity effects. The geometry of the earth suggests to develop the equations in spherical coordinates λ,ϕ and r, which are longitude, latitude and distance to the centre of the earth, respectively, see figure 2.1. Neglecting frictional terms for the moment, we obtain the closed system

$$\frac{du}{dt}+\frac{uw}{r}-\frac{uv}{r}\tan\phi-2\Omega\sin\phi\, v+2\Omega\cos\phi w=-\frac{1}{\rho}\frac{1}{r\cos\phi}\frac{\partial p}{\partial\lambda}, \tag{2.1a}$$

$$\frac{dv}{dt}+\frac{vw}{r}+\frac{u^2}{r}\tan\phi+2\Omega\sin\phi\, u=-\frac{1}{\rho r}\frac{\partial p}{\partial\phi}, \tag{2.1b}$$

$$\frac{dw}{dt}-\frac{u^2+v^2}{r}-2\Omega\cos\phi\, u=-\frac{1}{\rho}\frac{\partial p}{\partial r}-g, \tag{2.1c}$$

$$\frac{d\rho}{dt}+\rho\{\frac{1}{r\cos\phi}[\frac{\partial u}{\partial\lambda}+\frac{\partial}{\partial\phi}(v\cos\phi)]+\frac{\partial w}{\partial r}+\frac{2w}{r}\}=0, \tag{2.1d}$$

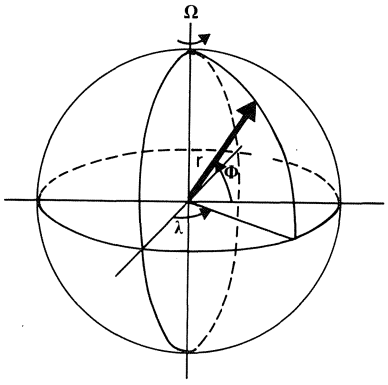

FIGURE 2.1. Spherical coordinates λ,ϕ,r for the earth.

$$\frac{d\theta}{dt}=\frac{\theta}{c_pT}H^*, \tag{2.1e}$$

$$p = \rho RT, \tag{2.1f}$$

$$\theta = T(\frac{p_r}{p})^{R/c_p}. \tag{2.1g}$$

Here

$$\frac{d}{dt}\equiv \frac{\partial}{\partial t} + \frac{u}{r\cos\phi}\frac{\partial}{\partial\lambda} + \frac{v}{r}\frac{\partial}{\partial\phi} + w\frac{\partial}{\partial r} \tag{2.2}$$

and u,v and w measure velocities in the longitudinal (zonal), latitudinal (meridional) and radial (vertical) direction, respectively. Furthermore g is the acceleration of gravity, Ω the angular speed of rotation of the earth, θ the potential temperature, H^* a heating function, p_r a prescribed reference pressure, R the gasconstant of dry air and c_p its heat capacity at constant pressure. Eqs. (2.1) are three momentum equations, a continuity equation, a thermodynamic equation, an equation of state (the ideal gas law) and the definition of potential temperature. A systematic derivation of these equations can be found in GILL (1982).

In order to analyse this system we need a priori knowledge about the particular motion to be considered. Here we shall study an atmospheric flow at midlatitudes having a vertical length scale which is much smaller than its horizontal length scale. Moreover, we assume the time scale of this flow to be large compared to the rotation period of the earth. Motivated by the qualitative description of the circulation given in chapter I, we distinguish between two different scales of motion. These are a planetary scale, with a horizontal length scale r_0 (the radius of the earth) and time scale σ_*^{-1}, and a synoptic scale with a horizontal length scale k^{-1} and time scale σ^{-1}. Both types of motion are assumed to have the same velocity scales $[u]$,$[v]$, and $[w]$ for u,v and w, respectively. They are defined as

$$[u] = \frac{\sigma}{k} = \sigma_* r_0, \quad [v]=[u], \quad [w] = \sigma H, \tag{2.3}$$

where H is the depth of the fluid. Our flow is now characterized by the conditions

$$\delta = kH \ll 1, \quad \epsilon = \frac{\sigma}{2\Omega} = \frac{[u]k}{2\Omega} \ll 1, \tag{2.4}$$

which imply a small aspect ratio and a small Rossby number, respectively. Next we introduce the following nondimensional variables:

$$\begin{aligned} &\xi = kr_0\lambda \ , \quad \eta = kr_0\phi, \quad \tilde{t} = \sigma t, \\ &\tilde{t}_* = \sigma_* t \ , \quad \tilde{z} = H^{-1}z = H^{-1}(r - r_0), \end{aligned} \tag{2.5}$$

where we assume that

$$\alpha = (kr_0)^{-1} \ll 1. \tag{2.6}$$

Then the global variation are described by functions of λ,ϕ and t_* while the variations on the synoptic scale are described by ξ,η and t. We define the nondimensional velocities $\tilde{u},\tilde{v}$ and $\tilde{w}$ as follows:

$$\begin{aligned} u &= [u]\, \tilde{u}(\lambda,\phi,t_*,z;\, \xi,\eta,t)\,, \\ v &= [v]\, \tilde{v}(\lambda,\phi,t_*,z;\, \xi,\eta,t)\,, \\ w &= [w]\, \tilde{w}(\lambda,\phi,t_*,z;\, \xi,\eta,t)\,, \end{aligned} \tag{2.7}$$

Since we are dealing with small velocities, in the sense that the Rossby number ϵ defined in (2.4) is small, pressure and density will differ only slightly from their values obtained in the absence of motion. In this rest state we have the hydrostatic balance

$$\frac{dp_s}{dz} = -\rho_s(z)g. \tag{2.8}$$

In principle any density profile can be chosen as long as

$$\frac{d\theta_s}{dz} \geqslant 0, \quad \theta_s(z) = \left(\frac{p_r}{\rho_s R}\right)\left(\frac{p_s}{p_r}\right)^{1-R/c_p}. \tag{2.9}$$

This means that the potential temperature, which is a function of ρ_s and p_s by (2.1f,g), decreases nowhere with height. Consequently the fluid is stably stratified. The pressure and density are written as

$$\begin{aligned} p &= p_s(z) + p'(\lambda,\phi,t_*,z;\, \xi,\eta,t)\,, \\ \rho &= \rho_s(z) + \rho'(\lambda,\phi,t_*,z;\, \xi,\eta,t)\,. \end{aligned} \tag{2.10}$$

The scaling for p' follows from the assumption that the Rossby number is small. It implies that the flow is quasi-geostrophic on both the planetary and synoptic scale, i.e., the horizontal momentum balance is dominated by the Coriolis and pressure gradient terms. In fact there are two different orders of pressure and density fluctuations. Here we scale p' by $2\Omega\rho_s\sigma k^{-2}$, which are

synoptic variables, and remark that pressure fluctuations on the planetary scale are a factor α^{-1} larger. The scale for the density perturbations in (2.10) is found from the hydrostatic balance which also applies to the disturbances. Thus $\rho' g$ must be of the same order as $\partial p'/\partial z$, hence it follows

$$p = p_s[1+\epsilon F\chi\tilde{p}], \quad \rho = \rho_s[1+\epsilon F\tilde{\rho}], \tag{2.11}$$

with

$$F = \frac{(2\Omega)^2 k^{-2}}{gH}, \quad \chi(z) = \frac{gH\rho_s}{p_s}(\sim 1). \tag{2.12}$$

The parameter F measures the squared ratio of the synoptic length scale of the flow to the external Rossby radius of deformation. The function $\chi(z)$ is a static density stratification parameter. To obtain the scaling for the potential temperature we eliminate T from (2.1f,g) and substitute (2.11). The result is

$$\theta = \theta_s[1+\epsilon F\tilde{\theta}], \tag{2.13}$$

where θ_s is defined in (2.9). Finally the heating function is written as

$$H^* = \epsilon F(2\Omega)c_p T\tilde{H}^*. \tag{2.14}$$

We next apply the transformations (2.3)-(2.14) to (2.1) and consider $\lambda,\phi,t_*,\xi,\eta$ and t as independent variables. Thus, derivatives in the original system are rewritten as

$$\begin{aligned} &\frac{\partial}{\partial\lambda}\to\frac{\partial}{\partial\lambda}+\alpha^{-1}\frac{\partial}{\partial\xi}\ , \quad \frac{\partial}{\partial\phi}\to\frac{\partial}{\partial\phi}+\alpha^{-1}\frac{\partial}{\partial\eta}\ , \\ &\frac{\partial}{\partial r}\to H^{-1}\frac{\partial}{\partial\tilde{z}} \qquad , \quad \frac{\partial}{\partial t}\to\alpha\sigma\frac{\partial}{\partial\tilde{t}_*}+\sigma\frac{\partial}{\partial\tilde{t}}. \end{aligned} \tag{2.15}$$

Dropping the tildes, we obtain

$$\epsilon\{\frac{du}{dt}+\alpha[\frac{du}{dt_*}+\frac{r_0}{r}(\delta uw-uv\tan\phi)]\}-\sin\phi\ v+\delta\cos\phi\ w$$
$$=\frac{-1}{(1+\epsilon F\rho)}\frac{r_0}{r\cos\phi}(\frac{\partial p}{\partial\xi}+\alpha\frac{\partial p}{\partial\lambda}), \tag{2.16a}$$

$$\epsilon\{\frac{dv}{dt}+\alpha[\frac{dv}{dt_*}+\frac{r_0}{r}(\delta vw+u^2\tan\phi)]\}+\sin\phi\ u$$
$$=\frac{-1}{1+\epsilon F\rho}\frac{r_0}{r}(\frac{\partial p}{\partial\eta}+\alpha\frac{\partial p}{\partial\phi}), \tag{2.16b}$$

$$\delta\epsilon\{\delta\frac{dw}{dt}+\alpha[\delta\frac{dw}{dt_*}-\frac{r_0}{r}(u^2+v^2)]\}-\delta\cos\phi\ u$$
$$=\frac{-1}{1+\epsilon F\rho}\{\frac{1}{\rho_s}\frac{\partial}{\partial z}(\rho_s p)+\rho\}, \tag{2.16c}$$

$$(1+\epsilon F\rho)\Big\{[\frac{r_0}{r\cos\phi}\frac{\partial u}{\partial\xi}+\frac{r_0}{r}\frac{\partial v}{\partial\eta}+\frac{1}{\rho_s}\frac{\partial}{\partial z}(\rho_s w)]$$

$$+\alpha\frac{r_0}{r}\{\frac{1}{\cos\phi}[\frac{\partial u}{\partial\lambda}+\frac{\partial}{\partial\phi}(v\cos\phi)]+2\delta w\}\Big\}$$

$$+\epsilon F[\frac{d\rho}{dt}+\alpha\frac{d\rho}{dt_*}]=0, \tag{2.16d}$$

$$\epsilon[\frac{d\theta}{dt}+\alpha\frac{d\theta}{dt_*}]+(1+\epsilon F\theta)S(z)w=\epsilon(1+\epsilon F\theta)H^*, \tag{2.16e}$$

$$1+\epsilon F\theta=\frac{(1+\epsilon F\chi p)^{1-R/c_p}}{1+\epsilon F\rho}, \tag{2.16f}$$

where

$$\begin{aligned}\frac{d}{dt}&\equiv\frac{\partial}{\partial t}+\frac{r_0}{r\cos\phi}u\frac{\partial}{\partial\xi}+\frac{r_0}{r}v\frac{\partial}{\partial\eta}+w\frac{\partial}{\partial z},\\ \frac{d}{dt_*}&\equiv\frac{\partial}{\partial t_*}+\frac{r_0}{r\cos\phi}u\frac{\partial}{\partial\lambda}+\frac{r_0}{r}v\frac{\partial}{\partial\phi},\end{aligned} \tag{2.17}$$

and the Burgers number

$$S(z)=\frac{F^{-1}}{\theta_s}\frac{d\theta_s}{dz} \tag{2.18}$$

is a stratification parameter, which is positive because of the condition (2.9). It measures the squared ratio of the internal Rossby radius of deformation and the external length scale of the flow.

In order to estimate the parameter values in (2.16) we must specify the various scales of the flow. The quasi-geostrophic atmospheric circulation at midlatitudes is characterized by $H\sim10^4m$, $k^{-1}\sim10^6m$ and $\sigma^{-1}\sim10^5s$. Furthermore, $g\sim10ms^{-2}$, $r_0\sim6.4.10^6m$, $\Omega\sim7.3.10^{-5}s^{-1}$ and $\theta_s^{-1}d\theta_s/dz\sim0.1$. Consequently, $\epsilon\sim0.1,\delta\sim0.01$, $\alpha\sim0.1,F\sim0.1$ and $S(z)\sim1$. These values suggest to analyse system (2.16) for

$$\epsilon\ll1,\ \delta=\mathcal{O}(\epsilon^2),\ \alpha=\mathcal{O}(\epsilon),\ F=\mathcal{O}(\epsilon),\ S(z)=\mathcal{O}(1). \tag{2.19}$$

Next we expand all state variables in perturbation series of a small parameter for which we choose the Rossby number ϵ. We remark that we scaled the thermodynamic variables according to the synoptic-scale variations and that fluctuations on the planetary scale are a factor α^{-1} larger. Because of (2.19) the expansions become

$$\begin{aligned}(u,v,w)&=\sum_{n=0}^{\infty}\epsilon^n(u_n,v_n,w_n),\\ (p,\rho,\theta)&=\epsilon^{-1}(p_*,\rho_*,\theta_*)+\sum_{n=0}^{\infty}\epsilon^n(p_n,\rho_n,\theta_n).\end{aligned} \tag{2.20}$$

Here u_n,v_n,w_n,p_n,ρ_n and θ_n are functions of both the planetary- and synoptic-scale coordinates. However, p_*,ρ_* and θ_* are functions of the planetary-scale coordinates (λ,ϕ,z and t_*) only, otherwise they would cause a violation of the

a priori assumed quasi-geostrophic balance. Substituting (2.19)-(2.20) in (2.16) and collecting terms with equal powers of ϵ, we obtain in lowest order

$$\sin\phi\, v_0 = \frac{1}{\cos\phi}\left[\frac{\partial p_0}{\partial \xi} + \frac{\alpha}{\epsilon}\frac{\partial p_*}{\partial \lambda}\right], \tag{2.21a}$$

$$\sin\phi\, u_0 = -\left[\frac{\partial p_0}{\partial \eta} + \frac{\alpha}{\epsilon}\frac{\partial p_*}{\partial \phi}\right], \tag{2.21b}$$

$$\frac{1}{\rho_s}\frac{\partial}{\partial z}(\rho_s p_*) + \rho_* = 0\,, \tag{2.21c}$$

$$\frac{1}{\cos\phi}\frac{\partial u_0}{\partial \xi} + \frac{\partial v_0}{\partial \eta} + \frac{1}{\rho_s}\frac{\partial}{\partial z}(\rho_s w_0) = 0\,, \tag{2.21d}$$

$$w_0 = 0\,, \tag{2.21e}$$

$$\theta_* = \left(1-\frac{R}{c_p}\right)\chi\, p_* - \rho_*. \tag{2.21f}$$

Using (2.9) and (2.21c) the expression for θ_* can be rewritten as

$$\theta_* = \frac{\partial p_*}{\partial z} - \frac{p_*}{\theta_s}\frac{d\theta_s}{dz} = \frac{\partial p_*}{\partial z}\,, \tag{2.22}$$

since $\theta_s^{-1} d\theta_s/dz = \mathcal{O}(\epsilon)$.

Eqs. (2.21a,b) state that in lowest order the Coriolis force is balanced by two horizontal pressure gradiens, which constitute the geostrophic balance at the synoptic and planetary scale, respectively. However, only three out of the four equations (2.21a,b,d,e) are independent which is a manifestation of the geostrophic degeneracy problem. In order to obtain a closed system of equations we have to consider the first-order momentum, continuity and thermodynamic equations as well. After substitution of (2.21d,e) they read

$$\frac{d_+ u_0}{dt} - \sin\phi\, v_1 = \frac{-1}{\cos\phi}\left\{\frac{\partial p_1}{\partial \xi} + \frac{\alpha}{\epsilon}\frac{\partial p_0}{\partial \lambda} - \frac{F}{\epsilon}\rho_*\left[\frac{\partial p_0}{\partial \xi} + \frac{\alpha}{\epsilon}\frac{\partial p_*}{\partial \lambda}\right]\right\}, \tag{2.23a}$$

$$\frac{d_+ v_0}{dt} + \sin\phi\, u_1 = -\frac{\partial p_1}{\partial \eta} - \frac{\alpha}{\epsilon}\frac{\partial p_0}{\partial \phi} + \frac{F}{\epsilon}\rho_*\left[\frac{\partial p_0}{\partial \eta} + \frac{\alpha}{\epsilon}\frac{\partial p_*}{\partial \phi}\right], \tag{2.23b}$$

$$\frac{1}{\rho_s}\frac{\partial}{\partial z}(\rho_s p_0) + \rho_0 = 0, \tag{2.23c}$$

$$\frac{1}{\cos\phi}\frac{\partial u_1}{\partial \xi} + \frac{\partial v_1}{\partial \eta} + \frac{1}{\rho_s}\frac{\partial}{\partial z}(\rho_s w_1) + \frac{\alpha}{\epsilon}\left\{\frac{1}{\cos\phi}\left[\frac{\partial u_0}{\partial \lambda} + \frac{\partial}{\partial \phi}(v_0\cos\phi)\right]\right\} = 0, \tag{2.23d}$$

$$\frac{d_+ \theta_0}{dt} + \frac{\alpha}{\epsilon}\frac{d_+ \theta_*}{dt_*} + \left[S(z) + \frac{\partial \theta_*}{\partial z}\right] w_1 = H^*, \tag{2.23e}$$

$$\theta_0 = (1-\frac{R}{c_p})\chi p_0 - \rho_0 - \frac{F}{\epsilon}[\rho_\star\theta_\star + \frac{R}{2c_p})\chi^2 p_\star^2], \tag{2.23f}$$

where

$$\begin{aligned}\frac{d_+}{dt} &\equiv \frac{\partial}{\partial t} + \frac{u_0}{\cos\phi}\frac{\partial}{\partial\xi} + v_0\frac{\partial}{\partial\eta}\ ,\\ \frac{d_+}{dt_\star} &= \frac{\partial}{\partial t_\star} + \frac{u_0}{\cos\phi}\frac{\partial}{\partial\lambda} + v_0\frac{\partial}{\partial\phi}\ ,\end{aligned} \tag{2.24}$$

represent the total time derivatives with respect to the total zeroth-order velocity field on the synoptic and planetary scale, respectively. An equation describing the time evolution of the zeroth-order field is obtained from differentiating (2.23b), multiplied by $(\cos\phi)^{-1}$, with respect to ξ, differentiating (2.23a) with resect to η, subtracting the results and substituting (2.23d). This yields

$$\frac{d_+}{dt}(\zeta_0 + f) \equiv \frac{d_+\zeta_0}{dt} + \beta v_0 = \frac{\sin\phi}{\rho_s}\frac{\partial}{\partial z}(\rho_s w_1), \tag{2.25}$$

with

$$\zeta_0 = \frac{1}{\cos\phi}\frac{\partial v_0}{\partial\xi} - \frac{\partial u_0}{\partial\eta}\ ,\ f = \frac{2\Omega}{\sigma}\sin(\alpha\eta)\ ,\ \beta = \frac{2\Omega\cos\phi}{\sigma k r_0}. \tag{2.26}$$

Here ζ_0 is the zeroth-order synoptic-scale relative vorticity, which is still a function of both the synoptic and planetary-scale coordinates, f is the Coriolis parameter (or planetary vorticity) and β is the gradient of f measuring the curvature of the earth. The vertical velocities in (2.25) follow from (2.23e) which can be written as

$$\frac{d_+}{dt}\frac{\partial p_0}{\partial z} + \frac{\alpha}{\epsilon}\frac{d_+}{dt_\star}\frac{\partial p_\star}{\partial z} + S(z)\, w_1 = H^\star, \tag{2.27}$$

where we have used (2.9), (2.23c,f) and the fact that $p_\star$,$\rho_\star$ and $\theta_\star$ are not functions of ξ,η and t. We have neglected the contribution $(\partial\theta_\star/\partial z)w_1$, since $\partial\theta_\star/\partial z = \mathcal{O}(\epsilon)$, as is shown in appendix A. Eqs. (2.25) and (2.27), with appropriate boundary conditions, describe the quasi-geostrophic dynamics for atmospheric motions. If (2.27) is solved for w_1 in terms of p_0 and $p_\star$, by using (2.21a,b) and (2.24), the result is

$$w_1 = w_{1s} + (\frac{\alpha}{\epsilon})w_{1c} + (\frac{\alpha}{\epsilon})^2 w_{1p}. \tag{2.28}$$

Here $w_{1s}(w_{1p})$ is the vertical velocity due to the synoptic (planetary)-scale geostrophic motion whereas w_{1c} is the contribution induced by the coupling between both scales.

In this tract we shall study a simplified type of quasi-geostrophic motion which is obtained in the limit $S(z)\to 0$. This means that the internal Rossby radius of deformation becomes small with respect to the horizontal scales of the flow. It then follows from (2.8),(2.9), (2.18), (2.21c) and (2.23c) that, at

least to $\mathcal{O}(\epsilon^2)$, density is a function of pressure only, hence the flow is barotropic. Then for $H^*=0$ (no heating) it follows from (2.27) that if p_0 and p_* are independent of z initially, they will be for all times independent of z. Furthermore we assume that the vertical velocities, which now come in due to the boundary conditions, are still of the type (2.27). Next integrating (2.25) over the depth of the fluid, substituting (2.26)-(2.27) and using (2.21a,b) as well as (2.24), we finally obtain

$$\begin{aligned}\frac{d_0}{dt}(\nabla^2\psi+f)-\int_0^1\frac{\sin\phi}{\rho_s}(\rho_s w_{1s})dz \\ +\frac{\alpha}{\epsilon}\{(\frac{-\partial p_*}{\partial\phi}\frac{\partial}{\partial x}+\frac{1}{\cos\phi}\frac{\partial p_*}{\partial\lambda}\frac{\partial}{\partial y})\nabla^2\psi \\ -\int_0^1\frac{\sin\phi}{\rho_s}\frac{\partial}{\partial z}(\rho_s w_{1c})dz\}= \\ =-(\frac{\alpha}{\epsilon})^2\sin\phi\int_0^1\{\frac{1}{\sin^2\phi}\frac{\partial p_*}{\partial\lambda}-\frac{1}{\rho_s}\frac{\partial}{\partial z}(\rho_s w_{1p})\}dz, \quad (2.29)\end{aligned}$$

where

$$\begin{aligned}\nabla &= (\frac{\partial}{\partial x}\ ,\ \frac{\partial}{\partial y})=(\frac{1}{\cos\phi}\frac{\partial}{\partial\xi}\ ,\ \frac{\partial}{\partial\eta})\ , \\ \frac{d_0}{dt}&=\frac{\partial}{\partial t}-\frac{\partial\psi}{\partial y}\frac{\partial}{\partial x}+\frac{\partial\psi}{\partial x}\frac{\partial}{\partial y}\ ,\qquad \psi=\frac{p_0}{\sin\phi}.\end{aligned} \quad (2.30)$$

Note that d_0/dt is the total time derivative with respect to the zeroth-order synoptic-scale velocity field, which is determined by the streamfunction ψ. Eq. (2.29) is written in such a way that its right-hand side contains contributions which depend on the planetary-scale coordinates λ,ϕ,z and t_* only. If this term were nonzero it would act as a constant forcing term on the synoptic-scale vorticity balance on the left-hand side of (2.29), ψ would grow linearly with time and consequently the geostrophic regime would break down. In order to avoid secular behaviour the r.h.s. of (2.29) must be zero and the result is two separate equations:

$$\begin{aligned}\frac{d_0}{dt}(\nabla^2\psi+f)-\int_0^1\frac{\sin\phi}{\rho_s}\frac{\partial}{\partial z}(\rho_s w_{1s})dz-\underbrace{\frac{\alpha}{\epsilon}\int_0^1\frac{\sin\phi}{\rho_s}\frac{\partial}{\partial z}(\rho_s w_{1c})dz}_{(2)} \\ +\underbrace{\frac{\alpha}{\epsilon}\left[\frac{-\partial p_*}{\partial\phi}\frac{\partial}{\partial x}+\frac{1}{\cos\phi}\frac{\partial p_*}{\partial\lambda}\frac{\partial}{\partial y}\right]}_{(1)}\nabla^2\psi=0, \quad (2.31a)\end{aligned}$$

$$\frac{1}{\sin\phi}\frac{\partial p_*}{\partial\lambda}-\int_0^1\frac{\sin\phi}{\rho_s}\frac{\partial}{\partial z}(\rho_s w_{1p})dz=0. \quad (2.31b)$$

They describe the quasi-geostrophic vorticity balances for barotropic motions on the synoptic and planetary scale, respectively. Obviously they are derived simultaneously by a multiple-scale analysis. If terms (1) and (2) are neglected in (2.31a) this equation shows that the total time derivative of the absolute vorticity ($\nabla^2\psi+f$) is affected by small vertical velocities. This equation follows directly from Eqs. (2.1) by a priori using a time scale σ^{-1}, a horizontal length scale k^{-1} and taking the limit $S(z)\to 0$. For $(\alpha/\epsilon)=\mathcal{O}(1)$ additional contributions are present which couple the two scales of motion. The terms (1) describe the advection of synoptic-scale relative vorticity by the planetary-scale geostrophic velocities. The terms (2) represent the effect of synoptic-scale vorticity stretching by divergence of the planetary-scale velocity field. Eq. (2.31b) describes a balance between the advection of planetary vorticity and the stretching of planetary vorticity by divergence of the planetary-scale velocity field. This equation could be obtained from system (2.1) by introducing the time scale σ_*^{-1} and horizontal length scale r_0. Note that the planetary-scale dynamics is not affected by synoptic-scale motions.

From now on we will a priori neglect all motions on the planetary scale and consider the synoptic-scale motions only. The boundary conditions for this type of flow are derived in PEDLOSKY (1987) and read for the barotropic case

$$\int_0^1 \frac{\sin\phi}{\rho_s}\frac{\partial}{\partial z}(\rho_s w_{1s})dz = \underset{(1)}{-\gamma\frac{d_0 h}{dt}} \underset{(2)}{-C\nabla^2\psi} \underset{(3)}{+C\nabla^2\psi^*}\,, \tag{2.32}$$

with

$$\gamma = \frac{fh_0}{H}\,,\quad C = \frac{f\delta_E}{2H}\cdot \tag{2.33}$$

They describe the modification of the flow at the lower boundary due to the presence of topography (1), frictional effects (2) and due to some external forcing streamfunction ψ^*(3) which for example models the equator-pole temperature gradient. Here $z=h$ is the position of the lower boundary with characteristic amplitude $h_0(\ll H)$ and δ_E is the thickness of the frictional (Ekman) boundary layer situated near the earth's surface. Substituting (2.32) in (2.31a), in which we neglect the terms (1) and (2), we arrive at

$$\frac{\partial}{\partial t}\nabla^2\psi + J(\psi,\nabla^2\psi+f)+\gamma J(\psi,h)+C\nabla^2(\psi-\psi^*) = 0\,, \tag{2.34}$$

where

$$J(A,B) = (e_z\times\nabla A)\cdot\nabla B \tag{2.35}$$

is the Jacobian of A and B with e_z a unity vector in the radial direction. Eq. (2.34) is the quasi-geostrophic barotropic potential vorticity equation for synoptic-scale motions. In many studies, including the present tract, it is used as a model for the dynamics of the atmospheric circulation.

II.2. SPECTRAL ANALYSIS FOR BAROTROPIC FLOW ON A BETA PLANE

It is discussed by DUTTON (1974) that the quasi-geostrophic potential vorticity equation can be investigated by means of spectral analysis. Here we apply this technique to its barotropic version: consider Eq. (2.34) on a domain D with appropriate boundary conditions. We look for solutions by expanding the streamfunctions ψ and ψ^*, as well as the topography h, in a series of eigenfunctions $\{\phi_j\}_j$ of the Laplace operator:

$$(\psi,\psi^*,h) = \sum_j (\psi_j,\psi_j^*,h_j)\phi_j, \tag{2.36}$$

where

$$\nabla^2\phi_j + \lambda_j\phi_j = 0, \quad j=(j_1,j_2). \tag{2.37}$$

The eigenfunctions have positive eigenvalues λ_j, satisfy the boundary conditions and are orthonormalized with respect to the domain average. It can be verified that

$$\psi = \phi_j e^{-i\omega t} \tag{2.38}$$

is a solution of (2.34) when $\gamma=C=\psi^*=0$ (no topography, dissipation and external forcing), provided

$$\omega = \frac{-\beta j_1}{\lambda_j}, \tag{2.39}$$

where β is defined in (2.26). Eq. (2.39) is the dispersion relation of a free westward propagating Rossby wave (PEDLOSKY, 1987). Note that a single wave satisfies the full nonlinear equation. Thus, application of the spectral technique to the barotropic potential vorticity equation yields a streamfunction expanded in the free Rossby modes of the equation.

Projecting (2.34) on these eigenfunctions, called a Galerkin projection, we obtain the spectral equations

$$\lambda_j\dot{\psi}_j = \frac{1}{2}\sum_l\sum_m c_{jlm}(\lambda_l-\lambda_m)\psi_l\psi_m + \gamma\sum_l\sum_m c_{jlm}\psi_l h_m + \sum_l b_{jl}\psi_l - C\lambda_j(\psi_j-\psi_j^*). \tag{2.40}$$

This system describes the time evolution of the expansion coefficients $\{\psi_j\}_j$. Here

$$c_{jlm} = <\phi_j, J(\phi_l,\phi_m)> , \quad b_{jl} = <\phi_j, J(\phi_l, f)>, \tag{2.41}$$

with

$$<A,B> = \int_D A\, B^{cc}\, d\vec{r} \Big/ \int_D d\vec{r} \tag{2.42}$$

defining an inproduct on D and cc denoting a complex conjugate. The interaction coefficients in (2.41) obey the relations

$$c_{jlm} = c_{lmj} , \quad c_{jlm} = -c_{jml} , \quad b_{jl} = -b_{lj} , \tag{2.43}$$

where the second one has already been used in the derivation of (2.40). Details of the spectral method are discussed in GOTTLIEB and ORSZAG (1977) and VOIGT et al. (1984). Using the completeness property of the eigenfunctions they show the existence and unicity of the spectral solution on a bounded domain.

In order to analyse Eqs. (2.40) we should consider the dynamics in an infinite-dimensional phase space. This cannot be realized for practical applications. A convenient way to deal with this problem in fluid dynamics is to approximate the streamfunction in (2.36) by an expansion in which j may run only through a finite number (say N) of values:

$$\tilde{\psi} = \sum_j \psi_j \phi_j \quad , \quad j_l \leqslant j \leqslant j_u \, . \tag{2.44}$$

This convention implies that we consider a rectangular truncation in the (j_1, j_2) space. Projecting the partial differential equation on these eigenfunctions we obtain a finite-dimensional dynamical system of the type (1.1) where $x = \{\psi_j\}_{j=j_l}^{j=j_u}$.

We finally consider the energetics of the spectral model. Defining

$$K = \tfrac{1}{2} < \nabla\psi, \nabla\psi > = -\tfrac{1}{2} < \psi, \nabla^2\psi > = \tfrac{1}{2} \sum_j \lambda_j \psi_j^2 \tag{2.45}$$

as the mean barotropic kinetic energy, we derive an equation for K by multiplying (2.34) with ψ and next averaging over the domain D. The result is

$$\dot{K} = -2CK + C < \nabla\psi, \nabla\psi^* > . \tag{2.46}$$

Note that in the absence of forcing and dissipation ($\psi^* = C = 0$) the kinetic energy is a constant of motion. Eq. (2.46) also holds for truncated spectral models of the barotropic potential vorticity equation where j in (2.45) runs through only a finite number of values.

The fact that Galerkin projection techniques can be applied to partial differential equations describing the dynamics of large-scale atmospheric flow was first realized by SILBERMAN (1954). In this paper Eq. (2.34) is considered without the effects of topography, dissipation and external forcing ($\gamma = C = \psi^* = 0$). The streamfunction is expanded in orthonormal eigenfunctions of the Laplace operator on the sphere, which are spherical harmonics in this case.

However, we remark that the quasi-geostrophic potential vorticity equation is not valid over the whole sphere because horizontal length scales should be small compared to the radius of the earth. As an alternative SALTZMAN (1959) introduced a channel approximation in which Eq. (2.34) is considered in a circular strip at midlatitudes, see figure 2.2. This approach has the problem that artificial boundary conditions are required at the two walls. The spectral method has been applied to both barotropic and baroclinic quasi-geostrophic motion as well as to nongeostrophic models, see the review in DE SWART (1988). Both types of geometry discussed above are frequently used.

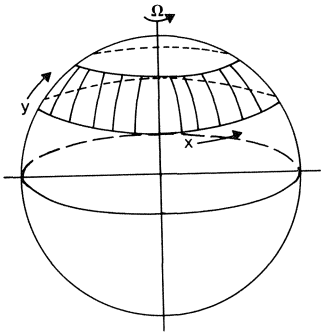

FIGURE 2.2. The midlatitude channel. The x-coordinate is along lines of constant latitude, the y-coordinate along lines of constant longitude.

Here we consider a barotropic flow in a rectangular channel on the beta plane, i.e., β in (2.26) is considered to be a constant. The channel has length 2π in the zonal x-direction and width πb in the meridional y-direction, hence

$$k = \frac{2\pi}{L} \ , \quad b = \frac{2B}{L} \ , \tag{2.47}$$

with B and L the dimensional width and length of the channel. We investigate the existence of travelling wave solutions in the x-direction. At the boundaries $y=0$ and $y=\pi b$ the meridional velocity component is assumed to be zero. Furthermore the circulation around the boundaries should be a constant. The resulting boundary conditions for the streamfunction are derived by PHILLIPS (1954). They lead to the following eigenvalue problem:

$$\begin{aligned} &\nabla^2\phi_j+\lambda_j\phi_j = 0 \ \text{ on } \ \{(x,y)|0\leqslant x\leqslant 2\pi,\ 0\leqslant y\leqslant \pi b\} \ , \\ &\phi_j(x+2\pi,y) = \phi_j(x,y) \ , \\ &\frac{\partial\phi_j}{\partial x} = 0 \text{ and } \int_0^{2\pi}\frac{\partial\phi_j}{\partial y}dx = 0 \ \text{ at } \ y=0 \ \text{ and } \ y=\pi b \ , \\ &<\phi_j,\phi_l>\equiv\frac{1}{2\pi^2 b}\int_0^{\pi b}\int_0^{2\pi}\phi_j\phi_l^{cc}\,dxdy = \delta_{jl} \ . \end{aligned} \tag{2.48}$$

Here cc denotes a complex conjugate and δ_{jl} a Kronecker delta function. Solutions of (2.48) are obtained by the method of separation of variables. The resulting eigenfunctions, with corresponding eigenvalues, are

$$\phi_j(y) = \sqrt{2}\,\cos(j_2\frac{y}{b}) \ , \ \lambda_j = \frac{j_2^2}{b^2} \ , \tag{2.49a}$$

$$\phi_j(x,y) = \sqrt{2}e^{ij_1x}\sin(j_2\frac{y}{b}) \ , \ \lambda_j = j_1^2+\frac{j_2^2}{b^2} \ . \tag{2.49b}$$

$|j_1|,j_2=1,2,...$

The eigenfunctions in (2.49a) are $(0,j_2)$ modes which describe zonal flow profiles. The solutions (2.49b) are $(|j_1|,j_2)$ Rossby waves. The interaction coefficients, defined in (2.41), for these modes are presented in appendix B. It appears that there are two types of nonlinear interactions. The first type involves a zonal flow mode and two Rossby waves, while the second type involves three wave modes. The latter are called barotropic wave triads. Furthermore, it appears that many nonlinear interactions do not lead to resonant coupling. The underlying physical mechanism is discussed in PEDLOSKY (1987).

The motivation to study low-order spectral models has already been discussed in chapter I and will not be repeated here. We derive a particular low-order model by including only the (0,1) (0,2), (1,1), (1,2), (2,1) and (2,2) modes. These are two zonal flow profiles and four Rossby waves, respectively. We assume that external forcing, due to the equator-pole temperature gradient, only acts upon the zonal flow modes. Furthermore

$$h = \cos(x)\,\sin(\frac{y}{b})\,, \tag{2.50}$$

i.e., the topography is given as a (1,1) mode, being the longest wave present in the model. Defining the real variables

$$\begin{aligned}
x_1 &= \frac{\psi_{01}}{b} \quad , \quad x_1^* = \frac{\psi_{01}^*}{b} \quad , \\
x_2 &= \frac{1}{b\sqrt{2}}(\psi_{11}+\psi_{-11}) \quad , \quad x_3 = \frac{i}{b\sqrt{2}}(\psi_{11}-\psi_{-11}) \quad , \\
x_4 &= \frac{\psi_{02}}{b} \quad , \quad x_4^* = \frac{\psi_{02}^*}{b} \quad , \\
x_5 &= \frac{1}{b\sqrt{2}}(\psi_{12}+\psi_{-12}) \quad , \quad x_6 = \frac{i}{b\sqrt{2}}(\psi_{12}-\psi_{-12}) \quad , \\
x_7 &= \frac{1}{b\sqrt{2}}(\psi_{21}+\psi_{-21}) \quad , \quad x_8 = \frac{i}{b\sqrt{2}}(\psi_{21}-\psi_{-21}) \quad , \\
x_9 &= \frac{1}{b\sqrt{2}}(\psi_{22}+\psi_{-22}) \quad , \quad x_{10} = \frac{i}{b\sqrt{2}}(\psi_{22}-\psi_{-22}) \quad ,
\end{aligned} \tag{2.51}$$

we arrive at the 10-coefficient model given in appendix C. It contains a six-dimensional subsystem, denoted by the dashed lines. For $x_4^*=0$ (no forcing in the (0,2) mode) it is further reduced to the three-component model between the dotted lines. These three models will be studied for their physical and mathematical properties. More specifically, we will investigate whether these models reflect characteristics of the atmospheric circulation such as a finite predictability and vacillation behaviour. This occurs if the asymptotic solutions of the spectral model (i.e., the solutions in the limit $t\rightarrow\infty$) irregularly visit different preferent regions in phase space. The techniques we shall apply to analyse the models originate from the theory of dynamical systems. A brief overview of the mathematical details is presented in appendix D.

II.3. THREE COMPONENTS: A REVIEW

So far only the three-component model, given in appendix C between the dotted lines, has been analysed completely. It is the simplest nontrivial spectral model of the atmospheric circulation, describing the interaction of a (0,1) zonal flow mode and a (1,1) Rossby wave. In order to study the properties of the nonlinearities explicitly we first neglect the effect of forcing and dissipation ($x_1^* = C = 0$). The stationary points $\hat{x} = (\hat{x}_1, \hat{x}_2, \hat{x}_3)$ of this model, obtained by setting all time derivatives equal to zero (see appendix D), satisfy

$$\hat{x}_2 = \frac{\gamma_{11}\hat{x}_1}{\alpha_{11}\hat{x}_1 - \beta_{11}}, \quad \hat{x}_3 = 0, \tag{2.52}$$

for arbitrary $\hat{x}_1$. Since $\hat{x}_3 = 0$ the wave is in phase with the topography. The stability of the equilibria is investigated by considering the dynamics of small perturbations on these states. They evolve as $\exp(\lambda t)$, where λ are the eigenvalues of the matrix derivative of the vector field, linearized at $\hat{x}$. In this case the characteristic equation reads

$$\lambda \left[\lambda^2 + (\alpha_{11}\hat{x}_1 - \beta_{11})^2 - \frac{\gamma_{11}\gamma_{11}^*\beta_{11}}{\alpha_{11}\hat{x}_1 - \beta_{11}} \right] = 0 . \tag{2.53}$$

A stationary point is unstable if there is at least one eigenvalue with a positive real part. In (2.53) this is the case if

$$0 < \alpha_{11}\hat{x}_1 - \beta_{11} < (\gamma_{11}\gamma_{11}^*\beta_{11})^{1/3}. \tag{2.54}$$

Note that instabilities can only occur for γ nonzero. For this reason the mechanism is called topographic instability (CHARNEY and DEVORE, 1979). In the limit $(\alpha_{11}\hat{x}_1 - \beta_{11}) \to 0$ the wave amplitude grows resonantly. This is due to a continuous vorticity transfer from the zonal flow to the wave mode where topography acts as a catalyst. This transfer is not compensated for by advection of total vorticity because the zonal flow velocity balances the phase speed of the Rossby wave.

Next we introduce zonal forcing and dissipation. Then stationary points are found from a cubic equation:

$$\begin{aligned} &\hat{x}_1^3 + a_2\hat{x}_1^2 + a_1\hat{x}_1 + a_0 = 0 , \\ &\hat{x}_2 = \frac{\gamma_{11}\hat{x}_1(\alpha_{11}\hat{x}_1 - \beta_{11})}{(\alpha_{11}\hat{x}_{11} - \beta_{11})^2 + C^2}, \quad \hat{x}_3 = \frac{-C\gamma_{11}\hat{x}_1}{(\alpha_{11}\hat{x}_1 - \beta_{11})^2 + C^2}, \end{aligned} \tag{2.55}$$

where

$$\begin{aligned} a_2 &= \frac{-(2\beta_{11} + \alpha_{11}x_1^*)}{\alpha_{11}}, \quad a_1 = \frac{2\alpha_{11}\beta_{11}x_1^* + \beta_{11}^2 + \gamma_{11}\gamma_{11}^* + C^2}{\alpha_{11}^2}, \\ a_0 &= -(\beta_{11}^2 + C^2)\alpha_{11}^{-2}x_1^*. \end{aligned} \tag{2.56}$$

From the kinetic energy equation (2.46) it follows that always $0 \leqslant \hat{x}_1 \leqslant x_1^*$.

Thus $\hat{x}_3<0$, which implies that the phase difference between the stationary wave and the topography is always negative. As can be seen from (2.55), due to dissipation the topographic resonance has shifted to small but nonzero values of $(\alpha_{11}\hat{x}_1-\beta_{11})$. Furthermore, there may be either one or three real stationary points. The bifurcation set, which is the set of parameter values at which a transition from one to three equilibria occurs, is given by

$$q^3+r^2=0,\quad q=\tfrac{1}{3}a_1-\tfrac{1}{9}a_2^2,\quad r=\tfrac{1}{6}(a_1a_2-3a_0)-\frac{1}{27}a_2^3. \tag{2.57}$$

The stationary points at the bifurcation set are turning points of the bifurcation diagram. For these parameter values the wave becomes topographically unstable. In the region where (q^3+r^2) is negative, called the catastrophe set, three real stationary points occur.

The stability of the stationary points is determined from the eigenvalues of the matrix derivative of the vector field linearized at $\hat{x}$. The characteristic equation reads

$$\begin{aligned}
&(\lambda+C)^3+b_1(\lambda+C)+b_0=0\\
&b_1=(\alpha_{11}\hat{x}_1-\beta_{11})^2-\gamma_{11}\gamma_{11}^*\left[\frac{\beta_{11}(\alpha_{11}\hat{x}_1-\beta_{11})-C^2}{(\alpha_{11}\hat{x}_1-\beta_{11})^2+C^2}\right],\\
&b_0=\frac{-C\gamma_{11}\gamma_{11}^*\alpha_{11}\hat{x}_1(\alpha_{11}\hat{x}_1-\beta_{11})}{(\alpha_{11}\hat{x}_1-\beta_{11})^2+C^2}.
\end{aligned} \tag{2.58}$$

From (2.55) and (2.58) it follows that if the system has only one real stationary point it is stable. If there are three real stationary points two of them are stable and one is unstable. Furthermore it can be shown that complex eigenvalues do not have vanishing real parts, hence there are no Hopf bifurcation points in the model. The only possibility for a real eigenvalue to pass through zero is at the bifurcation set.

As a specific example we consider a channel of length 4900 km and variable width around the central latitude $\phi=45°$. The vertical length scale is taken to be $H=10^4m$ and the time scale $\sigma^{-1}=10^5s$, such that $f=10$. It then follows for the model parameters $\beta=1.25$, the value of b depends on the channel width (see (2.47)), γ measures the topography amplitude in km, C^{-1} a dissipation time scale in days and $x_1^*=U/U_0$. Here U is a velocity scale for the external forcing and $U_0=\sigma/k=7.8ms^{-1}$. We take $\gamma=1, C=0.1$ and vary x_1^*. In the literature the model has also been studied for different parameter values, see the review in De Swart (1988). The results of these investigations do not differ significantly from those which will presented here. In figure 2.3a the bifurcation set of the model in the b,x_1^*-parameter space, enclosing the catastrophe set, is shown. It is known as a cusp catastrophe. In figure 2.3b the equilibrium solution component $\hat{x}_1$, which represents the nondimensional intensity of the zonal flow, is presented as a function of the external forcing x_1^* in case $b=1.6$ (channel-width 3920 km). The x_1-component is proportional to

the zonal index since it measures the eastward transport between the two meridional channel walls.

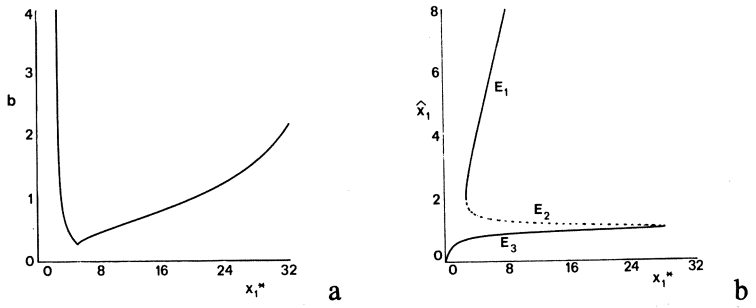

FIGURE 2.3a. Bifurcation set in the b,x_1^*-parameter space of the three-component model for fixed β,γ and C.

b. The x_1-component of the stationary points as a function of x_1^* for $b=1.6$ and fixed β,γ and C. A solid line denotes that the solution is stable, a dashed line denotes an unstable solution.

For large x_1^* ($\geqslant 28.107$) there is one stable stationary point E_1. For smaller forcing values ($2.741 \leqslant x_1^* \leqslant 28.107$) two more stationary points appear. The intermediate one (E_2) is unstable, since it has one positive real eigenvalue, while the lower one (E_3) is stable. For small x_1^* ($\leqslant 2.741$) one stable stationary point (E_3) is left. To show the characteristic circulation patterns of the equilibria we have taken $x_1^* = 4$ (zonal-forcing velocity amplitude of $31.7 ms^{-1}$). Then three equilibria exist with the numerical values

$$E_1 = (3.829,\ 0.428,\ -0.018)\,,\quad E_2 = (1.477\,,\ 0.989,\ -0.263),$$
$$E_3 = (0.776,\ -0.768,\ -0.336). \tag{2.59}$$

Their nondimensional streamfunction patterns are shown in figure 2.4. The stationary point E_1 represents a high-index state with a strong westerly flow and a small wave amplitude. Furthemore, E_3 is a low-index state representing a large wave embedded in a weak zonal flow. Finally, E_2 is an intermediate state showing characteristics of the two equilibria discussed previously.

In figure 2.5 a projection of trajectories onto the $x_1 - x_2$ plane is shown for the case of three real stationary points. Initial conditions are taken in a plane $x_3 =$ constant. It appears that most trajectories tend to one of the stable equilibria. Exceptions are those which lie on the separatrix between the attraction domains of E_1 and E_3, which tend to E_2. The separatrix has a complicated structure and its geometry can only be approximated by a large number of time integrations of the system. As concluded by CHARNEY and DEVORE (1979), the presence of topography is a necessary condition for the existence of multiple equilibria: the unstable equilibrium E_2 is due to topographic instability. Furthermore, these authors argue that the flow patterns of the stable equilibria E_1 and E_3 resemble large-scale preference states of the atmospheric circulation. This is motivated by the qualitative resemblance between the

circulation patterns of the Grosswetterlagen, shown in figure 1.2, and those of the equilibria of the spectral model, presented in figure 2.4. KÄLLÉN (1981, 1982) has drawn similar conclusions for a three-component model of the barotropic potential vorticity equation on a sphere.

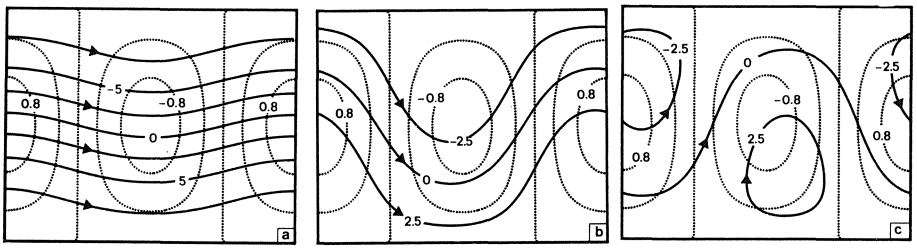

FIGURE 2.4. Nondimensional streamfunction contours (solid lines) for the equilibria $E_1(a), E_2(b)$ and $E_3(c)$ defined in (2.59). A difference $\Delta\psi = 1$ corresponds to a zonal transport of about $1.1.10^6 m^2 s^{-1}$. Arrows indicate the flow direction. The dashed lines represent contours of topography (km).

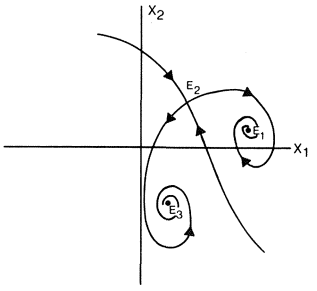

FIGURE 2.5. Sketch of the phase flow of the three component-model, projected onto the $x_1 - x_2$ plane in case there are three equilibria. Initial conditions are chosen in a plane $x_3 =$ constant.

The model is unrealistic in the sense it always ends up in a stationary point. Thus, we conclude that, although there is some qualitative agreement, the three-component model does not give a realistic picture of the time evolution of large-scale atmospheric flow. It therefore becomes useful to include more modes and study its consequences for the solutions as $t \to \infty$. This brings us to a six-component model, which will be the subject of the next chapter.

III. Analysis of a six-component model of the atmospheric circulation

III.1 Preliminary remarks

It is clearly indicated by synoptic observations that the atmospheric circulation has an irregular temporal and spatial structure. This suggests that complicated models are needed to describe adequately the evolution of the flow. The structure of general circulation models and weather forecast models confirms this idea (Jarraud and Baede, 1985). Although these models are successful in simulating the flow, they do not provide much insight into the underlying dynamics. It is therefore significant to investigate whether it is possible to construct more simple nonlinear models which reflect specific features of the atmospheric circulation. By the latter we mean a flow vacillating between different weather regimes and of which the evolution can only be predicted for a finite amount of time. As discussed more extensively in chapter I we study in this tract truncated spectral models of the barotropic potential vorticity equation in a beta plane channel. They are of the type (1.1) and can be analysed with techniques originating from dynamical systems theory. We are particularly interested whether such a system, without the effect of the forcing terms $F(t)$ in (1.1), contains a strange attractor with a multimodal probability distribution on it. Since the associated chaotic motion is characterized by sensitive dependence on the initial conditions it models a finitely predictable flow. The multimodal probability distribution implies that trajectories alternately visit different preferent regions in phase space, as required to obtain an index cycle.

In section II.3 it has been found that the three-component model of appendix C between the dotted lines possesses multiple equilibria for a wide range of parameter values. The corresponding circulation patterns resemble the weather regimes of high-index, low-index and transitional type discussed in chapter I. However, no vacillation behaviour is obtained: all nontransient solutions

appear to be stationary. This result suggests to study the effect of including more modes in the spectral expansions. This naturally leads to the six-component model given in appendix C between the dashed lines. It describes the interaction between two zonal flow modes and two Rossby waves. It was originally derived by CHARNEY and DEVORE (1979) and is also considered in MATSUDA (1983), YODEN and HIROTA (1984) and YODEN (1985). A spherical analogon is discussed in KÄLLÉN (1981, 1982). Although these studies answered many questions, our knowledge of the model is still incomplete. For example, the existence of vacillation behaviour has not been investigated yet. Therefore, in the present chapter a detailed analysis is given of the physical and mathematical properties of the six-component model.

First we note that the spectral equations are invariant under the transformation

$$(x_1,x_2,x_3,x_4,x_5,x_6,x_1^*,x_4^*) \rightarrow (x_1,\ x_2,\ x_3,-x_4,-x_5,-x_6,x_1^*,-x_4^*). \tag{3.1}$$

This implies that, in case $x_4^*=0$ (no forcing in the second zonal harmonic), if initial conditions are chosen such that $x_4(0)= x_5(0) =x_6(0) =0$, the evolution will be governed by the three-component model discussed in section II.4. Furthermore, the increased number of degrees of freedom allows for a new physical mechanism, called barotropic instability mechanism. It may occur in the triad interaction between the (0,2), (1,1) and (1,2) mode. FJØRTOFT (1953) showed that such a triad conserves kinetic energy as well as enstrophy (squared relative vorticity). Next he derived a necessary condition for a participating mode to become unstable: its wave-length must be smaller than that of the second participating mode and larger than that of the third one. Applying this theorem to the triad of the six-component model we find

$$\begin{aligned} &\text{if } b^2<3: \text{ (0,2) mode can become unstable,} \\ &\text{if } b^2>3: \text{ (1,1) mode can become unstable.} \end{aligned} \tag{3.2}$$

Thus the width-length ratio of the channel controls the barotropic instability mechanism.

The stationary solutions and their stability properties are studied in section III.2 as a function of two parameters. Apart from b the external forcing, controlling the topographic instability mechansim, is varied. The existence of strange attractors is investigated in the sections III.3 and III.4 by continuing in parameter space branches of periodic orbits which bifurcate from branches of stationary points. In some cases the periodic orbits become homoclinic, such that they connect a stationary point with itself. For nearby parameter values strange attractors occur, in agreement with the theory developed by SILNIKOV (1965). However, although the six-component model has interesting properties, it is of limited validity for the atmospheric circulation. It appears that the strange attractors only have a small attraction domain in phase space, such that chaotic trajectories remain in a specific regime forever. Physically, this is due to the presence of only one resonant barotropic triad so that the number

of possible nonlinear interactions is limited. It is argued in section III.5 that more degrees of freedom are needed in order to obtain vacillation behaviour.

III.2 Stationary solutions and their bifurcations

We now study the steady states of the six-component model. For the moment we take $x_4^* = 0$. Then, because of (4.1), equilibria of the three-component model are also equilibria of the six-component model with $\hat{x}_4 = \hat{x}_5 = \hat{x}_6 = 0$; they are called single-mode equilibria. However, their stability may change due to presence of more modes. It can be shown that the characteristic equation, which is of sixth degree, factorizes into two cubic equations describing the stability with respect to the first-mode and second-mode perturbations, respectively. According to the Fjørtoft theorem, equilibrium E_1 cannot become barotropically unstable because it is characterized by a large (0,1) component having the smallest wave-number of the spectrum. The possible instability of E_2 and E_3 with respect to second-mode perturbations leads to additional mixed-mode equilibria, for which $\hat{x}_4$, $\hat{x}_5$, $\hat{x}_6 \neq 0$, as well as periodic solutions. Charney and Devore (1979) showed that the mixed-mode equilibria are governed by

$$\begin{aligned} &d_2(\hat{x}_1)\hat{x}_4^4 + d_1(\hat{x}_1)\hat{x}_4^2 + d_0(\hat{x}_1) = 0 , \\ &e_2(\hat{x}_1)\hat{x}_4^4 + e_1(\hat{x}_1)\hat{x}_4^2 + e_0(\hat{x}_1) = 0 , \end{aligned} \tag{3.3}$$

where d_2, d_1, d_0, e_2, e_1 and e_0 are known functions of $\hat{x}_1$. Furthermore, for each $\hat{x}_1$ and $\hat{x}_4$ we obtain a unique $\hat{x}_2$, $\hat{x}_3$, $\hat{x}_5$ and $\hat{x}_6$. Since (3.3) is two quadratic equations for $\hat{x}_4^2$ we conclude that mixed-mode equilibria always occur in pairs having the same $\hat{x}_1$, $\hat{x}_2$ and $\hat{x}_3$ component, but opposite $\hat{x}_4$, $\hat{x}_5$ and $\hat{x}_6$ components.

The equilibria and their stability properties were calculated for the parameter values $\beta = 1.25$, $C = 0.1$, $\gamma = 1$, $x_4^* = 0$ and variable b and x_1^*. The physical conditons are identical to those discussed in section II.4 for the three-component model. In figure 3.1 curves in the (b, x_1^*) parameter space are shown. The solid lines, labelled L_1, L_2 and L_3, are curves of turning points (saddle-node bifurcations). The dashed lines are curves of pitchfork bifurcation points and the dotted lines, labelled $H1$, $H2$ and $H3$, are curves of Hopf bifurcation points. Definitions of equilibria, bifurcations etc. are given in appendix D.

At the turning points and bifurcation points two different branches of equilibria come together. Consequently, the associated curves in figure 3.1 divide the parameter space into regions, each with its own characteristic number of equilibria. This is denoted by the symbols a_s, a_m, where a_s gives the number of single-mode equilibria and a_m the number of mixed-mode equilibria.

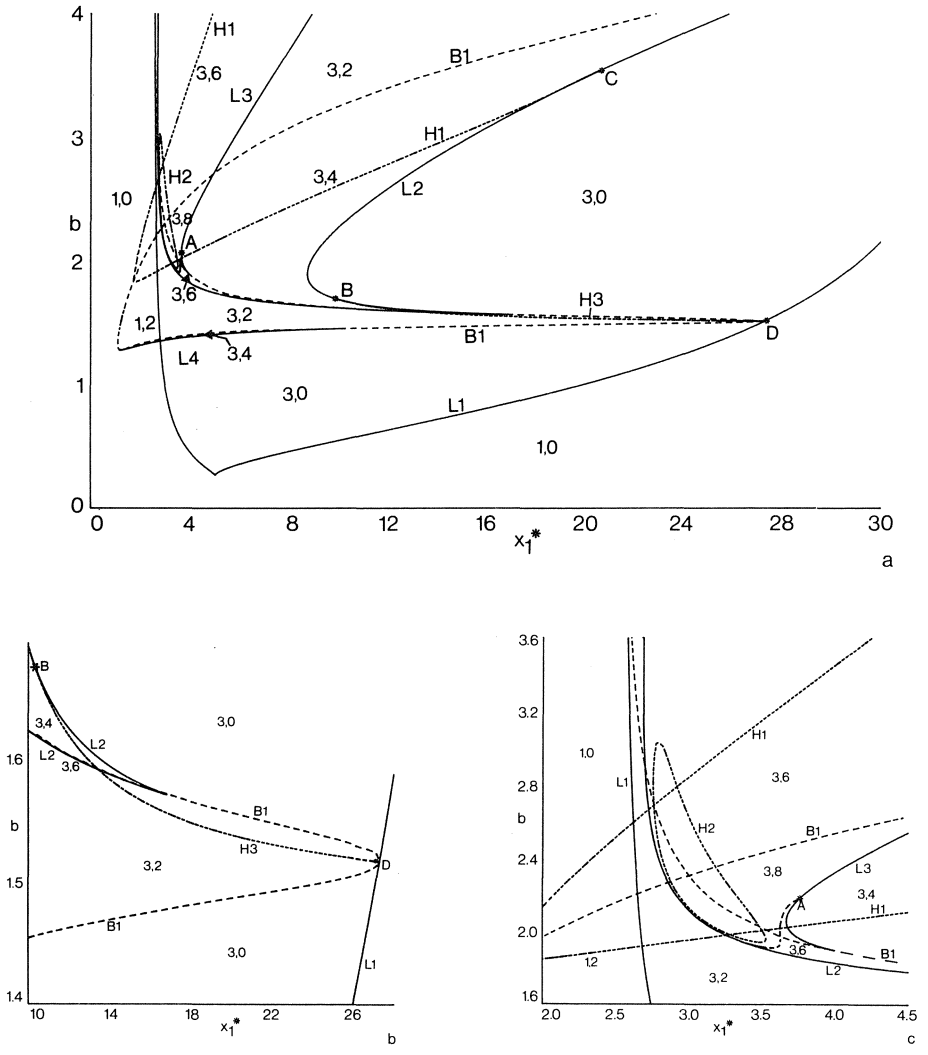

FIGURE 3.1. a. Curves of singular points in the b, x_1^* parameter space. Solid lines are curves of turning points ($L1$, $L2$, $L3$), dashed lines are curves of pitchfork bifurcations ($B1$) and dotted lines are curves of Hopf bifurcation points ($H1$, $H2$, $H3$). The symbols a_s, a_m denote the number of single-mode equilibria and mixed-mode equilibria, respectively. The points A, B, C and D are associated with a direct transition from regular to chaotic behaviour.

b. Blow-up of a.: $10 < x_1^* < 28$, $1.4 < b < 1.7$.

c. Blow-up of a.: $2 < x_1^* < 4.5$, $1.6 < b < 3.5$.

Stability properties of at least one of the equilibria change each time that a curve in the diagram is crossed. They are not indicated since the diagram is already densely filled with information. In figure 3.1 b,c blow-ups of two regions are presented where the behaviour is rather complicated. Thick points in the diagram are special singular points of the model, because they are associated with bifurcations of codimension larger than one. It means that more than one free parameter is needed to describe the bifurcation adequately. For example, the unfolding near the point $(x_1^*, b)=(5.042, 0.267)$ is the well-known cusp catastrophe described in appendix D. The phase flow structure near such points can be rather complicated. Of particular interest are the points labelled A,B,C and D. There we have the coaslescence of a Hopf bifurcation and a saddle-node bifurcation. As will be dicussed later on, at these points a direct transition occurs from regular to chaotic solutions.

The curve $L1$ is the bifurcation set of the three-component subsystem, where the number of single-mode equilibria changes from one to three. From figure 3.1 we conclude that for $b<1.279$ the six-component model has a similar qualitative behaviour with only single-mode equilibria. However, if b becomes larger additional mixed-mode equilibria occur, making the bifurcation diagram more complicated. In figure 3.2 cross-sections of some bifurcation diagrams are presented. Shown are the $\hat{x}_1$- and $\hat{x}_4$-components of the equilibria as a function of x_1^* for $b=1.4$, $b=1.5$, $b=1.6$ and $b=2$. Note that the high-index equilibria (E_1) are always stable. When $b>1.279$ mixed-mode equilibria are generated at the branch of low-index (E_3) equilibria. This occurs by means of pitchfork bifurcations which cause E_3 to become unstable. The bifurcations are due to topographic instability of the (1,2) Rossby mode: at this point the wave is in phase with the topography. Beyond the bifurcation perturbations on the unstable state E_3 have a growing standing-wave structure.

As long as $b<1.517$ mixed-mode equilibria are absorbed by the E_3-branch (figure 3.2 a,b). However, if b exceeds this bound they vanish at the branch of E_2-equilibria (figure 3.2 c,d). Another, more important, aspect for $b>1.517$ is that equilibria can become unstable due to the presence of Hopf bifurcations, causing the generation of periodic solutions. Hopf bifurcations are a manifestation of the barotropic instability mechanism and the periodic solutions can be interpreted as topographically modified propagating barotropic Rossby waves.

Explicit calculations of stationary points have been carried out for the parameter values $b=1.6$ and $x_1^*=4$, a case that was also considered in section II.4. The results for the single-mode equilibria are already presented in (2.59), except that they now have the additional components $\hat{x}_4=\hat{x}_5=\hat{x}_6=0$. Furthermore, two mixed-mode equilibria occur:

$$E_{4a}/E_{4b}=(0.599,-0.394,-0.354,\pm 0.195,\mp 0.090,\mp 0.357). \quad (3.4)$$

The streamfunction patterns of E_1, E_2 and E_3 are shown in figure 2.4, those of E_{4a} and E_{4b} are presented in figure 3.3. As can be seen there is qualitatively little difference between E_3, E_{4a} and E_{4b}: they are all of low-index type. The situation in the six-dimensional phase space is sketched in figure 3.4 as a

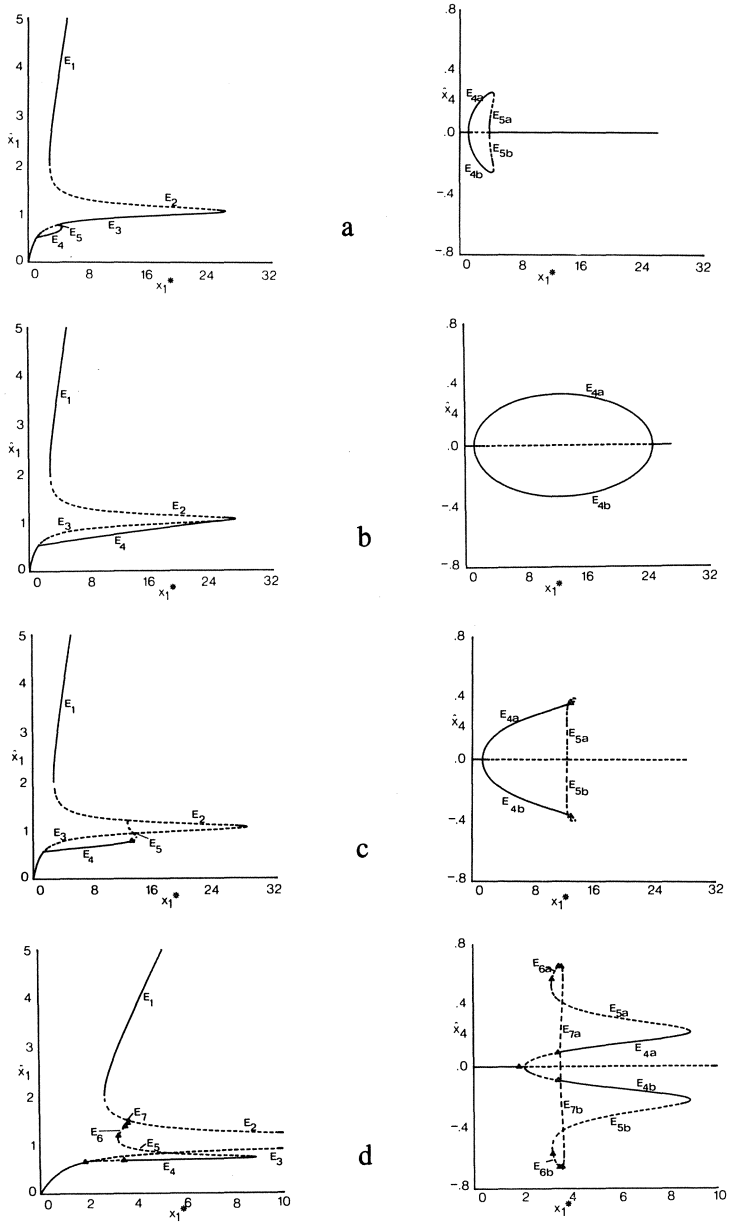

FIGURE 3.2. From left to right: $\hat{x}_1$- and $\hat{x}_4$-components of the equilibria as a function of x_1^* for $b=1.4$ (a), $b=1.5$ (b), $b=1.6$ (c) and $b=2.0$ (d). A solid line denotes that the solution is stable, while a dashed line indicates an unstable solution. The triangle symbol represents a Hopf bifurcation point.

projection of the phase flow onto the $x_1 - x_4$ plane. Both E_2 and E_3 are now of the saddle-point type and lie on separatrices between the attraction domains of the stable equilibria E_1, E_{4a} and E_{4b}.

In figure 3.1 there is one dashed region where no stable equilibria exists. Numerical integrations show that for these parameter values trajectories starting from arbitrary initial conditions tend to a globally attracting limit cycle. Thus we conclude that the set of limit points of the six-component model at least contains a point attractor or periodic attractor.

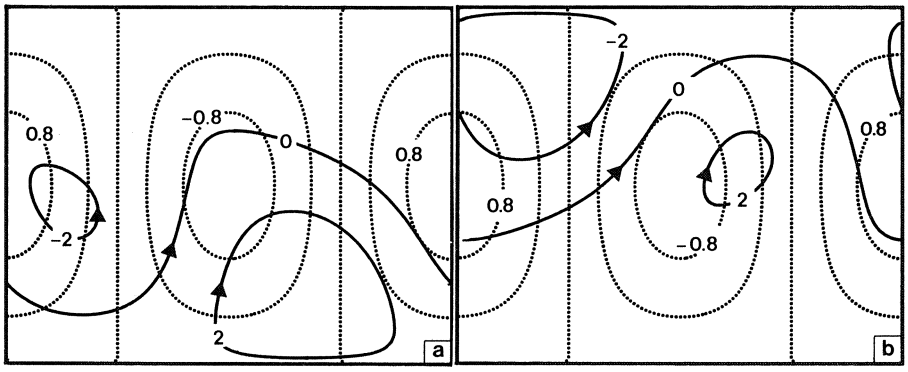

FIGURE 3.3. As figure 2.4, but for the equilibria E_{4a} (a) and E_{4b} (b) defined in (3.4).

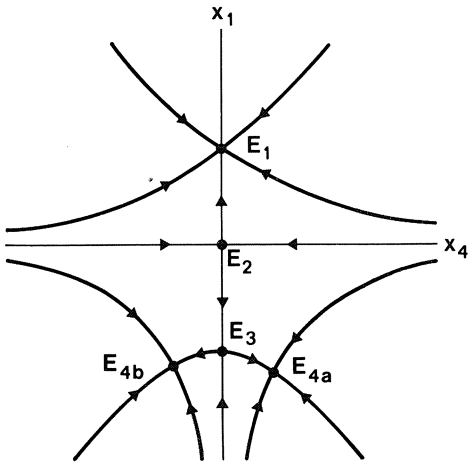

FIGURE 3.4. Sketch of the phase flow projected onto the $x_1 - x_4$ plane of the six-component mode in the case $b = 1.6$, $x_1^* = 4$. Initial conditions are chosen for fixed x_2, x_3, x_5 and x_6.

III.3 Periodic and aperiodic solutions

III.3.1. Zonal flow instabilities

In figure 3.1 indications are present that the behaviour of the six-component model can be chaotic. To investigate the existence of strange attractors we have studied the position and stability of periodic orbits branching off from stationary points as a function of x_1^* for $b=1.6$ and $b=2.0$. As discussed in the previous section in these cases periodic solutions can be generated representing barotropic propagating waves. Clearly, these values are *characteristic* for the behaviour of the model since for $b=1.6$ the (0,2) zonal flow mode can become unstable whereas for $b=2$ this may occur for the (1,1) wave mode, see (3.2). Note that once the periodic orbits branch off from stationary points of the mixed-mode type, they occur in pairs. If their orbits in phase space are given as $P_\mu(x;t)=0$ and $\tilde{P}_\mu(x;t)=0$, they are related by

$$P_\mu(x_1,x_2,x_3,x_4,x_5,x_6;\,t) = \tilde{P}_\mu(x_1,x_2,x_3,-x_4,-x_5,-x_6;\,t)\,, \tag{3.5}$$

This is a consequence of the natural symmetry of the system.

For $b=1.6$ there is one pair of Hopf bifurcation points occurring at the mixed-mode equilibrium branches for $x_1^*=12.954$, see figure 3.2c. Here the imaginary parts λ_i of the two complex conjugated eigenvalues with real part zero are $\lambda_i=\pm 0.227$. Consequently, periodic orbits with initial period $T=2\pi/|\lambda_i|=27.653$ and amplitude zero branch off. In figure 3.5 the period of these orbits is shown as a function of the external forcing.

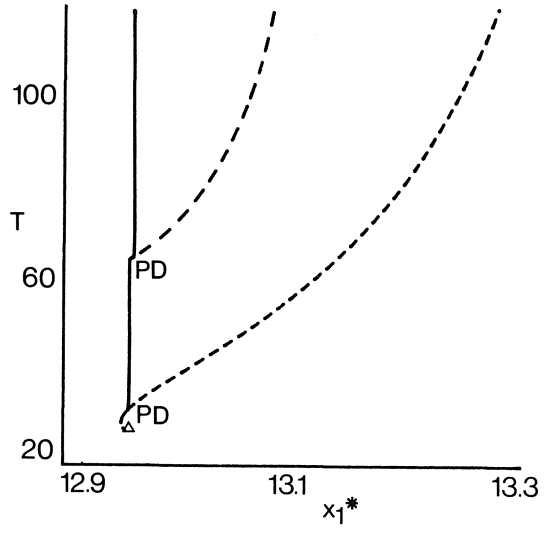

Figure 3.5 Period T of the periodic orbits as a functions of x_1^* for $b=1.6$. Stability properties are denoted by a solid curve (stable) or a dashed curve (unstable). A Hopf bifurcation is indicated by a triangle, a period-doubling bifurcation by *PD*.

Clearly, the Hopf bifurcation is subcritical, i.e. a branch of stable equilibria absorbs a branch of unstable periodic orbits, see the description in appendix D. However, already for a slightly smaller external forcing ($x_1^* = 12.951$) the periodic orbit merges into a saddle-node bifurcation together with a stable periodic orbit. Next, stable periodic solutions can be found in the range $12.951 < x_1^* < 12.9585$. An example of such a solution is shown in figure 3.6a for $x_1^* = 12.958$. They ultimately loose stability in a period-doubling bifurcation at $x_1^* = 12.9585$. In figure 3.6b a stable doubly-periodic solution is shown which exists for $x_1^* = 12.9596$. It is found that a sequence of period-doubling bifurcations takes place, leading to the generation of a strange attractor for x_1^* slightly larger than 12.96. A chaotic solution, occurring for $x_1^* = 12.961$, is shown in figure 3.6c.

We have demonstrated that this signal is chaotic by computing its Lyapunov exponents, following the method of WOLF et al. (1985). These numbers measure the average exponential growth of the principal axes of an infinitesimal small 'error' sphere along the orbit. Positive Lyapunov exponents indicate that initially nearby orbits in phase space diverge. The reciprocal of the largest positive exponent defines a time scale on which the system is predictable on the average. In this case it was found numerically that there is one positive Lyapunov exponent $\nu_1 = 0.016$. We have not analysed the strange attractors in detail, since they do not have a global structure. In this case they remain permanently in the low-index regime.

The region of x_1^*-values for which strange attractors occur appears to be very narrow. Numerical integrations show that for $x_1^* \geqslant 12.962$ trajectories starting from arbitrary initial conditions converge to the stable stationary point E_1. Obviously the strange attractors have changed into nonattracting strange invariant sets, the chaotic solutions have become unstable and therefore they can no longer be obtained from numerical integrations. In order to interprete figure 3.5 we use some arguments discussed in THOMPSON and STEWART (1986). We hypothesise that the qualitative changes at $x_1^* = 12.962$ are associated with global bifurcations involving heteroclinic connections between the unstable periodic orbits and the saddle-points E_{5a}/E_{5b} defined in figure 3.2c. Next the strange invariant sets disappear in a global bifurcation at $x_1^* \cong 13.26$. For that parameter value the unstable principal periodic orbits have become homoclinic orbits which connect the saddle-points E_{5a} and E_{5b} with themselves. This bifurcation is called a blue-sky catastrophe because for larger x_1^* values the orbits do no longer exist: "they have vanished into the blue sky". A numerical approximation of one of the homoclinic orbits, considered as a periodic orbit with period $T \to \infty$, is shown in figure 3.6d. The route, which leads to the disappearance of a strange attractor for an increasing forcing parameter, is described in SPARROW (1982) as a type-*B* homoclinic explosion. The reverse route (a type-*A* homoclinic explosion) *generates* a strange attractor for an increasing forcing parameter. This type of behaviour is for instance found in the LORENZ (1963) convection model.

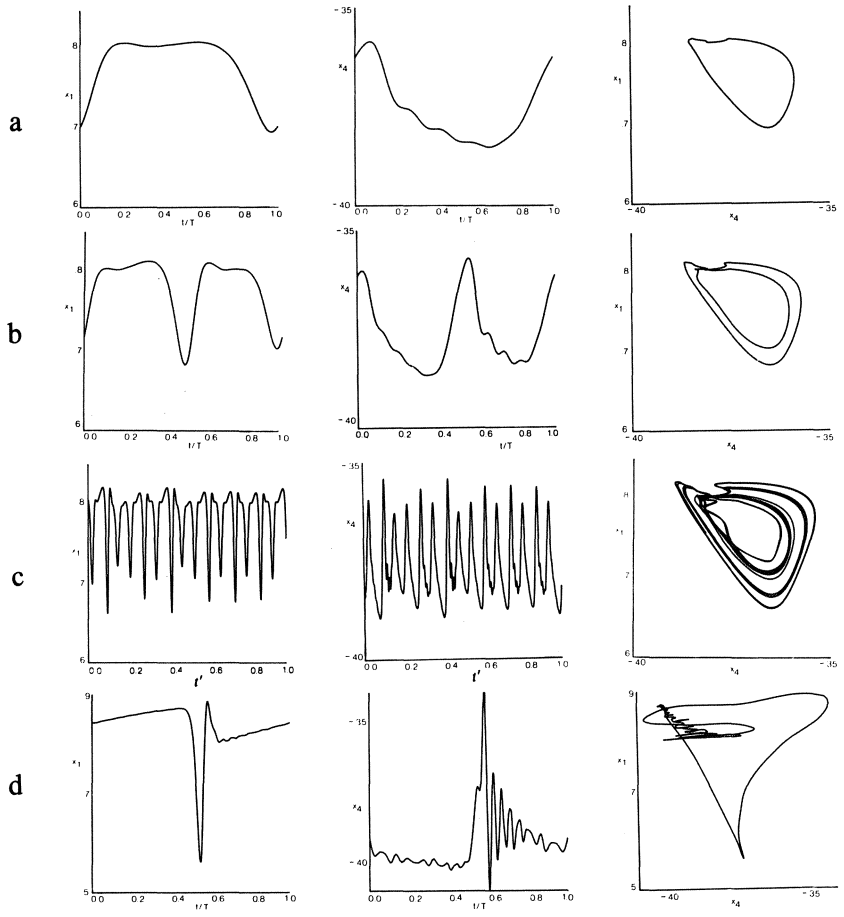

FIGURE 3.6. a. From left to right: x_1-component of stable periodic solution, existing for $b=1.6$ and $x_1^*=12.958$, as a function of t/T (where T is the period), x_4-component as a function of t/T and projection of the orbit onto the x_1-x_4 plane.

b. As a., but for $x_1^*=12.9596$.

c. Chaotic time series for $b=1.6$, $x_1^*=12.961$, generated by starting on the unstable principal periodic orbit. From left to right: x_1-component as a function of $t'=(t-1000)/500$, x_4-component as a function of t' and projection of the trajectory onto the x_1-x_4 plane.

d. Numerical approximation of one of the two homoclinic orbits occurring at $b=1.6$, $x_1^*=13.26$ as a periodic solution with period $T\to\infty$. From left to right: x_1-component as a function of t/T, x_4 component as a function of t/T and projection of the orbit onto the x_1-x_4 plane. The other homoclinic orbit is obtained by reversing the signs of x_4, x_5 and x_6.

III.3.2 Rossby wave instabilities

We will now consider the continuation of periodic orbits generated by Hopf bifurcations occurring for $b=2$. Then the parameter values are similar to those used by CHARNEY and DEVORE (1979). From figure 3.2d it appears that there is one Hopf bifurcation at a branch of single-mode equilibria ($x_1^*=1.864$). Furthermore, four pairs of Hopf bifurcation points are found at mixed-mode equilibrium branches for $x_1^*=3.456$, $x_1^*=3.229$, $x_1^*=3.503$ and $x_1^*=3.623$. The study of periodic solutions involved in these bifurcations will be referred to as case I, II, III, IV and V, respectively.

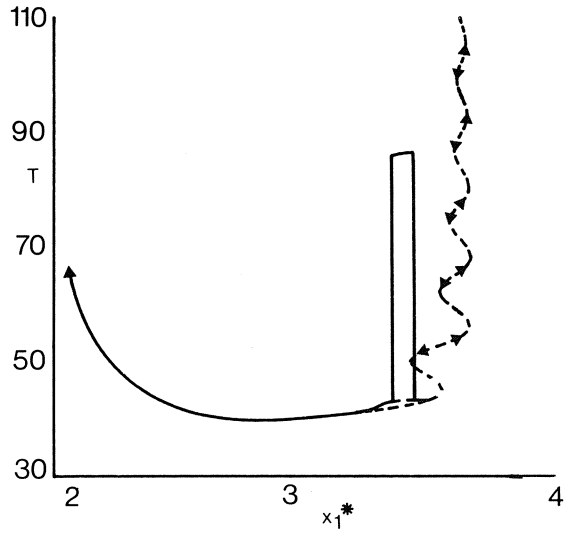

FIGURE 3.7. Period of the periodic orbits as a function of x_1^* for $b=2$, case I. For explanation see the text. Stability properties are indicated by a solid curve (stable) and dashed curve (unstable). The symbols $<$ and $>$ indicate a supercritical and subcritical sequence of period-doubling bifurcations in a very small range of x_1^*-values.

In figure 3.7 the period of the orbits is shown as a function of x_1^* for case I. Part of this bifurcation diagram ($0<x_1^*<3.5$) has been described by YODEN and HIROTA (1984) and YODEN (1985). Some time series of the x_1- and x_4-components, as well as projections of the periodic orbits onto the x_1-x_4 plane, are shown in figure 3.8 for various forcing values. It appears that the stable periodic solutions bifurcate on the side of the unstable equilibrium E_3, hence it is a supercritical Hopf bifurcation (see appendix D). With increasing x_1^* the amplitude of the periodic orbits increases while the period decreases a little. The behaviour of the solution becomes more complicated because of the higher harmonics of the fundamental frequency (figure 3.8a,b).

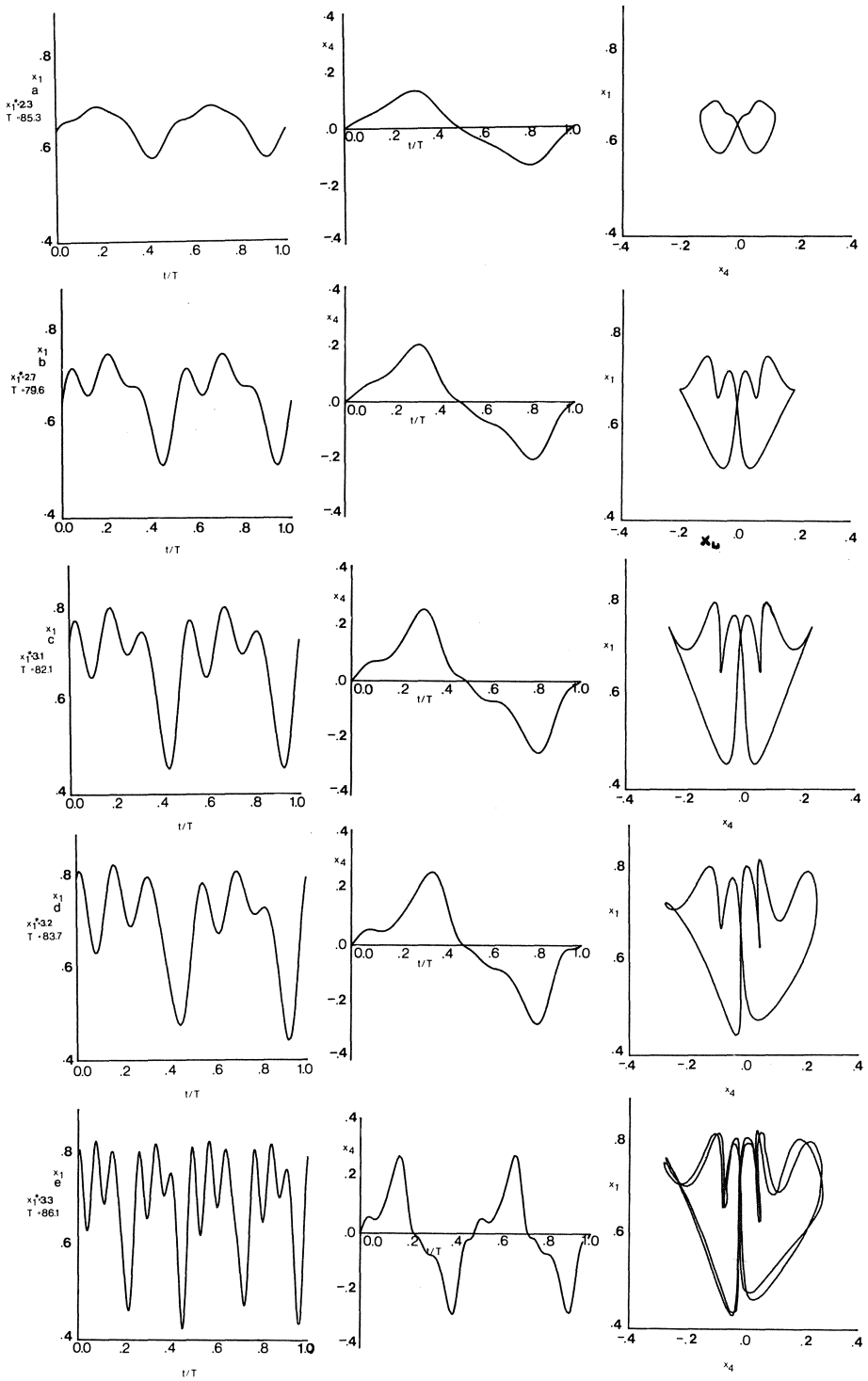
a
x1*2.3
T =85.3
b
x1*2.7
T =79.6
c
x1*3.1
T =82.1
d
x1*3.2
T =83.7
e
x1*3.3
T =86.1
x1
x4
t/T

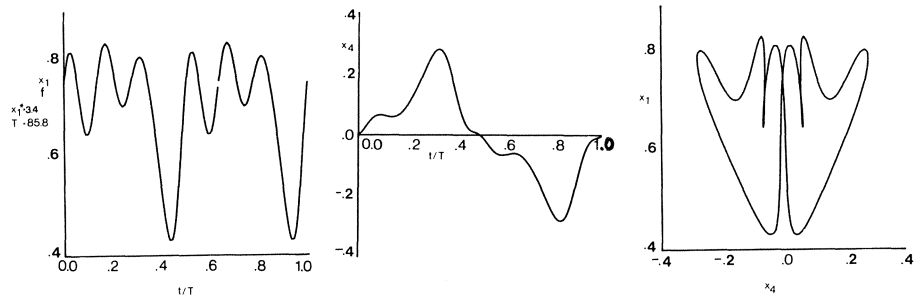

FIGURE 3.8. Visualization of some periodic orbits occurring for $b=2$, case I. Shown are $x_1(t/T), x_4(t/T)$ and a projection of the orbits onto the x_1-x_4 plane. Here t is time and T the period.

Note that the orbits are symmetric with respect to $x_4=0$, $x_5=0$, $x_6=0$. At $x_1^*=3.122$ the symmetry is broken by a pitchfork bifurcation. The symmetric periodic orbit becomes unstable while two non-symmetric stable periodic orbits branch off. One of them is shown in figure 3.8c, the other one is obtained by reflection in $x_4=0$. Each of the non-symmetric orbits becomes unstable at $x_1=3.276$ due to a period-doubling bifurcation. An example of a doubly-periodic solution is shown in figure 3.8d. Further period-doubling bifurcation do not take place. On the contrary, we have a period-halving bifurcation at $x_1^*=3.368$ and a pitchfork bifurcation at $x_1^*=3.432$.

For $x_1^*=3.5$ YODEN (1985) found chaotic solutions, but no explanation is given of the bifurcation route resulting in the occurrence of a strange attractor. However, using figure 3.7 we are able to describe the scenario leading to chaos. If we continue the branch of periodic solutions starting from the pitchfork bifurcation at $x_1^*=3.432$ for increasing x_1^* we arrive, for a slightly increased forcing ($x_1^*=3.497$), at a saddle-node bifurcation. Here the branch of stable periodic orbits coalesce with a second branch consisting of unstable periodic orbits which have larger periods. Following the latter branch for decreasing forcing values we encounter a next saddle-node bifurcation at $x_1^*=3.357$, where a coalescence occurs with a branch of stable periodic orbits. If we continue these stable solutions it appears that they are almost immediately turned unstable by a period-doubling bifurcation. The branch remains unstable until x_1^* is close to a new saddle-node bifurcation existing at $x_1^*=3.615$: for a slightly smaller forcing the branch has become stable due to a period-halving bifurcation. From that moment on the branches of periodic orbits show a similar behaviour as just described, except that the differences between successive saddle-node bifurcation values decrease and that the values of the periods increase. The tendency of the period to become infinitely large is associated with the approach to a homoclinic orbit existing for $x_1^*=3.581$. A numerical approximation of this orbit is shown in figure 3.9a. It connects the stationary point $E_3=(0.768, -0.614, -0.234, 0., 0., 0.)$ with itself. This type of bifurcation has been analysed by SILNIKOV (1965) and more recently by GLENDINNING and SPARROW (1984) and GASPARD et al. (1984). From their results it

follows that in the neighbourhood of the parameter value for which homoclinicity occurs a countable infinity of unstable periodic orbits and an uncountable infinity of aperiodic, chaotic orbits exist. The aperiodic orbits are generated and disappear due to an infinite cascade of period-doubling and period-halving bifurcations, respectively, which take place near each winding of the $T(x_1^*)$ curve in figure 3.7. Consequently, for parameter values close to the critical value at which homoclinicity occurs chaotic solutions will be found. An example of a chaotic time series, for $x_1^* = 3.5$, is shown in figure 3.9b. It has one positive Lyapunov exponent $\nu_1 = 0.040$. Note that the trajectories move in a small tube which closely follows the homoclinic orbit. The importance of this type of bifurcation for spectral models of the atmospheric circulation has been proposed by DE SWART and GRASMAN (1984). The existence of homoclinic orbits and related chaos is already suggested in figure 3.1. In this diagram codimension-2 bifurcation points occur (A,B,C,D) where a limit point and a Hopf bifurcation point coaslescence. According to LANGFORD (1981) such bifurcations involve homoclinic orbits with an associated transition to chaos, see also GUCKENHEIMER and HOLMES (1983) and a remark in LEGRAS and GHIL (1985).

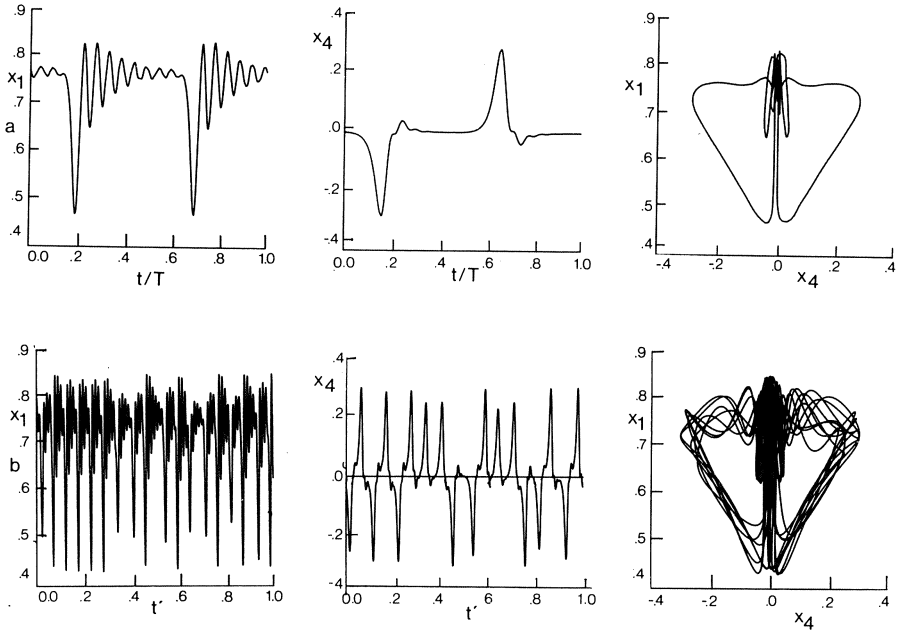

FIGURE 3.9. a. As figure 3.6d, but approximation of the homoclinic orbit at $b = 2$, $x_1^* = 3.581$.
b. As figure 3.6c, but for $b = 2$ and $x_1^* = 3.5$.

Before discussing the approach to the homoclinic orbit in more detail, we consider the continuation of periodic orbits emanating from the pair of Hopf

bifurcation points at $x_1^* = 3.456$ (case II). In figure 3.10 the period of the orbits is shown as a function of the external forcing. Starting from the subcritical Hopf bifurcation points, with initial period $T = 19.368$, a series of wiggles are found in the interval $3.45 \leqslant x_1^* \leqslant 3.65$. For $x_1^* = 3.584$ we have the approach to two homoclinic orbits. A numerical approximation of one of them is presented in figure 3.11, the other one is obtained by reversing the signs of x_4, x_5 and x_6, because of (3.1). Again they connect the saddle point E_3 with itself. In the bifurcation diagram their positions are close to the homoclinic orbit discussed previously. Each of the two new-found orbits seems to be just half a part of the orbit of figure 3.9a.

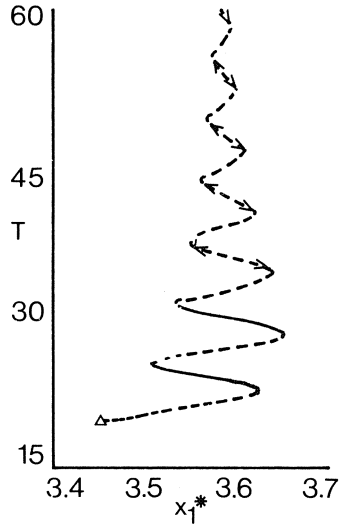

FIGURE 3.10. As figure 3.7, but for case II.

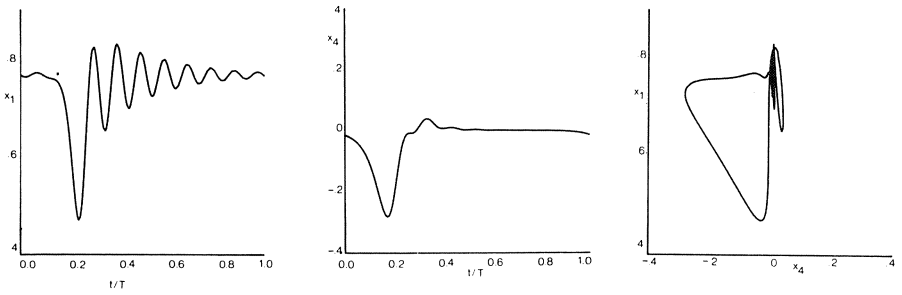

FIGURE 3.11. As figure 3.6d, but approximation of one of the homoclinic orbits at $b = 2$, $x_1^* = 3.584$.

III.3.3 Homoclinic orbits and chaos

The behaviour of the periodic solutions discussed in the previous subsection can be understood as follows, see GLENDINNING and SPARROW (1984) and GASPARD et al. (1984). Suppose that for a parameter value μ_{01} we have a homoclinic orbit connecting a saddle-point with itself, as sketched in figure 3.12a. The behaviour of the vectorfield close to μ_{01} is characterized by three eigenvalues of the matrix derivative of the vectorfield linearized at the saddle-point. They are a real positive eigenvalue λ_1 and two complex conjugated eigenvalues $-\lambda_2 \pm i\omega$ with $\lambda_2 > 0$. If $\lambda_2/\lambda_1 < 1$ the bifurcation diagram of the periodic orbits existing nearby the homoclinic orbit has a similar structure as shown in the figures 3.7 and 3.10. However, for nearby parameter values there exist a number of other, so-called subsidiairy homoclinic orbits. They make one or more encounters with the saddle point before returning to it. An example of a double-pulse subsidiairy homoclinic orbit is presented in figure 3.12b. Assume that the saddle-node bifurcations, associated with the approach to an M-pulse homoclinic orbit occurring for the parameter value μ_{oM}, exist for parameter values $\{\mu_i\}_{i=1}^{\infty}$ with $\{T_i\}_{i=1}^{\infty}$ the corresponding periods of the orbits. Then

$$\lim_{i\to\infty}(T_{i+1} - T_i) = \frac{M\pi}{\omega}, \tag{3.6a}$$

$$\lim_{i\to\infty}\left[\frac{\mu_{i+1} - \mu_{oM}}{\mu_i - \mu_{oM}}\right] = -\exp\left[\frac{-\pi\lambda_2}{\omega}\right], \tag{3.6b}$$

for a derivation see GLENDINNING and SPARROW (1984). In our model the numerical values of the three eigenvalues important in this case are

$$\lambda_1 = 0.325\ ,\ \lambda_2 = 0.067\ ,\ \omega = 1.034. \tag{3.7}$$

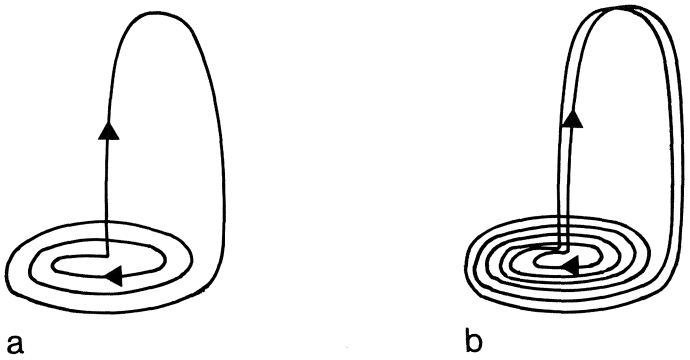

FIGURE 3.12. Sketches of a principal homoclinic orbit (a) and a double-pulse subsidiairy homoclinic orbit (b) in a three-dimensional phase space.

We have $\lambda_2/\lambda_1 = 0.206$, which is smaller than 1, as required. Substituting (3.7) in the right-hand sides of (3.6a,b) we obtain the numerical values 3.039 M and

-0.816, respectively. From the figures 3.7 and 3.10 we computed numerical values for the left-hand sides of Eqs. (3.6a,b). The results are presented in table 3.1.

	figure 3.7	figure 3.10
$T_{i+1}-T_i$	6.2	3.1
$\frac{\mu_{i+1}-\mu_{oM}}{\mu_i-\mu_{oM}}$	-0.89	-0.81

TABLE 3.1: Approximations of the left-hand sides of (3.6a) and (3.6b) from the bifurcation diagrams of figures 3.7 and 3.10.

From that we conclude that the two homoclinic orbits occurring at $x_1^*=3.584$ are principal orbits, while the homoclinic orbit at $x_1^*=3.581$ is a double-pulse subsidiairy orbit. We remark that $(\mu_{i+1}-\mu_{oM})/(\mu_i-\mu_{oM})$ is difficult to compute accurately because results strongly depend on the parameter value μ_{oM} for which the homoclinic orbits are found.

III.3.4 Bifurcation structure of remaining periodic orbits

The next case we study is the continuation of periodic orbits starting from the supercritical Hopf bifurcations at $x_1^*=3.229$ (case III). In figure 3.13 the period of these orbits is shown as a function of x_1^*. The initially stable branches of periodic orbits become unstable at $x_1^*=3.308$ due to a period-doubling bifurcation. Numerically it is found that this bifurcation is the beginning of an infinite cascade of period-doublings in the region $3.308 \leqslant x_1^* \leqslant 3.3254$, resulting in the generation of a strange attractor. An example of a chaotic time series occurring for $x_1^*=3.3255$ is shown in figure 3.14. It has one positive Lyapunov exponent $\nu_1=0.012$. The strange attractors are found in only a narrow range of forcing values. Integrations for x_1^* slightly larger than 3.326 show that trajectories starting close to the unstable principal periodic orbits tend to stable limit cycles with periods close to 86. These limit cycles have already been obtained previously, see figure 3.7. Obviously, at $x_1^*=3.326$ the strange attractors turn into nonattracting strange invariant sets. Chaotic solutions still exist, but they are unstable and hence are not obtained by means of numerical integrations. In the literature scenarios are known which describe the destabilization of a strange invariant set. They involve heteroclinic connections between unstable stationary points and unstable periodic orbits, see SPARROW (1982) and THOMPSON and STEWART (1986). However, they are not studied in detail here.

The nonattracting strange invariant sets exist for $3.326 \leqslant x_1^* \leqslant 4.315$, until they disappear in a cascade of period-halving bifurcations, the last one occurring at $x_1^*=4.223$. After that only the principal periodic orbits are left having two Floquet multipliers with absolute values larger than 1, see figure 3.13b. These numbers indicate the degree of instability of a periodic solution, as discussed in appendix D. Next the branches merge into saddle-node bifurcations together with branches of periodic orbits which originates from the pair of

Hopf bifurcation points at $x_1^* = 3.503$. Obviously, the cases III and IV are connected and have been studied together.

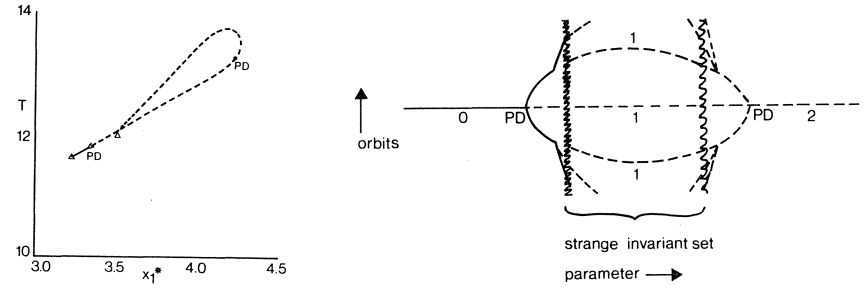

FIGURE 3.13. a. As figure 3.7, but for the cases III and IV.
b. Bifurcation scheme in the region between the period-doubling bifurcations of figure 3.13a. The straight line denotes the principal periodic orbit. The number of Floquet multipliers with absolute values larger than 1 (which measures the degree of instability of the periodic orbits) is also indicated.

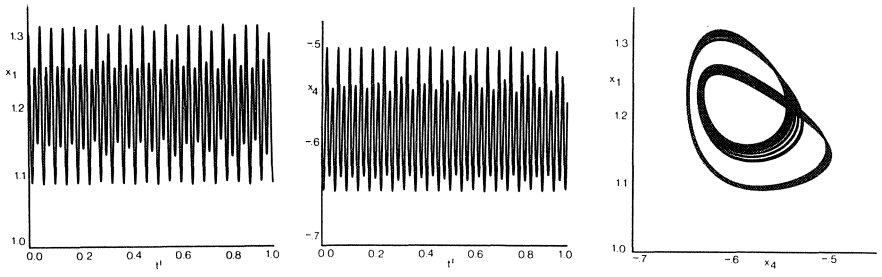

FIGURE 3.14. As figure 3.6c, but for $b = 2$ and $x_1^* = 3.33255$.

We finally investigate the periodic orbits, generated by the subcritical Hopf bifurcations at $x_1^* = 3.623$ (case V). In figure 3.15 the period of the orbits is presented as a function of the external forcing. Again a series of wiggles is found, but only in a small region of x_1^* values. This behaviour suggests the approach to homoclinic orbits for $x_1^* = 3.625$. A numerical approximation of one of them is shown in figure 3.16. It seems that these orbits connect the equilibria $E_{6a}/E_{6b} = (1.445, 0.466, -0.182, \pm 0.657, \pm 0.147, \pm 0.024)$, defined in figure 3.2d, with themselves.

At first sight the bifurcation structure in figure 3.15 is similar to those of

figures 3.7 and 3.10. It suggests that the theory discussed in section III.3.3 can be applied. However, the normal form of this scenario requires a homoclinic orbit connecting a saddle point in three dimensions. Furthermore, the matrix derivative of the vectorfield, linearized at the saddle point, should have one positive real eigenvalue and two complex conjugated eigenvalues with negative real parts. But in this case the saddle points have two real positive eigenvalues as well as two pairs of complex conjugated eigenvalues with negative real parts. Obviously, in order to describe the approach to a homoclinic orbit in figure 3.15 in a persistent way, the Silnikov theory should probably be generalized to systems of dimensions larger than 3. Another problem comes from the numerically observed fact that in most cases trajectories starting close to the unstable principal periodic orbits are not chaotic. Instead they tend to one of the stable equilibria E_{4a} or E_{4b}. Thus the scenario leading to the bifurcation structure shown in figure 3.15 remains to be investigated.

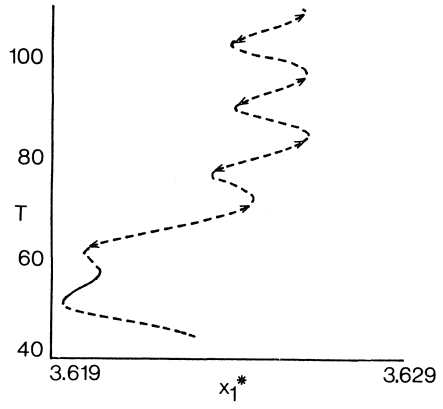

FIGURE 3.15. As figure 3.7, but for case V.

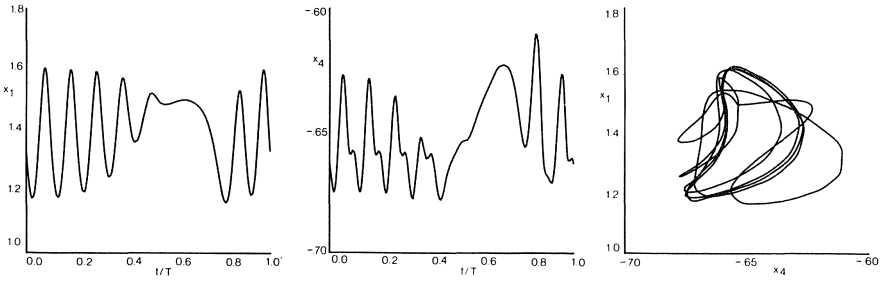

FIGURE 3.16. As figure 3.6d but for $b=2$ and $x_1^*=3.625$.

III.4. THE POSSIBILITY OF INDEX CYCLES

In order for the six-component system to model the large-scale atmospheric circulation it should have at least qualitative agreement with synoptic observations. Therefore, we expect the system to fluctuate irregularly between different preferent domains in phase space. So far we have found irregular chaotic solutions for certain parameter values and initial conditions, but they remain in the low-index flow regime forever. Moreover, the corresponding strange attractors in phase space have small attraction domains: there is only a small set of initial conditions for which trajectories are attracted to a strange invariant set. For the concept of deterministic chaos to be physically meaningful the strange attractor should have a global structure in phase space. In other words, chaotic trajectories should be capable of visiting both the low-index and high-regimes. Such a system would show the characteristics of an index cycle. A recent discussion about this phenomenon is given in WALLACE and BLACKMAN (1983). In our model an index cycle is not found because the high-index equilibrium E_1 is stable for all parameter values. This is due to the fact that the equilibrium is dominated by a (0,1) zonal flow component. It cannot be destabilized by topographic instability since this mechanism only acts on wave modes. Furthermore, barotropic instability of the (0,1) mode is not possible due to the Fjørtoft theorem (FJØRTOFT, 1953) because it has the smallest wave number of the spectrum.

However, with a slight extension of the model we can allow for unstable high-index equilibria. This is done by introducing a nonzero amplitude x_4^* of the external forcing in the (0,2) zonal flow mode. For sufficiently large $|x_4^*|$ values and $b<\sqrt{3}$ the (0,2) mode can become barotropically unstable, see (3.2) and appendix E. As an example we take the numerical values $b=1.6$, $C=0.1$, $\beta=1.25$, $\gamma=1$, $x_1^*=4$ and let x_4^* be a free parameter. In appendix E a lower bound is computed of the critical amplitude $|x_{4,c}^*|$ for which barotropic instability of the high-index equilibrium occurs. It is found that $|x_{4,c}^*|$ should be somewhat larger that 0.35. In figure 3.17 results of a numerical bifurcation analysis are presented. They show the $\hat{x}_4$-component of the equilibria as a function of x_4^*, where for $x_4^*=0$ is started in the equilibria E_1,E_2 and E_3 (defined in (2.59)), respectively. Considering E_1, it becomes barotropically unstable at $|x_{4,c}^*|=0.402$ by means of a Hopf bifurcation. We have investigated the continuation of periodic orbits emanating from these bifurcation points. With increasing $|x_4^*|$ stable periodic orbits are found which turn unstable at $|x_4^*|=8.459$ due to a period-doubling bifurcation. However, at $|x_4^*|=11.771$ they become stable again by absorbing a branch of unstable doubly-periodic orbits. The principal periodic orbits ultimately loose stability at $|x_4^*|=19.705$ by means of a torus bifurcation.

We have investigated the existence of strange attractors in the range $0<|x_4^*|<15$. It was found that trajectories either tend to a limit cycle of the high-index type or to a stationary point of the low-index type, but no chaotic solutions were obtained. The existence of point attractors can be understood from figure 3.17b,c. It appears that the equilibrium E_2 remains unstable if x_4^* is varied, but in all cases a stable equilibrium of the low-index type is found.

When $|x_4^*|$ is large most energy of these equilibria is contained in the (1,1) wave mode. This mode cannot become unstable because the model contains only one wave triad, for which (3.2) holds, and here $b<\sqrt{3}$. Thus, the conclusion is that the six-component barotropic spectral model cannot generate index cycles.

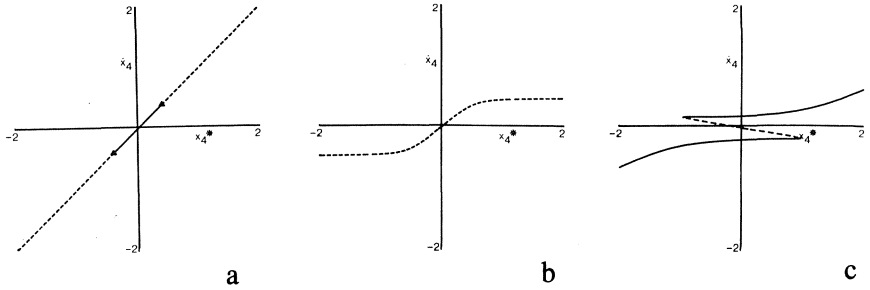

FIGURE 3.17. $\hat{x}_4$-component of the equilibria for $b=1.6$ and $x_1^*=4$ as a function of x_4^*. For $x_4^*=0$ a restart is made in $E_1(a),E_2(b)$ and $E_3(c)$. Stability properties are indicated by a solid line (stable) or dashed line (unstable). The triangle symbol denotes a Hopf bifurcation point.

III.5 CONCLUDING REMARKS

We have studied a six-component spectral model of the barotropic potential vorticity equation in a beta-plane channel, originally derived by CHARNEY and DEVORE (1979). In order to investigate in what sense the model reflects features of the atmospheric circulation a systematic bifurcation analysis has been carried out for two free parameters. They are the external forcing and the width-length ratio of the channel, which control the topographic and barotropic instability mechanisms, respectively. It is concluded that the physical and mathematical properties of the model are richer than those of the three-component subsystem. In both models multiple equilibria can occur for fixed parameter values. The associated streamfunction patterns resemble large-scale preference states of the atmospheric circulation. However, the asymptotic states of the subsystem are always stationary, while for the full model also periodic, quasi-periodic and chaotic solutions are found. In particular the occurrence of strange attractors is of interest since the associated solutions model an irregular time-dependent flow. Furthermore, chaos is characterized by sensitive dependence on the initial conditions: nearby orbits in phase space exponentially diverge during the evolution of the system. Since in practical situations initial conditions are never known with infinite precision, the system evolution can only be predicted for a finite amount of time. A finite predictability is typically one of the properties of the atmospheric circulation. This

follows from numerical experiments as well as from theoretical studies (HOLLOWAY and WEST, 1984).

Various scenarios are found which describe the generation or disappearance of a strange attractor. Apart from the period-doubling route we obtained homoclinic orbits connecting stationary points with themselves. For nearby parameter values chaotic trajectories occur moving in small tubes around the homoclinic orbits. This is in agreement with the theory of SILINIKOV (1965), see also GLENNDINNING and SPARROW (1984) and GASPARD et al. (1984).

Despite its complexity and interesting properties the validity of the model is limited. It appears that the strange attractors do not have a global structure in the sense that chaotic trajectories are capable of visiting alternately different preferent regions in phase space. Thus it is concluded that the six-component model cannot show vacillatory behaviour. The reason is clearly due to a lack of barotropic wave triads or, equivalently, due to the severe truncation. Internal vacillation can only be obtained by allowing quasi-statically changes of the parameters. This can be considered as modelling slowly varying boundary conditions in the atmosphere, as described in LEGRAS and GHIL (1985).

For fixed parameter values vacillation can be generated in three ways. The first is to add stochastic perturbations to the spectral equations, which will be done in the next chapter. The second way consists of constructing a spectral model with more degrees of freedom by allowing more eigenfunctions in the spectral expansions. We shall discuss this method in chapter V. The third possibility is to study spectral models of baroclinic flows to which we shall return in chapter VI.

IV. Effect of stochastic perturbations on low-order atmospheric spectral models *

IV.1. Introduction

It was discussed in chapter I that, in order to obtain a better understanding of the atmospheric circulation, detailed information is required about the ultra-long quasi-stationary waves and transient synoptic-scale eddies. This problem is often studied with a planetary-scale model, in which the effect of the transient eddies is parametrized. There are several propositions to solve this closure problem. One possibility is to use techniques, originating from turbulence theory, to express the eddy characteristics in terms of the resolved part of the flow. For grid-point models this has been done by White and Green (1982) and Shutts (1983). An alternative method is to represent the eddy forcing by stochastic terms. Balgovind et al. (1983) applied it to a grid-point model.

In this tract we study spectral models of the large-scale atmospheric flow. Such a model can be formulated as a dynamical system of the type (1.1). In the derivation of the spectral model we have the freedom to choose the flow characteristics (e.g. barotropic or baroclinic), the geometry of the domain (e.g. a beta plane or the sphere) and the truncation number N. The forcing terms $F(t)$ in (1.1) represent the effect of the neglected short-scale modes and additional physical processes not incorporated in the model.

By application of coarse-grain methods from nonequilibrium statistical mechanics, Lindenberg and West (1984) have shown that (1.1) is formally a system of stochastic differential equations with its stochastic character fully due to the uncertainty in the initial values of the unresolved modes. Their results indicate that the forcing terms are complicated and do not fit the description given by Charney and DeVore (1979) and Egger (1981): they

* co-author J. Grasman.

are only stationary and Markovian under rather restrictive conditions. However, in practice these restrictions can be weakened. EGGER and SCHILLING (1983, 1984) and BARNETT and ROADS (1986) have determined the statistical characteristics of the forcing terms from data and found that they could be fitted with coloured-noise processes, which are stationary and Markovian. Furthermore these authors analysed the response of a linearized spectral model of the barotropic vorticity equation to this forcing. Taking into account the ultralong waves only they showed that in this way it is possible to explain a substantial part of the observed long-term variability of the atmosphere.

In section II.3 and chapter III it has been demonstrated that trajectories of a three- and six-component barotropic spectral model in phase space tend to different sets of limit points. Each of these sets, with its corresponding attraction domain in phase space, represents a specific flow regime. However, the models do not describe transitions between the different weather regimes, as observed for the atmospheric circulation (NAMIAS, 1950). In order to obtain this vacillatory behaviour stochastic perturbations will be added to the spectral equations. They are considered as a parametrization of the forcing terms $F(t)$ defined in (1.1). The noise forces the system to alternately visit the different preferent regimes. The expected residence time of the system in a regime is then a measure for the persistence of a large-scale preferent state. EGGER (1981) studied the effect of random forcing of the Gaussian white-noise type on the three-component model of section II.3. BENZI et al. (1984) and MORITZ (1984) computed expected residence times of this system in the attraction domains of the stable equilibria of the unperturbed system as a function of the zonal forcing. Here we will also compute the responses as a function of the intensity and correlation time of the noise.

Mathematical aspects of stochastic processes are considered in more detail in section IV.2. Next, in section IV.3 a method is discussed to compute expected residence times in an attraction domain of a stable equilibrium of the unperturbed system. It differs in some respect from the method considered in DE SWART and GRASMAN (1987): it can now be applied to six-dimensional spectral models. The results are presented in section IV.4. Following the ideas of Ghil (pers.comm.) to model geophysical systems by discrete models, we consider in section IV.5 a discrete-state Markov model of the atmospheric circulation. A similar study has been performed by SPEKAT et al. (1983) using atmospheric data. Our model consists of three states, viz. a high-index, a low-index and a transitional state. Transition probabilities per unit of time are specified using the results of section IV.4. We then calculate the time evolution of the probability distribution from the master equations. The eigenvalues of these equations determine the time scale over which the effect of the initial state is present in this distribution. Finally some concluding remarks are given in section IV.6.

IV.2. Dynamical systems forced by random noise

Consider the system (1.1) where the $F(t)$ are assumed to be random terms. In this section a few remarks will be given on the formulation of stochastic dynamical systems. In order to describe the transition from a deterministic to a stochastic evolution in a mathematical precise way is complicated and requires a thorough knowledge of the theory of stochastic processes. Here we only present results which are needed during the course of this chapter. More detailed discussions about stochastic processes can be found in Gardiner (1983) and van Kampen (1983).

A stochastic dynamical system can be written as

$$\begin{aligned} dx &= f_\mu(x)dt + \epsilon\underline{\sigma}(x).d\Phi(t), \\ \Phi(t) &= \int_0^t \eta(s)ds. \end{aligned} \tag{4.1}$$

Here ϵ is the noise intensity, σ an $(N\times N)$ diffusion matrix and the N components of $\eta(t)$ represent the random forcing. The latter are assumed to be stationary, which implies that their statistical moments do not depend explicity on time. Important characteristics of the noise terms are the mean values $<\eta>$ and the correlation matrix

$$\underline{C}_\eta(\tau) = <\eta(t)\eta(t+\tau)>, \tag{4.2}$$

where $<\ >$ denotes an ensemble average. The energy of the noise in the frequency domain is given by the spectral density matrix

$$\underline{S}(\omega) = \lim_{T\to\infty} \alpha(\omega,T)\alpha^*(\omega,T)\ ,\ \ \alpha(\omega,T) = \int_{-T}^{T} \eta(t)e^{i\omega t}dt, \tag{4.3}$$

with the asterix denoting a complex conjugation. According to the Wiener-Khinchine theorem, for stationary processes the spectral density matrix is the Fourier transform of the correlation matrix (Priestly, 1981), thus

$$\underline{S}_\eta(\omega) = \int_{-\infty}^{\infty} \underline{C}_\eta(\tau)e^{i\omega t}dt. \tag{4.4}$$

In this way a multivariate stochastic process $X_\epsilon(\eta,t)$ is generated, which takes on the realisations x. In general the evolution at any time will depend on the history of the process, which is a fundamental difficulty in the analysis of the dynamics. This problem can be met by choosing the $\eta(t)$ to be white-noise processes $\xi(t)$ with the properties

$$<\xi(t)> = 0;\ \ \underline{C}_\xi(\tau)=<\xi(t)\xi(t+\tau)> = \underline{I}\delta(\tau). \tag{4.5}$$

Here I is the $(N\times N)$ unity matrix and $\delta(\tau)$ the Dirac delta function with argument τ. Thus, white-noise processes have zero means and are fully uncorrelated.

With this choice $\Phi(t)$ in (4.1) becomes a multivariate Wiener process $W(t)$ and the stochastic dynamical system reads

$$dx = f_\mu(x)dt + \epsilon\underline{\sigma}(x)\cdot dW(t). \tag{4.6}$$

Now $X_\epsilon(\xi,t)$ is a Markov process, i.e. its realisation at any time in the future only depends on its present state. Such a process is fully described by the conditional probability density $p(x,t|x',t')$, which denotes the probability density for the $X_\epsilon(\xi,t)$ to have the realisation x at time t, given it had realisation x' at time $t' \leqslant t$. It can be shown that $p(x,t|x',t')$ is the solution of the Fokker-Planck equation

$$\frac{\partial}{\partial t}p(x,t|x',t') = -\nabla\cdot[f_\mu(x)p(x,t|x',t')] + \tfrac{1}{2}\epsilon^2\nabla\nabla:[\underline{\sigma}(x)\cdot\underline{\sigma}^T(x)p(x,t|x',t')], \tag{4.7}$$

where σ^T is the adjungated of σ (GARDINER, 1983). The solution of (4.7) gives a complete description of the stochastic dynamical system (4.6). Another method of obtaining information about the system is the statistical analysis of a large number of simulations of (4.6) by using a related system of stochastic difference equations, see appendix F.

Representing certain physical processes by white noise can be misleading, because white noise is uncorrelated and its energy is equally distributed of over all frequencies in the spectral time domain, as can be seen from (4.4) and (4.5). Consequently, the noise energy is infinite and hence the process has no physical relevance. Alternatively, we may assume the $\eta(t)$ in (4.1) to be coloured-noise processes $\zeta(t)$ which are described by the stochastic differential equations

$$d\zeta = -\alpha\zeta dt + \alpha' dW, \tag{4.8}$$

with α and α' nonnegative constants. In order for white noise and coloured noise to result in equal variances of the increments $dx(t)$, we must take $\alpha' = \alpha$. We then obtain

$$<\zeta(t)> = 0, \quad \underline{C}_\zeta(\tau) = <\zeta(t)\zeta(t+\tau)> = \tfrac{1}{2}\alpha e^{-\alpha|\tau|}\underline{I}. \tag{4.9}$$

It follows that α^{-1} is a measure for the correlation time and the white noise limit is obtained by taking $\alpha \to \infty$. Some spectral energy distributions of coloured noise for different values of α are shown in figure 4.1. They are obtained from (4.4) and (4.9).

Applying the coloured-noise forcing to (4.1) and transforming $\epsilon\zeta(t) = y(t)$, we obtain

$$d\begin{bmatrix} x \\ y \end{bmatrix} = \begin{bmatrix} f_\mu(x) + \underline{\sigma}(x)\cdot y \\ -\alpha y \end{bmatrix} dt + \epsilon \begin{bmatrix} \Theta & \Theta \\ \Theta & \alpha\underline{I} \end{bmatrix} \cdot dW \text{ in } \mathbb{R}^{2N}, \tag{4.10}$$

where Θ denotes an $(N \times N)$ matrix with zero elements. This system is of the same type as (4.6). Consequently, its solution is again a Markov process and a Fokker-Planck equation for the conditional probability density can be derived from (4.10) in an analogous manner as (4.7) follows from (4.6).

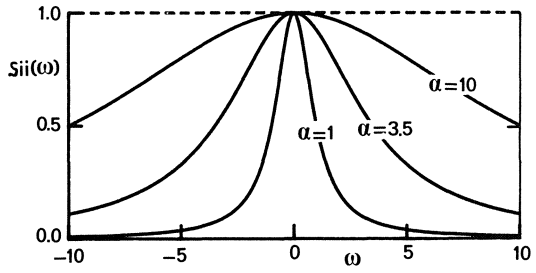

FIGURE 4.1. Distribution of energy in the spectral time domain of a coloured-noise process for different values of α. The dashed line represents the white-noise limit $\alpha \to \infty$.

IV.3. ANALYSIS OF THE STOCHASTICALLY PERTURBED SYSTEM

We consider the stochastically forced system (4.6) and assume that the unperturbed system ($\epsilon=0$) has a stable stationary point E. Define in phase space a domain $\Omega \subseteq \Omega_a$ containing E, where Ω_a is the attraction domain of E. At the boundary $\partial\Omega$ the deterministic vectorfield satisfies $f_\mu(x)\cdot\nu(x)\leqslant 0$, where $\nu(x)$ is the outward normal to the boundary. Starting in $x \in \Omega$ at time $t=0$, the perturbed system will remain in Ω for a finite time, as shown by MATKOWSKY and SCHUSS (1977). In this section we shall derive an expression for the expected residence time $T(x)$ in Ω.

We first analyse the function $\Psi(x)$ satisfying the stationary form of the Fokker-Planck equation (4.7):

$$L_\epsilon^* \Psi \equiv \tfrac{1}{2}\epsilon^2 \nabla\nabla : [\underline{a}(x)\Psi(x)] - \nabla\cdot[f_\mu(x)\Psi(x)] = 0, \tag{4.11}$$

where

$$\underline{a}(x) = \underline{\sigma}(x)\cdot\underline{\sigma}^T(x). \tag{4.12}$$

Furthermore the normalisation condition $\Psi(E)=1$ is proposed. As will become clear in the course of our derivation, the expected residence time is directly related to this function.

For low-intensity noise ($0<\epsilon<<1$) an approximate solution is assumed to be of the Gaussian form

$$\Psi(x) \sim w(x) e^{-Q(x)/\epsilon^2}, \tag{4.13}$$

with $w(E)=1$ and $Q(E)=0$. We require $\Psi(x)$ to be positive in Ω with a maximum value in $x=E$. This WKBJ-approximation originates from geometrical optics, see GOLDSTEIN (1980). It is only valid within the attraction domain of E. If Ω coincides with Ω_a, additional boundary-layer corrections for $w(x)$ are needed (MATKOWSKY et al., 1983).

Substituting (4.13) in (4.11) and collecting terms with equal power in ϵ, we obtain in lowest order the so-called eikonal equation

$$[\tfrac{1}{2}\underline{a}(x)\cdot\nabla Q(x) + f_\mu(x)]\cdot\nabla Q(x) = 0; \quad Q(E) = 0. \tag{4.14}$$

In next order an equation for w is obtained, however in our analysis it is sufficient to consider the solution of (4.14) only. In case a potential function $V_\mu(x)$ exists, such that

$$\begin{aligned} f_\mu(x) &= f_\mu^{(p)}(x)+f_\mu^{(r)}(x), \\ f_\mu^{(p)}(x) &= -\underline{a}(x)\cdot\nabla V_\mu(x), \\ \nabla V_\mu(x)\cdot f_\mu^{(r)}(x) &= 0, \end{aligned} \tag{4.15}$$

its solution is

$$Q(x) = 2\{V_\mu(x)-V_\mu(E)\}, \tag{4.16}$$

as may verified by a direct substitution of (4.15) in (4.14). At this point we note the BENZI et al. (1984) reduced their spectral model to a potential system. When the deterministic system is not of gradient type, such as the spectral models of section II.3 and chapter III, Eq. (4.14) is analysed by rewriting it as

$$H(x,p)\equiv[\tfrac{1}{2}\underline{a}(x)\cdot p+f_\mu(x)]\cdot p=0; \quad p=\nabla Q. \tag{4.17}$$

By taking the differential of the Hamilton function H along a bicharacteristic in the (x,p) space we obtain the Hamilton equations

$$\begin{aligned} \frac{dx}{ds} &= \nabla_p H = \underline{a}(x)\cdot p+f_\mu(x), \\ \frac{dp}{ds} &= -\nabla H = -\{\tfrac{1}{2}\nabla\underline{a}(x)\cdot p+\nabla f_\mu(x)\}\cdot p. \end{aligned} \tag{4.18}$$

Here s is a parameter varying along a bicharacteristic and ∇_p denotes the nabla operator with respect to the p-variables. Additionally we have

$$\frac{dQ}{ds} = p\cdot\frac{dx}{ds} = \tfrac{1}{2}\underline{a}(x):pp, \tag{4.19}$$

where (4.17) and (4.18) have been applied. Since $a(x)$ is a positive-definite matrix we see that Q increases with increasing s.

We wish to obtain values for Q at each point $x\in\Omega$, given $Q(E)=0$. This distribution is of physical interest since surfaces $Q=$constant enclose the smallest region in the x-space where the system is found with a given probability. Secondly, the Q-function is related to the expected residence time $T(x)$ of the system in Ω. As shown by GARDINER (1983) the latter satisfies Dynkin's equation

$$L_\epsilon T(x) = -1 \text{ in } \Omega; \quad T(x) = 0 \text{ at } \partial\Omega, \tag{4.20}$$

where

$$L_\epsilon\equiv\tfrac{1}{2}\epsilon^2\underline{a}(x):\nabla\nabla+f_\mu(x)\cdot\nabla \tag{4.21}$$

is the backward Kolmogorov operator, being the formal adjungated of L_ϵ^* in (4.11). An approximate solution of (4.20) is found for low-intensity noise ($0<\epsilon\ll 1$) by means of singular perturbation techniques. Using theorem

6.2.1.1 from ECKHAUS (1979) we obtain an asymptotic solution of the form

$$\begin{aligned} &T\sim C_0 e^{K/\epsilon^2} \quad \text{outside a neighbourhood of } \partial\Omega, \\ &T\sim C_0 e^{K/\epsilon^2} \quad \{1-e^{-\rho/\epsilon^2}\} \text{ near } \partial\Omega \text{ with } f_\mu(x)\cdot\nu(x)<0, \\ &T\sim C_0 e^{K/\epsilon^2} \sqrt{\frac{2}{\pi}} \int_0^{s(x)} e^{-\frac{1}{2}\hat{s}^2}\, d\hat{s} \text{ near } \partial\Omega \text{ with } f_\mu(x)\cdot\nu(x)=0, \end{aligned} \tag{4.22}$$

where

$$s(x) = \frac{2}{\epsilon}\{\int_0^\rho \tilde{\rho}\frac{\partial f}{\partial \nu}\frac{d\tilde{\rho}}{\underline{a}:\nu\nu}\}^{\frac{1}{2}}. \tag{4.23}$$

Furthermore ρ is the distance to the nearest point at the boundary and $(\partial/\partial\nu)$ is the derivative along the normal ν. Details can be found in MATKOWSKY et al. (1983). Note that $T(x)$ has a singular behaviour for $\epsilon\to 0$, because of the inhomogenous term in (4.20). This is consistent with the fact that the residence times tend to infinity if the noise intensity tends to zero. Furthermore, it appears that in this limit the expected residence time is independent of the initial value x, as long as the latter is chosen outside the boundary layer near $\partial\Omega$.

The constants C_0 and K are determined by using a method discussed in MATKOWSKY and SCHUSS (1977). By means of partial integration and application of the divergence theorem it follows that

$$\begin{aligned} \int_\Omega \{\Psi L_\epsilon T - T L_\epsilon^* \Psi\} dV = \int_{\partial\Omega} \{&\tfrac{1}{2}\epsilon^2[\Psi\frac{\partial T}{\partial n} - T\frac{\partial \Psi}{\partial n}] \\ &-\tfrac{1}{2}\epsilon^2 \Psi T(\nabla\cdot\underline{a})\cdot\nu + \Psi T f_\mu\cdot\nu\} dS. \end{aligned} \tag{4.24}$$

Here $\partial/\partial n = a(x):\nu\nabla$ is the co-normal derivative. Using (4.11), (4.13) and (4.20) we obtain

$$-\int_\Omega w e^{-Q/\epsilon^2} dV = \tfrac{1}{2}\epsilon^2 \int_{\partial\Omega} w e^{-Q/\epsilon^2} \frac{\partial T}{\partial n} dS. \tag{4.25}$$

Both integrals are of Laplace type. Substituting (4.22) in (4.25) we see that the surface integral contains $\exp[-[Q(x)-K]/\epsilon^2\}$. Its main contribution comes from the point $x_{\min}\in\partial\Omega$ where $[Q(x)-K]$ attains a minimum. Since the volume integral is of algebraic order in ϵ, the exponentially large contribution from the surface integral only cancels if

$$K = Q(x_{\min}) = \min_{\partial\Omega} Q(x). \tag{4.26}$$

Thus if we solve for $Q(x)$ from (4.18)-(4.19) we can compute the coefficient K, which is an estimate of the exponential increase of the expected residence time for a vanishing noise intensity. An integral expression for C_0 may also be found from (4.25). Its analysis requires knowledge of the function $w(x)$, which will not be considered here. In a similar way asymptotic approximations for the distribution of exit points on the boundary $\partial\Omega$ can be derived. As found

by MATKOWSKY et al. (1983) an ϵ-neighbourhood of $x_{\min}$ is the most probable exit region.

We now discuss the computation of $Q(x)$ from (4.18)-(4.19). Numerical integrations starting at $x=E$ will fail since it follows from (4.17) that $p=0$ for $x=E$, which makes it a stationary point of the Hamilton system (4.18). We may proceed in two different ways, for details see ROOZEN (1986). The first method is the initial-value approach where near $x=E$ the functions $Q(x),p(x),f_\mu(x)$ and $a(x)$ are approximated by Taylor series:

$$\begin{aligned} Q(x) &= (\underline{P}/2):(x-E)(x-E) + \mathcal{O}(|x-E|)^3, \\ p(x) &= \underline{P}\cdot(x-E) + \mathcal{O}(|x-E|^2), \\ f_\mu(x) &= \underline{F}\cdot(x-E) + \mathcal{O}(|x-E|^2), \\ \underline{a}(x) &= \underline{A} + \mathcal{O}(|x-E|). \end{aligned} \tag{4.27}$$

Here only the constant elements of matrix P are unknown. Substituting these expansions in (4.17) and collecting terms of equal power in $(x-E)$, we obtain in lowest order the matrix Ricatti equation

$$\underline{P}\cdot\underline{A}\cdot\underline{P} + \underline{P}\cdot\underline{F} + \underline{F}^T\cdot\underline{P} = 0, \tag{4.28}$$

which can be solved by standard methods (LUDWIG, (1975). Thus we have initial values (x_0,p_0,Q_0) for (4.18) and (4.19) on a small sphere around E. Integration of the Hamilton equations yields a path in x-space, called a ray. In this way the solution $Q(x)$ in Ω is constructed. Although this method yields high-accuracy solutions, a disadvantage is the lack of control over the way rays develop. This makes it less suited for the construction of confidence contours as well as for the computation of K defined in (4.26). The boundary-value approach is more useful for these cases. Then Eqs. (4.18)-(4.19) are considered with the boundary conditions

$$\begin{aligned} s\to-\infty &: Q = 0,\ x = E, \\ s = 0 &: x = e, \end{aligned} \tag{4.29}$$

where e is an endpoint which can be chosen freely. In the numerical computations the limit $s\to-\infty$ is replaced by $s=-s^*$ with s^* a sufficiently large number.

From now on we assume that Ω coincide with the attraction domain of E and $\partial\Omega$ contains a stationary point $\tilde{E}$ of the vectorfield $f_\mu(x)$. This situation is obtained with the three -and six-component models of section II.4 and chapter III for a range of parameter values. Since it follows from the eikonal equation that $\nabla Q(\tilde{E})=0$, while $f_\mu\cdot\nabla Q<0$ near $x=\tilde{E}$ at $\partial\Omega$, we have that $x_{\min}=\tilde{E}$. Obviously, unstable equilibria of $f_\mu(x)$ are the most probable exit points, hence they are of dynamical significance in the stochastically perturbed model. As $x\to\tilde{E}$ the deterministic change tends to zero. Consequently, the stochastic system slows down and remains a characteristic residence time $\tilde{T}$ near that point. Locally, the dynamics is governed by the linearized system

$$\dot{z} = \underline{D}\cdot z, \tag{4.30}$$

where matrix D has at least one eigenvalue with positive real part. Starting from an initial point $z_0=\mathcal{O}(\epsilon)$, the eigenvalue with largest positive real part λ_p determines the characteristic time:

$$\tilde{T} = \frac{d}{\lambda_p}\ln(\frac{1}{\epsilon})+\mathcal{O}(1);\ \epsilon\to 0. \tag{4.31}$$

We now discuss in more detail the computation of $K=Q(\tilde{E})$. In the initial-value approach we introduce in x-space spheres with radius R at the points E and $\tilde{E}$. Next mesh points x_0 are chosen on the sphere at E. The corresponding values of p_0 and Q_0 follow from (4.27). Then Eqs. (4.18)-(4.19) are integrated starting from the different mesh points. If a ray enters the sphere around $\tilde{E}$, the value $Q(\tilde{E})$ is obtained from a Taylor expansion at $\tilde{E}$ similar to (4.27). Next an iteration is carried out: the radius of the spheres is decreased and at each step a shooting method is applied with the result at the previous step as starting approximation for the mesh points on the sphere around E. The fundamental difficulty in this method is the strong divergence of the rays approaching $\tilde{E}$. It was found by DE SWART and GRASMAN (1987) that this method is only successful for deterministic vectorfields with dimension $N=3$. They applied it to the white noise-forced three-component spectral model.

The boundary-value approach is more powerful, as it can also handle the coloured noise-forced three-component model as well as the white noise-forced six-component model. Here we note that the computation of $K=Q(\tilde{E})$ requires the construction of a heteroclinic orbit connecting the saddle points $S=(E,0)$ and $\tilde{S}=(\tilde{E},0)$ of the Hamilton system (4.18). Consequently, in this case the correct boundary conditions are

$$\begin{aligned} s\to-\infty &: M_{us}(x,p) = 0\,, \\ s\to\infty &: M_{s\tilde{s}}(x,p) = 0\,, \end{aligned} \tag{4.32}$$

where $M_{us}(x,p)=0$ is the local unstable manifold of S and $M_{s\tilde{s}}(x,p)=0$ the local stable manifold of $\tilde{S}$. As discussed in appendix D, a stable (unstable) manifold of a stationary point is locally spanned by the eigenvectors corresponding to the eigenvalues with negative (positive) real parts. Thus the conditions (4.32) follow from a standard eigenvalue-eigenvector analysis at the saddle points S and $\tilde{S}$ of (4.18).

IV.4. RESULTS FOR LOW-ORDER SPECTRAL MODELS

The theory of sections IV.2 and IV.3 will be applied to the three- and six-component models of appendix C between the dotted and dashed lines, respectively. We assume the reader to be familiar with their properties discussed in section II.3 and chapter III. Here we take a channel of length $L=3.10^6 m$ and variable width, centered at latitude $\phi=45°$. Furthermore we take a topographic amplitude $h_0=500m$, a scale height $H=1.10^4 m$, a time scale $\sigma^{-1}=2.10^5 s$ and $f=H/h_0$. such that $\gamma=1$ and $\beta=2.55(4\sqrt{2}/3\pi)$. Finally, $C=0.2(4\sqrt{2}/3\pi)$ which corresponds to a dissipation time scale of about fifteen days. The zonal forcing intensity x_1^* and the width-length ratio b of the channel are varied.

The three-component model is equivalent to that studied by DE SWART and GRASMAN (1987) except that they introduced a new time $t'=(4\sqrt{2}/3\pi)t$. For the stochastic dynamical system (4.1) this implies that if we define their vectorfield $f'_\mu(x)$, noise intensity ϵ', random contributions $d\Phi'(t')$, residence times T' and solution $Q'(x)$ of the eikonal equation we have the relations

$$\begin{aligned} f_\mu'(x) &= \frac{3\pi}{4\sqrt{2}} f_\mu(x) \quad , \ \epsilon' = \{\frac{3\pi}{4\sqrt{2}}\}^{1/2}\epsilon, \\ d\Phi'(t') &= \{\frac{3\pi}{4\sqrt{2}}\}^{1/2} d\Phi(t) \ , \ T' = \frac{4\sqrt{2}}{3\pi} T, \\ Q'(x) &= \frac{3\pi}{4\sqrt{2}} Q(x) \quad , \ K' = \frac{3\pi}{4\sqrt{2}} K. \end{aligned} \tag{4.33}$$

In all experiments we have taken a unity diffusion matrix.

For $b=1$ and $3.111<x_1^*<17.326$ the unperturbed three-component system has two stable equilibria E_1 and E_3 of high-index and low-index type and an unstable equilibrium E_2 of transitional type. The corresponding streamfunction patterns are similar to those presented in figure 2.4. We take $b=1$ (channel-width of $1.5.10^6 m$) and $x_1^*=4.19$ (zonal forcing intensity of $10ms^{-1}$) as a specific example. Considering characteristic residence times near $E_2=(1.881, 1.399, -0.462)$ we find from a linear stability analysis that $\lambda'_p=0.715$ is the only eigenvalue with positive real part. To verify expression (4.31) a large number (200) of simulations of the system starting in E_2, forced by coloured-noise processes with different values of α, have been carried out. Results are shown in figure 4.2a, where $\tilde{T}'$ is plotted against $\ln(1/\epsilon')$ for white noise and a coloured-noise process with $\alpha=3.5$. The latter value corresponds to a dimensional correlation time of about 1 day, which is representative for atmospheric flow (EGGER and SCHILLING, 1983). In agreement with (4.31) we find for small ϵ' a slope of $1.42=1/\lambda'_p$.

Next we study the residence times in the attraction domains Ω_1 and Ω_3. We distinguish between the white-noise and coloured-noise case. By using the initial-value approach to integrate along rays we obtain, with the first type of stochastic forcing, for K' in (4.33) the values

$$\begin{aligned} K'(1) \equiv K'(\Omega_1) &= 0.230, \\ K'(3) \equiv K'(\Omega_3) &= 0.518. \end{aligned} \tag{4.34}$$

Again the results were verified by means of numerical simulations. Figure 4.2b shows $\ln(T')$ as a function of $1/(\epsilon')^2$ for the domains Ω_1 and Ω_3. The data are fitted with

$$\ln T' = \tilde{K}\frac{1}{(\epsilon')^2} + \tilde{C}_0. \tag{4.35}$$

The results for $\tilde{K}$ and $\tilde{C}_0$ are

$$\begin{aligned} \tilde{K}(1) &= 0.24, \quad \tilde{C}_0(1) = 8.5, \\ \tilde{K}(3) &= 0.53, \quad \tilde{C}_0(3) = 7.0, \end{aligned} \tag{4.36}$$

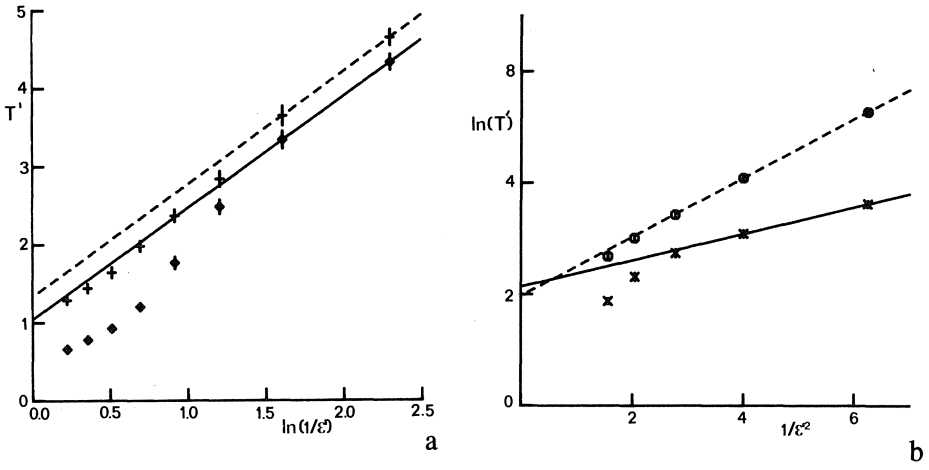

FIGURE 4.2a. Characteristic residence time $\tilde{T}'$ near E_2 as a function of $\ln(1/\epsilon')$. The solid- and dashed line show the behaviour of $\tilde{T}'$ for $\epsilon' \to 0$ for white noise and coloured noise ($\alpha = 3.5$), respectively. The data points for white-noise forcing are denoted ◆, and those for the coloured noise by +.

b. Dependence of $\ln T'$ (T' expected residence time) in Ω_1 (data points ×) and Ω_3 (data points ○) on $1/(\epsilon')^2$. The solid line and dashed line represent the asymptotic behaviour in the limit $\epsilon' \to 0$ for Ω_1 and Ω_3, respectively.

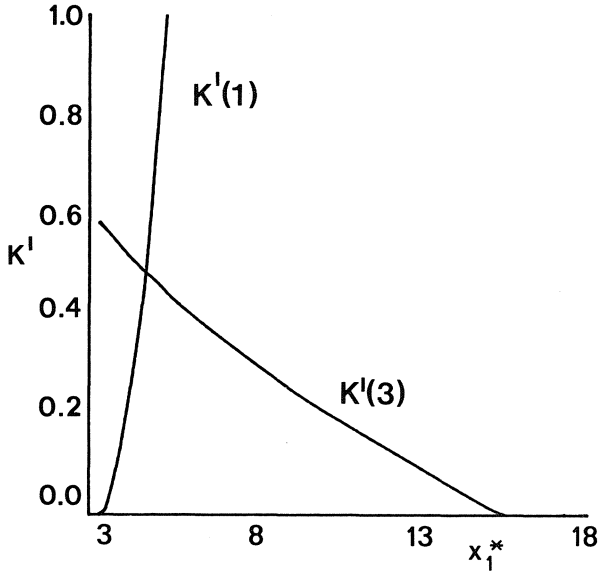

FIGURE 4.3. Dependence of $K'(1)$ and $K'(3)$ on the zonal forcing x_1^*. For further explanation see text.

with an accuracy in $\tilde{K}$ and $\tilde{C}_0$ of 10% and 25%, respectively. The $\tilde{K}$-values agree well with the values in (4.34). Furthermore it appears that the numerical constant C_0 in (4.22) has a significant influence on the expected residence times. The K'-values of (4.34) are also found with the boundary-value approach discussed in section IV.3. Since this method is more efficient we are able to present the dependence of $K'(1)$ and $K'(3)$ on the zonal forcing intensity x_1^*. The results are presented in figure 4.3. The coefficient $K'(1)$ becomes zero at $x_1^* = 3.311$, where E_1 vanishes, and $K'(3)=0$ for $x_1^* = 17.326$ where E_3 vanishes. Furthermore, it is noticed that $K'(1)$ is a strongly increasing function of x_1^*. As long as $x_1^* \lesssim 4.5$, the stochastically perturbed system spends most of its time in the low-index state, for $x_1^* \sim 4.5$ residence times in two attraction domains are of the same order while for $x_1^* \gtrsim 4.5$ the probability of finding the system in domain Ω_3 is almost zero.

Next the effect of coloured-noise forcing on the three-component model is considered for $b=1$ and $x_1^* = 4.19$. We investigate the dependence of the $K'(1)$- and $K'(3)$-values on the correlation time of the noise. In this case the initial value approach used by DE SWART and GRASMAN (1987) failed because the rays already have a strongly diverging character at some distance from E_2. However, it appears that the boundary-value approach can be used quite succesful. Results for $K'(1)$ and $K'(3)$ are presented in table 4.1, together with values for $\tilde{K}$ and $\tilde{C}_0$ obtained from numerical simulations. There is a reasonable good agreement between the analytical and simulation results.

α	$K'(1)$	$\tilde{K}(1)$ ($\pm$ 10%)	$\tilde{C}_0(1)$ ($\pm$ 25%)	$K'(3)$	$\tilde{K}(3)$ ($\pm$ 10%)	$\tilde{C}_0(3)$ ($\pm$ 25%)
1	0.259	0.28	11.0	0.760	0.68	11.3
1.75	0.241	0.26	10.6	0.627	0.61	9.8
2.5	0.236	0.24	10.8	0.575	0.55	9.3
3.5	0.234	0.24	10.2	0.530	0.53	8.4
∞	0.230	0.23	8.5	0.518	0.52	7.2

TABLE 4.1. The coefficients $K'(1)$, $\tilde{K}(1)$, $\tilde{C}_0(1)$, $K'(3)$, $\tilde{K}(3)$ and $\tilde{C}_0(3)$ for different values of α. For further explanation see text.

For $0<\epsilon\ll 1$ the expected residence times of the system in the two attraction domains increase with increasing noise memory. This can be explained as follows: the time evolution of a system, perturbed by coloured noise, will have some memory of its own. Consequently, larger correlation times cause the system to be persistently driven further away from equilibrium in an arbitrary direction. In the limit $\epsilon \to 0$ it is known that exit through the boundary of an attraction domain will only occur near the unstable equilibrium E_2. Since there is no preference for the perturbation to drive the system right away to this point, it will take a longer time on the average to reach the boundary.

The results shown are based on the assumption that the noise has a low intensity ($0<\epsilon\ll 1$). We obtained a reasonable agreement between the

asymptotic values for the expected residence times and the outcome from simulations for ϵ^2 smaller than 0.3. Estimates of ϵ for atmospheric models are given by EGGER (1981) and EGGER and SCHILLING (1983). They found $\epsilon^2 \sim 0.2$ for the three-component model considered here. In case of white-noise forcing it then follows expected residence times of about 90 days for the high-index state, 10 days for the intermediate state and about 310 days for the low-index state. These values seem to be rather large compared with observational data. They even increase by some 10% if coloured-noise forcing is applied with a correlation time of one day ($\alpha = 3.5$). We return to this point in section IV.6.

Considering the stochastically perturbed six-component model we remark that in case of coloured-noise forcing the Hamilton system (4.18) is 24-dimensional. It then appears that the computation of Q-values requires too much direct memory storage on the CDC Cyber 170-750 system. We therefore restrict our analysis to white-noise forcing. We remark that we have found the differences between white-noise and coloured-noise forcing with realistic correlation times to be small. Furthermore, in order to apply the theory of section IV.3 to this system, we note that it is valid for equilibria only. Since we know that the six-component model can have more complicated attractors than equilibria we have to select specific parameter values for our analysis.

We have investigated the sets of limit points for the values defined in the beginning of this section. The curves of singular points in the b, x_1^* parameter space are similar to those presented in figure 3.1. As long as $b \leqslant 1.54$ the model contains equilibria only. For $b = 1$ all of then are of single-mode type, i.e. they are also equilibria of the three-component subsystem. For small noise intensities characteristic residence times near the unstable equilibrium E_2 are given by (4.31) where the maximum positive eigenvalue has the same value as in the three-component model. Moreover, expected residence times in the attraction domains Ω_1 and Ω_3 of the stable equilibria E_1 and E_3 are given by (4.22) with $K(\Omega_1)$ and $K(\Omega_3)$ identical to the K-values obtained from the white noise-forced three-component model. This is because solutions of the six-dimensional Hamilton system associated with the three-component model are also solutions of the 12-dimensional Hamilton system associated with the white noise-forced six-component model. This argument has been verified by application of the boundary-value approach to both Hamilton systems. We could not estimate the values of the constants C_0 in (4.22) and d in (4.31) because numerical simulations require too much computer time.

Finally we consider the white noise-forced six-component model for $b = 1.5$ and $x_1^* = 4.19$. In this case there are two unstable equilibria E_2 and E_3 and three stable equilibria E_1, E_{4a} and E_{4b}. A sketch of the phase flow of the unperturbed system is presented in figure 3.4. The constant $K'(\Omega_1)$ has been computed by application of the boundary-value approach to the 12-dimensional Hamilton system. We obtained $K'(\Omega_1) = 0.29$, which is the same result as for the 6-dimensional Hamilton system associated with the three-component model with $b = 1.5$ and $x_1^* = 4.19$, forced by white noise. Obviously, the stochastically perturbed systems have a qualitatively similar

dynamics in this attraction domain. Considering expected residence times in the attraction domains $\Omega_{4a,b}$ of the equilibria $E_{4a,b}$ we note that the statistics in both domains are equivalent because of the symmetry of the system. We have constructed the heteroclinic orbit between the saddle points $x=E_{4a},p=0$ and $x=E_3,p=0$. Given $Q'(E_{4a})=0$ we then find from (4.18) that $K(\Omega_{4a}) = Q'(E_3)=0.01$. This value gives an estimate of the expected residence times in Ω_{4a} whenever exit occurs near E_3. Once the system is near E_3 it can leave the 'low-index attraction domain' along the unstable equilibrium E_2 and go over to the 'high index attraction domain' Ω_1. Therefore, the persistence of the low-index regime is actually measured by $K'(\Omega_3)=0.38$. This result is obtained by solving Eq. (4.19) along the heteroclinic orbit which connects the saddle points $x=E_3,p=0$ and $x=E_2,p=0$ of the Hamilton system (4.18). As discussed previously the value $K'(\Omega_1)=0.29$ is an estimate of the persistence of the high-index regime.

IV.5. A DISCRETE-STATE MARKOV MODEL OF THE ATMOSPHERIC CIRCULATION

As soon as a stochastically forced dynamical system of the type (4.6) is in statistical equilibrium, the expected residence times of the preference states yield information about the expected durances of such states. However, in this way no information is obtained about the time scale over which the transient effect of initial conditions are important. To find this time scale in general requires the solution of the full Fokker-Planck equation, but for small noise intensities it appears that most of the time the system is close to a stationary point of the unperturbed spectral model. This suggests the introduction of a discrete-state Markov process model, with which we can study the evolution of the probability distribution in time for any initial conditions. For the randomly forced three-component spectral model, studied in the previous section, we can develop such a model with three states, viz. a zonal state (1), a transitional state (2) and a blocking state (3).

Let $Q_{ij}(t)$ denote the transition probability per unit time to go from state i to state $j(i,j=1,2,3)$ at time t, let $p_i(t)$ denote the probability to be in state i at time t and let T_i be the expected residence time of this state. The latter is a measure of predictability when i is the initial state. The set of discrete-time master equations are

$$p_i(t+\Delta t) = \sum_{j=1}^{3} p_j(t)Q_{ji}(t)\Delta t \; ; \; i=1,2,3, \tag{4.37}$$

with Δt a small but finite time step. Since the sum of the probabilities is equal to one, the model can be reduced to two dynamical equations for e.g. $p_1(t)$ and $p_3(t)$ and one passive equation for $p_2(t)$. To arrive at the time-continuous model we use the identities

$$\sum_{j=1}^{3} Q_{ij}\Delta t = 1 \text{ for } i=1,2,3, \tag{4.38}$$

and take the limit $\Delta t \to 0$. The result is

$$\begin{aligned}\dot{p}_1 &= -(Q_{12}+Q_{13}+Q_{21})p_1 + (Q_{31}-Q_{21})p_3 + Q_{21},\\ \dot{p}_3 &= (Q_{13}-Q_{23})p_1-(Q_{31}+Q_{32}+Q_{23})p_3 + Q_{23},\\ p_2 &= 1-p_1-p_3.\end{aligned} \tag{4.39}$$

To specify the transition probabilities we use the results of section IV.4. There it was found that for small noise intensities the transition from the zonal state to the blocking state, and vice versa, occurs by way of the transitional state. Furthermore, given the system is in the transitional state, it has equal probability to go to the zonal state or the blocking state. Hence

$$Q_{13} = Q_{31} = 0\,, \quad Q_{23} = Q_{21} \tag{4.40}$$

must hold. The remaining unknown coefficients Q_{12}, Q_{21} and Q_{32} in the equations (4.39) can be related to the expected residence times in the following way. Define $\chi_i(t)$ as the conditional probability for the system to be in state i at time t, given it was in i at $t=0$. Since $\chi_i(t)-\chi_i(t+\Delta t)$, is the probability for exit of state i in the time interval $[t,t+\Delta t]$, it follows $-d\chi_i/dt$ as a probability density distribution over the time domain. Consequently the expected residence time is

$$T_i = -\int_0^\infty t\frac{d\chi_i}{dt} = \int_0^\infty \chi_i dt, \tag{4.41}$$

where in the last step partial integration has been applied. In this case we have

$$\begin{aligned}\chi_1(t)-\chi_1(t+\Delta t) &= \chi_1(t)Q_{12}(t)\Delta t,\\ \chi_2(t)-\chi_2(t+\Delta t) &= 2\chi_2(t)Q_{21}(t)\Delta t,\\ \chi_3(t)-\chi_3(t+\Delta t) &= \chi_3(t)Q_{32}(t)\Delta t.\end{aligned} \tag{4.42}$$

We now assume that Q_{12}, Q_{21} and Q_{32} are constants. Then solving for $\Delta t \to 0$ gives

$$\chi_1(t) = e^{-Q_{12}t},\ \chi_2(t) = e^{-2Q_{21}t},\ \chi_3(t) = e^{-Q_{32}t}. \tag{4.43}$$

In figure 4.4a a numerically computed probability density $-d\chi_2/dt$ is shown for the stochastically forced three-component model. As can be seen from figure 4.4b, a constant exponential decay rate is only found in the tail of the distribution. Nevertheless, if we accept (4.43) as a first approximation we find from (4.41) that

$$Q_{12} = \frac{1}{T_1}\,, \quad Q_{21} = \frac{1}{2T_2}\,, \quad Q_{32} = \frac{1}{T_3}. \tag{4.44}$$

Our model now consists of (4.39), (4.40) and (4.44). The general solution of this inhomogeneous linear system reads

$$\begin{bmatrix}p_1\\ p_3\end{bmatrix} = \begin{bmatrix}p_{1s}\\ p_{3s}\end{bmatrix} + \alpha_1\begin{bmatrix}u_{11}\\ u_{13}\end{bmatrix}e^{\lambda_1 t} + \alpha_2\begin{bmatrix}u_{21}\\ u_{23}\end{bmatrix}e^{\lambda_2 t}, \tag{4.45}$$

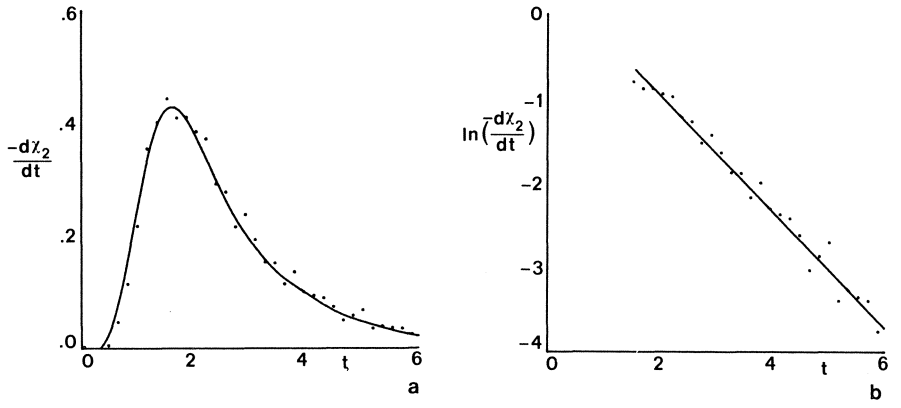

FIGURE 4.4. a. Probability density distribution $-d\chi_2/dt$ of the characteristic residence times near the equilibrium E_2 of the white noise-forced three-component model. The data points, denoted by •, are based on 2000 simulations for $b=1, x_1^*=4.19$ and $\epsilon'=0.3$.

b. $\ln(-d\chi_2/dt)$ as a function of time for the data points shown in figure 4.5a with $t>1.4$. Fitting a straight line to the data yields the linear slope -0.69 ± 0.02.

where

$$\begin{bmatrix} p_{1s} \\ p_{3s} \end{bmatrix} = \frac{1}{T_1+2T_2+T_3} \begin{bmatrix} T_1 \\ T_3 \end{bmatrix} \tag{4.46}$$

is the equilibrium point of the model, which corresponds to the stationary probability distribution. Furthermore λ_1 and λ_2 are eigenvalues of the homogeneous system, with (u_{11},u_{13}) and (u_{21},u_{23}) the corresponding eigenvectors, while α_1 and α_2 are integration constants determined by the initial conditions. It appears that λ_1 and λ_2 are real negative constants, so the stationary point is always stable.

As a specific example we have analysed the model for $T_1=9$, $T_2=1$ and $T_3=31$, which are scaled values of the explicity calculated residence times of the stochastically forced three-component model of section IV.4. The eigenvalues in this case are

$$\lambda_1 = -0.070, \quad \lambda_2 = -1.073. \tag{4.47}$$

As can be seen from (4.45) they represent a slow and fast exponential decay towards the stationary probability distribution. In figure 4.5a trajectories of the system in the p_1,p_3-phase plane are shown with initial values (1,0), (0,0) and (1,0), denoting that at $t=0$ the system is in state 1, 2 or 3 with probability 1. From the numerical experiments it follows that if the system is in state 1 or 3, the transient evolution of the probability distribution is mainly determined

by λ_1. If state 2 is the initial state the decay in p_2 is in a first instance controlled by $\lambda_2 = \mathcal{O}(1/T_2)$ and hereafter by λ_1. Thus the predictability is then lower, as the model will almost certain have undergone a transition either to state 1 or state 3. Whenever this happens the dynamics is from then on controlled by λ_1, as we have seen. This is illustrated in the figures 4.5b,c,d, which show the time evolution of the probability distribution starting in the initial states 1, 2 and 3, respectively. The dotted lines show the stationary probability distribution.

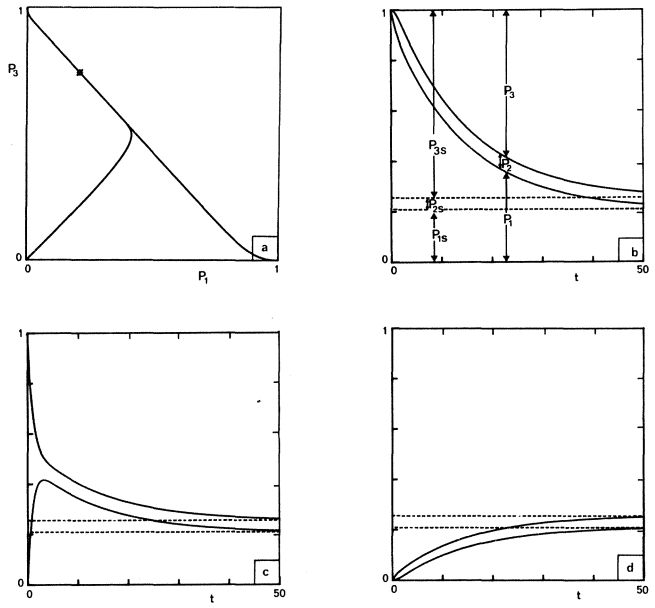

FIGURE 4.5. Evolution in time of the probability distribution of the Markov process model for $T_1 = 9$, $T_2 = 1$ and $T_3 = 31$, starting in the states 1, 2 and 3. In (a) the trajectories in the p_1,p_3-plane are shown. In (b), (c) and (d) the explicit time dependence is shown; the dotted lines represent the stationary probability distribution.

IV.6. CONCLUDING REMARKS

In this chapter we have studied the effect of stochastic perturbations on a three- and six-component spectral model of the barotropic potential vorticity equation in a beta-plane channel. The unperturbed systems have been analysed in section II.3 and chapter III, respectively. It appeared that for parameter values representative for the atmosphere multiple equilibria exist; some of them are stable, others unstable.

In section IV.2 we have parametrized the effect of the neglected modes, including additional processes not incorporated in the model, by stationary stochastic terms, being of the white-noise and coloured-noise type. We have taken the diffusion matrix to be the unity matrix. One may include the state

dependent sensitivity of the large-scale circulation model for transient perturbations by letting the components of the diffusion matrix be functions of the state variables x, but is not clear how these functions should be specified.

The perturbed system shows frequent transitions between the attraction domains of the stable equilibria of the unperturbed model. As noticed in section IV.3 for small noise intensities ($0<\epsilon\ll 1$), the system will also remain for some time in a neighbourhood of the unstable equilibria, hence the latter are significant for the dynamics of the perturbed system. As a consequence, unstable equilibria may be important for the dynamics of the large-scale atmospheric circulation. Similar results have been found by REINHOLD and PIERREHUMBERT (1982) and LEGRAS and GHIL (1985). They used higher-order deterministic spectral models of the potential vorticity equation. In their case the presence of saddle points is responsible for chaotic dynamics and regime behaviour.

A method is described to calculate the asymptotic behaviour of the expected residence times in the neighbourhood of the equilibria for $\epsilon\rightarrow 0$. BENZI et al. (1984) have carried out such an asymptotic analysis. The method we presented extends to unstable equilibria of the unperturbed system and to systems that are not necessarily of gradient type. In section IV.4 results have been presented for the three-component spectral model of atmospheric flow perturbed by noise with different correlation times. It has been found that the initial-value approach for solving the Hamilton equations is only applicable in the white-noise case. The boundary-value approach is more successful: it can handle both the coloured noise-forced three-component model and the white noise-forced six-component model. Its only limitation for practical use is the computer storage needed. Hence this method may be a useful tool in the analysis of more complicated spectral models.

Since the solution of the stochastically perturbed model remains most of the time near the three equilibria of the unperturbed system, we have formulated in section IV.5 a stochastic dynamical system which may take only three discrete states. With this time-continuous Markov model we have studied the effect of initial conditions on the evolution of the probability distribution over the three states. From the results it can be concluded that the predictability of the states is closely connected with the eigenvalues of the Markov model. In the first instance the residence times T_i yield information on the expected durance of the preference state i. In addition to this, the value $1/\lambda_1$ in (4.47) gives an indication of the time scale over which transient effects are present in the system. In this time span the initial state can be utilized in the process of computing the probability distribution over the three preference states.

We will now discuss the validity of the stochastically forced spectral equations as a model of the atmospheric circulation. In order to do so we have cast the results in the form of a three-state Markov model, see also SPEKAT et al. (1983). The latter authors developed a similar model, but used meteorological data as input to calculate transition probabilities, expected residence times, etc.. It then follows that the persistence of the zonal state E_1 and the blocking state E_3 of our model are too large (by a factor of 10) compared to the

characteristic lifes of large-scale circulation types over Central Europe. Obviously, the spectral models considered here are not a correct representation of the atmospheric circulation. We expect a better agreement if the resolution of the quasi-geostrophic spectral models is increased. Therefore, in the next chapter we will study the effect of including more modes in the spectral expansions on the dynamics of the barotropic model.

V: Predictability properties of a minimum-order atmospheric spectral model with vacillation behaviour

V.1. Introduction

It has been discussed in chapter I that the large-scale atmospheric circulation may irregularly vacillate between preferent weather regimes. Furthermore this flow has an unpredictable nature, implying that weather forecasts only have validity for a finite period of time. In this tract we investigate whether low-order spectral models represent these features. These models are of the type (1.1) and can be analysed with techniques originating from the theory of dynamical systems.

In chapter III we have found that three- and six-component models of the barotropic potential vorticity equation can have multiple preferent states. However, they do not describe transitions between the different states. This is due to the fact that the systems lack for relevant nonlinear interactions. Two processes were suggested which would help to overcome this shortcoming. The first one, adding stochastic perturbations to the spectral equations, has been investigated in chapter IV. Here we shall deal with the second suggestion: extending the deterministic model by including more modes in the spectral expansions. Legras and Ghil (1985) have studied a 25-component barotropic model in spherical geometry and found that solutions could visit different preferent regions in phase space. However, they did not determine the minimum number of modes required for the occurrence of vacillation. Here we shall derive this necessary number by analysing the physical properties of barotropic spectral models. The aim of the present study is to derive a minimum-order model, based on a rectangular truncation of the spectral expansions in wave-number space, which has for fixed parameter values multiple unstable regular solutions and a strange attractor. We expect trajectories, starting from arbitrary initial conditions, to converge to this attractor. Subsequently, they must vacillate between different preferent regions in phase space which are close to the (weakly) unstable regular solutions.

We claim that the 10-component barotropic model presented in appendix C is in fact this minimum-order model. It describes the evolution of two zonal flow profiles (a (0,1) and (0,2) mode) and four Rossby waves (the (1,1), (1,2), (2,1) and (2,2) modes). Compared to the six-component model of chapter III it contains a new type of nonlinear interaction involving three Rossby waves: the (1,1), (1,2) and (2,1) modes. In section V.2 it is shown that, due to the presence of this barotropic wave triad, all regular solutions become unstable for a range of parameter values. Attractor properties of the system are investigated in section V.3. The nontransient time series represent a flow vacillating between three weather regimes. By computing the Lyapunov exponents we shall show the existence of a global strange attractor. As discussed in WOLF et al. (1985) chaos is characterized by one or more positive Lyapunov exponents. Furthermore, essential features of the preferent regimes are given such as the corresponding flow patterns and their average duration times. A discrete-state Markov model is used to compute a time scale over which the effect of initial conditions is important. The static structure of the strange attractor, characterized by its fractal dimensions, is investigated in section V.4. The integer obtained from rounding off the Hausdorff dimension upwards estimates the actual number of degrees of freedom of the chaotic flow. The distinction between the preferent regimes is measured by the difference between Hausdorff dimension and correlation dimension.

In practice we do not know initial conditions with infinite precision. Consequently, small errors are introduced in the system which will grow during its evolution because of the chaotic dynamics. Consequently, the predictability of the flow is limited: a time scale on which it is predictable on the average is given by the reciprocal of the sum of all positive Lyapunov exponents. However, of more interest to meteorologists is the dependence of predictability on the state of the system, see TENNEKES et al. (1986). We argue in section V.5 that the local eigenvalues of the matrix derivative of the vectorfield, linearized at each point of a reference orbit, measure the local growth rates of small errors introduced on this orbit. However, this is on the condition that the time scale of error growth is small compared to the time scale on which the flow itself evolves. In that case the corresponding eigenvectors will yield information about the geographical distribution of the errors.

In section V.6 we shall study the impact of neglected short-scale waves on a planetary-scale forecast model. We shall consider our chaotic 10-component model to represent the real atmosphere and the six-component subsystem, shown in appendix C between the dashed lines, as a forecast model. For obtaining equivalence between solutions of the two systems, forcing terms must be added to the equations of the forecast model. It will appear that these forcing terms have an unpredictable nature and that they cannot be parametrized by simple stochastic processes. This conclusion is in agreement with the findings of LINDENBERG and WEST (1984) and KOTTALAM et al. (1987). We shall end with a few general remarks in the final section.

V.2. BIFURCATION ANALYSIS

Consider the 10-component barotropic spectral model of appendix C. We wish to investigate the existence of stable chaotic solutions and co-existing unstable regular solutions. Thus, trajectories should alternately visit different preferent regions in phase space close to the regular solutions. Then the model represents a flow having a finite predictability and vacillating between different weather regimes. In appendix D it is shown how these properties are investigated by using a bifurcation analysis of the stationary points and periodic solutions of the model. In this way quasi-periodic and chaotic solutions can be found.

A complete exploration of the spectral model is difficult to carry out because it contains so may nonlinear interactions. However, for our purposes a limited bifurcation analysis is sufficient. Since the model is an extension of the model studied in chapter III we expect regular solutions to be either of high-index, low-index or transitional type. Necessary conditions for the occurrence of multiple regimes are the presence of topography (γ nonzero) and a forcing in the (0,1) zonal flow component (x_1^* nonzero). It was found in section III.4 that in order to obtain unstable high-index regimes the (0,2) zonal flow mode must also be forced (x_4^* nonzero). For the instability of the low-index regimes at least one of the four wave modes must be unstable. In order to derive necessary conditions for the occurrence of these instabilities, we have sketched in figure 5.1 the three barotropic triads of the model. Two of them involve the (0,2) zonal flow mode while there is one wave triad.

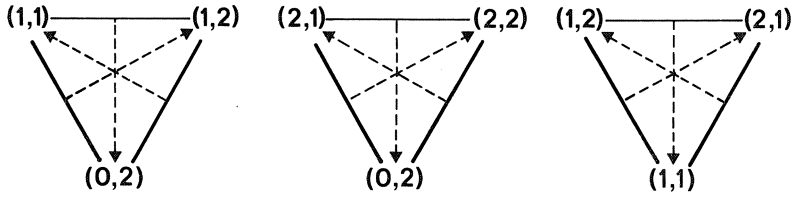

FIGURE 5.1. Schematic representation of the barotropic triads of the 10-component model. Nonlinear interactions involve two modes at a time, denoted by the solid lines. As a result of each interaction a third mode is affected, as denoted by the dashed lines.

We note that FJØRTOFT (1953) has derived a theorem stating that a participating mode in such a triad can become unstable if its wave-length is smaller than that of the second participating mode but larger than that of the third mode. The wave-lengths of the different modes are just the eigenvalues λ_j defined in (2.49 a,b). Applying the Fjørtoft theorem to the triads of figure 5.1 we obtain that for $(\sqrt{3}/2)<b<\sqrt{3}$ at least one wave mode can be unstable. Thus if we take $b=1.6, \beta=1.25, C=0.1$ and $\gamma=1$ we expect to find vacillatory behaviour for x_1^* and x_4^* sufficiently large. The physical situation corresponding to these parameter values has already been described in section II.3.

We first consider the case that $x_4^* = 0$. Although no vacillating solutions will be found, the subsequent analysis will give an idea of the types of solutions that arise and will show the importance of the wave triad. In figure 5.2 the $\hat{x}_1$- and $\hat{x}_4$-component of the stationary points of the 10-component model are shown as a function of x_1^*. It is obtained numerically by application of the continuation routines included in the software package AUTO, see DOEDEL (1986). Similar diagrams have been shown for the three- and six-component model, see the figures 2.3b and 3.2. Solutions of the three-component model are also solutions of the full model, although stability properties may differ. This does not apply to solutions of the six-component model: for nonzero amplitudes of the (1,1) and (1,2) modes the wave triad provides for a direct forcing of the (2,1) mode. In figure 5.2 three branches of single-mode equilibria occur, for which $\{\hat{x}_i = 0\}_{i=4}^{10}$; they are denoted by E_1, E_2 and E_3. Their existence is a consequence of the presence of topography, which also causes changes in the stability properties of the single-mode equilibria at ordinary bifurcation points. Here mixed-mode equilibria branch off which have nonzero $\{x_i\}_{i=4}^{10}$. Furthermore isolated branches of mixed-mode equilibria occur which have not been found previously. They are generated due to the presence of the wave triad and have been calculated by means of routines to locate zeroes of nonlinear algebraic systems, in combination with the continuation routines of AUTO. The Hopf bifurcation points in figure 5.2 are a manifestation of the barotropic instability mechanism. At these points branches of periodic orbits are generated.

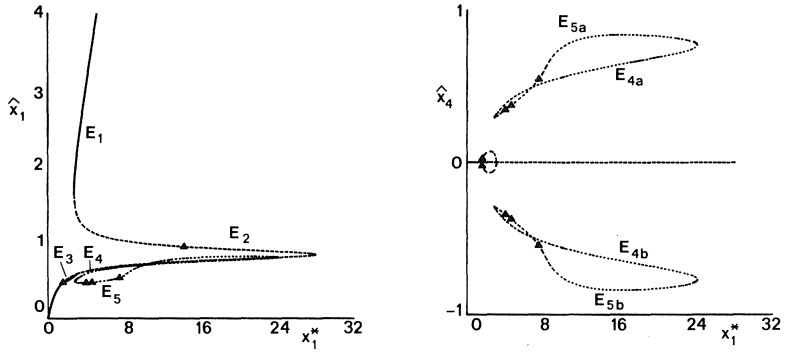

FIGURE 5.2. Stationary solutions of the 10-component model. Shown are the $\hat{x}_1$- and $\hat{x}_4$-component as a function of x_1^* for $b = 1.6, \beta = 1.25$, $C = 0.1, \gamma = 1$ and $x_4^* = 0$. A solid line denotes that the solution is stable whereas a dashed line refers to an unstable solution. Hopf bifurcation points are indicated by a triangle.

We consider the stationary points of the model for $x_1^* = 4$ in more detail. Apart from the single-mode equilibria E_1, E_2 and E_3 given in (2.59) we have the (isolated) mixed-mode equilibria

$$
\begin{aligned}
E_{4a/b} &= (0.732, -0.605, -0.340, \pm 0.384, \pm 0.018, \mp 0.069, \\
&\quad \pm 0.046, \pm 0.020, -0.042, -0.012), \qquad (5.1) \\
E_{5a/b} &= (0.581, -0.300, -0.356, \pm 0.344, \pm 0.035, \mp 0.308, \\
&\quad \pm 0.054, \pm 0.030, -0.066, -0.023).
\end{aligned}
$$

They clearly differ from the mixed-mode equilibria of the six-component subsystem given in (3.4). The streamfunction patterns of E_1, E_2 and E_3 were shown in figure 2.4. They represent a flow of high-index, transitional and low-index type, respectively. The streamfunction configurations of $E_{4a/b}$ and $E_{5a/b}$ defined in (5.1) are presented in figure 5.3. From this and figure 3.3 we see that all mixed-mode equilibria represent steady states of low-index type.

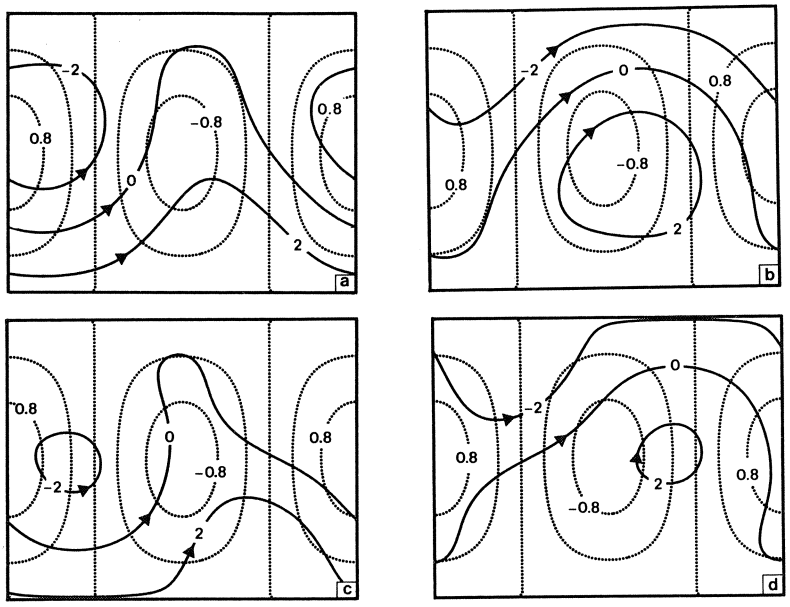

FIGURE 5.3. Nondimensional streamfunction contours (solid lines) for the equilibria $E_{4a}(a), E_{4b}(b), E_{5a}(c)$ and $E_{5b}(d)$ defined in (5.1). A difference $\Delta\psi = 1$ corresponds to a zonal transport of about $1.1.10^6 m^2 s^{-1}$. The dashed lines represent contours of topography ($10^3 m$).

We now fix $x_1^* = 4$ and consider the position and stability of the stationary points as a function of the (0,2) zonal-forcing amplitude x_4^*. Results are shown in figure 5.4 where for $x_4^* = 0$ has been started from the equilibria E_1, E_2 and E_3, respectively. Identical experiments have been discussed in section III.4 for the six-component subsystem. There it was found that for each value of x_4^* at least one stable stationary point or stable periodic orbit exists. However from figure 5.4 and table 5.1 it appears that the dynamics of the 10-component model is considerably different. We find that for $|x_4^*| > 5.752$ all

equilibria of the spectral model are unstable. Moreover, we expect that for $|x_4^*|$ somewhat larger than 5.752 the periodic solutions have also become unstable. The reason is that the large number of nonlinear interactions allow for many ways to transfer energy and enstrophy between the different modes. We will test this hypothesis in the next section.

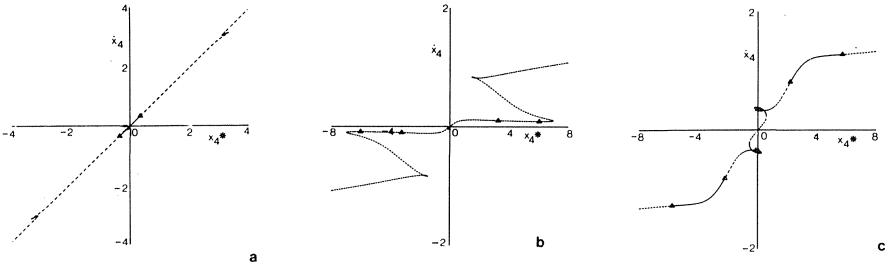

FIGURE 5.4. The $\hat{x}_4$-component of the equilibria of the 10-component model for $x_1^*=4$ as a function of x_4^*. For $x_4^*=0$ a restart is made in $E_1(a), E_2(b)$ and $E_3(c)$. Stability properties are indicated by a solid line (stable) or dashed line (unstable). The symbol Δ denotes a Hopf bifurcation point.

$\lvert x_4^*\rvert$		$\lvert x_4^*\rvert$		x_4^*	
0.	E_1 $\rightarrow -$ (0)	0.	E_2 $\rightarrow +$ (1)	0.	E_3 $\rightarrow +$ (2)
0.348	*HB* $\rightarrow +$ (2)	3.270	*HB* $\rightarrow +$ (3)	$\pm$ 0.578	*TP* $\rightarrow +$ (3)
3.346	*TP* $\rightarrow +$ (1)	6.054	*HB* $\rightarrow +$ (1)	$\mp$ 0.252	*TP* $\rightarrow +$ (2)
3.119	*TP* $\rightarrow +$ (2)	7.021	*TP* $\rightarrow +$ (2)	$\mp$ 0.009	*HB* $\rightarrow +$ (4)
$\downarrow$		1.480	*TP* $\rightarrow +$ (3)	$\pm$ 0.141	*HB* $\rightarrow +$ (2)
∞		$\downarrow$		$\pm$ 2.205	*HB* $\rightarrow -$ (0)
		∞		$\pm$ 5.752	*HB* $\rightarrow +$ (2)
				$\downarrow$	
				$\pm\infty$	

TABLE 5.1. Bifurcation and stability properties of the branches of stationary points shown in figure 5.4. Each $x_4^* \neq 0$ is a bifurcation value with the type of bifurcation indicated (*HB*: Hopf bifurcation, *TP* turning point). The sign behind the arrow denotes stabilitity properties of the equilibria between successive bifurcation values ($-$: stable, $+$: unstable). The number in brackets denotes the number of eigenvalues with positive real part.

V.3. DYNAMICAL BEHAVIOUR

V.3.1. Global analysis and scale selection

Considering the previous results we take $x_1^* = 4$ and $x_4^* = -8$ as values of the forcing for which we expect vacillating solutions. The resulting zonal velocity-forcing profile is shown in figure 5.5. It represents intense westerlies in the northern part of the channel and weaker easterlies in the southern part. Comparing it with the forcing of atmospheric flow in midlatitudes we find that our velocities and meridional gradients are unrealistically large: over $150 ms^{-1}$ and $3.10^{-4} s^{-1}$, respectively. For these parameter values three unstable equilibria exist:

$$\begin{aligned} EQ_1 &= (4.300, -0.845, 0.031, -7.856, -0.326, 0.000, \\ &\quad -0.001, 0.000, -0.003, 0.000), \\ EQ_2 &= (0.723, 2.752, -0.341, -1.085, -0.722, 0.243, \\ &\quad 0.104, -0.031, 0.250, -0.109), \\ EQ_3 &= (0.614, -3.107, -0.353, -1.323, 0.580, -0.092, \\ &\quad 0.038, 0.005, 0.151, -0.003). \end{aligned} \tag{5.2}$$

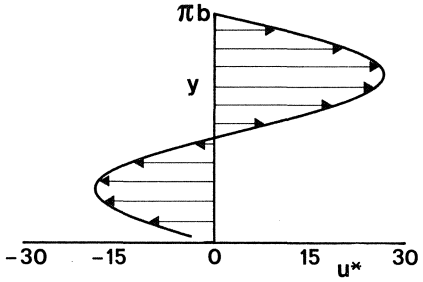

FIGURE 5.5. The function $u^*(y) = \sqrt{2} x_1^* \sin(y/b) + 2\sqrt{2} x_4^* \sin(2y/b)$ for $x_1^* = 4$ and $x_4^* = -8$, which is the zonal velocity forcing used in our experiments.

The corresponding streamfunction patterns are shown in figure 5.6. They represent a flow of high-index, transitional and low-index type, respectively. The existence of a global strange attractor was investigated by numerical integration of the spectral equations starting from different initial conditions. It was found that after a period of 500 nondimensional time units transient effects could no longer be observed and all time series had identical qualitative and quantitative properties. Obviously, the model has a global attractor and for its analysis we will use one asymptotic trajectory which is also considered in the remaining part of this chapter. In figure 5.7a a time series of the x_1-component is shown. It represents the climatology of the zonal index of the flow, as x_1 is proportional to the zonal transport between the two walls of the channel. From this figure we conclude that the model has vacillation properties: it alternately visits a high-index and low-index regime.

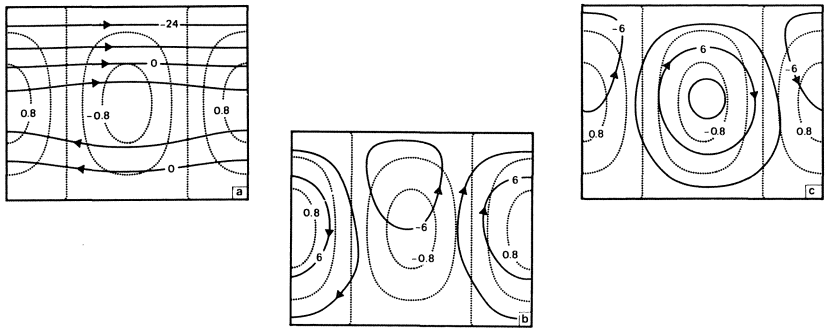

FIGURE 5.6. As figure 5.3, but for the equilibria EQ_1, EQ_2 and EQ_3 defined in (5.2).

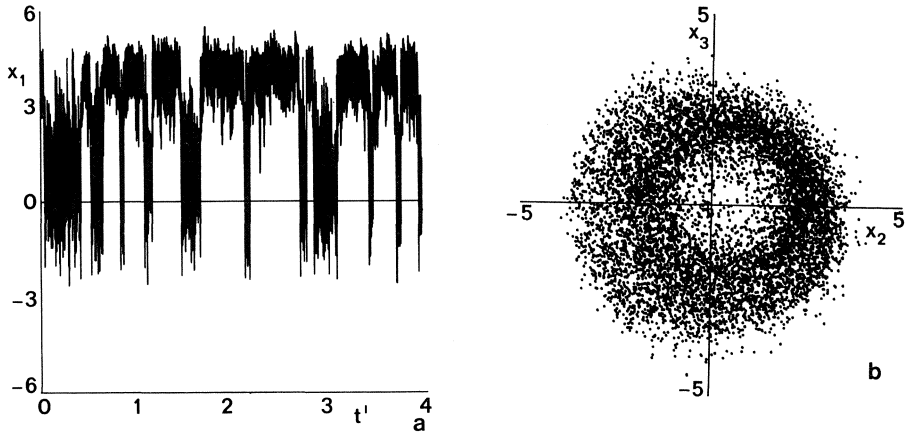

FIGURE 5.7a. Time series of the x_1-component of the 10-component model generated by a Runge-Kutta-Merson numerical integration scheme. Here $t'=(t-1000)/500$. The dimensional period shown is approximately six years.

b. Projection of the chaotic trajectory, considered at discrete times, onto the x_2-x_3 plane for the period $1000<t<3000$. The plot contains 8000 data points.

A quantitative characterization of the system behaviour is given by the Lyapunov exponents. As discussed in SCHUSTER (1987) and in section V.5 of this chapter, they measure the average exponential growth of the semi-axes of an infinitesimal error sphere along a principal orbit. Thus one or more positive Lyapunov exponents imply that nearby orbits in phase space diverge. In table V.2 the numerical results are presented for the 10-component model where we have used the method of WOLF et al. (1985).

ν_1	ν_2	ν_3	ν_4	ν_5	ν_6	ν_7	ν_8	ν_9	ν_{10}
0.34	0.18	0.04	0.	-0.06	-0.12	-0.17	-0.23	-0.38	-0.60

TABLE 5.2. Lyapunov exponents $\nu_i (i = 1.2,...,10)$ of the 10-component model for $b = 1.6$, $x_1^* = 4, x_4^*, = -8$.

Since chaos is related to the existence of at least one positive Lyapunov exponent we conclude that the model has a global strange attractor. The reciprocal of the least negative exponent defines a time scale T_t on which transient effects are important. Here we have $T_t \sim 17$, which gives an a posteriori justification for the assumption that for $t > 500$ time series are not affected by the choice of the initial condition.

A different representation of the model behaviour is obtained by consideration of the state variables at discrete times. In figure 5.7b results are shown for the x_2- and x_3-components of the asymptotic trajectory for $1000 < t < 3000$ with a time increment $\Delta t = 0.25$ between the successive data points. The figure shows the climatology of the (1,1) mode which is the longest wave present in the model. From this it seems that the static structure of the attractor in phase space resembles a distorted torus. This suggests that the strange attractor is generated due to the Ruelle-Takens-Newhouse scenario. For a detailed discussion of this route to chaos we refer to SCHUSTER (1987) and THOMPSON and STEWART (1986). Briefly it is described as follows, see figure 5.8. Consider attractor properties of the dynamical system with increasing values of a forcing parameter. At first we have a branch of stable stationary points. It becomes unstable at a Hopf bifurcation point, causing the generation of a branch of stable periodic orbits. At its turn this branch becomes unstable due to a torus bifurcation. We then observe stable quasi-periodic motion having two fundamental frequencies f_1 and f_2 with f_1/f_2 irrational, see appendix D. The next bifurcation generates a third frequency, but the corresponding quasi-periodic motion is generally unstable and chaos will be observed instead.

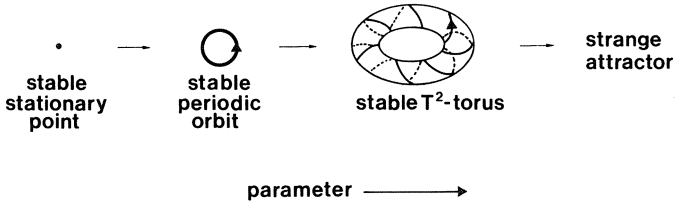

FIGURE 5.8. The Ruelle-Takens-Newhouse route to chaos.

The bifurcation route leading to chaos in our model has been investigated by calculation of the Lyapunov exponents with decreasing negative values of the forcing parameter x_4^*. It follows that for $x_4^* = -7$ there are two positive exponents which disappear at $x_4^* = -6.5$. Here we obtain two zero exponents

indicating that the motion is quasi-periodic (WOLF et al. 1985). From these results we conclude that the strange attractor is indeed generated by the Ruelle-Takens-Newhouse scenario.

The squared amplitudes of the (0,1),(1,1), (0,2), (1,2), (2,1) and (2,2) modes included in the 10-component model are given by x_1^2,$(x_2^2+x_3^2)$,x_4^2, $(x_5^2+x_6^2)$,$(x_7^2+x_8^2)$ and $(x_9^2+x_{10}^2)$, respectively. From the analysis of their nontransient time series we find that the mean intensities of the (0,1), (1,1) and (0,2) modes (having wave-lengths 8000 km, 4240 km and 4000 km) are much larger than the mean intensities of the (1,2), (2,1) and (2,2) modes (having wave-lengths 3123 km, 2386 km and 2120 km). Obviously most energy is contained in the long waves. This scale selection may be a consequence of the energy cascade from the small scales to the large scales which occurs in quasi-geostrophic turbulent flow (TENNEKES, 1985; PEDLOSKY, 1987). Here we define the (0,1), (1,1), and (0,2) modes as the planetary-scale modes and the other modes as the synoptic-scale modes.

Apart from the distinction between spatial scales it appears that the system contains two different time scales. In figure 5.9a a smoothed sample spectrum is presented of the time series $x_1(t')$ of figure 5.7a.

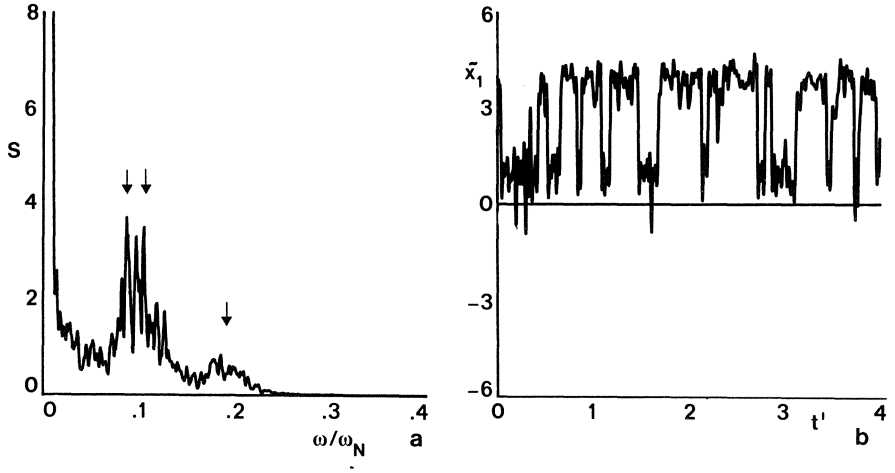

FIGURE 5.9a. Distribution of the variance in the time series $x_1(t')$ of figure 5.7a over the spectral frequencies $\omega=2\pi/T$ where T is the period. Here $\omega_N=\pi/\Delta t$ is the Nyquist frequency with $\Delta t=0.25$ the time increment between successive data points. It is the highest frequency which can be identified by the Fast Fourier Transform (PRIESTLY, 1981). The arrows indicate preferent oscillation frequencies which correspond to the three weather regimes, see section V.3.2.

b. Low-frequency part $\tilde{x}_1(t')$ of the time series $x_1(t')$ of figure 5.7a, obtained from adapting data points to an ideal low-pass filter which removes all frequencies $\omega/\omega_N>0.04$ (dimensional periods smaller than two weeks).

It shows the distribution of the variance in the zonal index over the spectral time frequencies. It appears that most variance is contained in the low-frequency domain $0<\omega/\omega_N<0.04$ (dimensional periods larger than two weeks). If we adapt the time series of figure 5.7a to an ideal low-pass filter, which removes all frequencies $\omega/\omega_N>0.04$, the result is the time series shown in figure 5.9b. On this long time scale the vacillation behaviour is still present but the rapid oscillations (with time scales of a few days) have disappeared. The latter phenomena will be discussed in the next subsection.

We have carried out test runs of the model for the same parameter values but without the wave-triad interactions. In these cases no vacillating solutions are obtained. This suggests that the presence of wave triads, which provide for interactions between different scales of motion, is a necessary condition for the occurrence of vacillation in spectral models of the atmospheric circulation.

V.3.2. Classification and characterization of weather regimes

The dynamics of the 10-component model differs considerably from that of the spectral models discussed in REINHOLD and PIERREHUMBERT (1982) and LEGRAS and GHIL (1985). In these papers the preferent flow regimes are characterized by a quasi-stationary planetary-scale flow. For our model we have considered the evolution speed of the flow, defined as the norm of the vectorfield. Furthermore the distance of each point at the nontransient trajectory to the equilibria EQ_1,EQ_2 and EQ_3 defined in (5.2) has been calculated. It appears that these quantities are never small, hence we conclude that the unstable equilibria are not of dynamical significance.

It seems that the individual regimes in our model are characterized by oscillatory behaviour with typical periods of a few days. In phase space the trajectories are attracted by unstable high-frequency periodic orbits of the system. The solutions remain for some time near these orbits until they are repelled and move away along the low-dimensional unstable manifold towards another unstable periodic orbit.

We distinguish between three different preferent regimes. The first is of high-index type: the x_1-component has positive maxima and minima. The second regime is of low-index type, during which the x_1-component oscillates between positive maxima and negative minima. Finally a third regime can be identified which is necessarily visited if a transition occurs from the high-index to the low-index regime or vice versa. Once the system is in the transitional regime it may also return to the original regime. In figure 5.10a,b time series are shown of the zonal index for a typical high-index and low-index situation. We do not show results for the transitional regime because it is visited by the system for periods which are very short compared to the time intervals shown. In figure 5.10c a sketch of the unstable periodic orbits, representing preferent regions in phase space, is shown as a projection onto the x_2-x_3 plane. The high-index regime is characterized by strong westerlies, a zonal index which is positive and by planetary waves propagating through the channel. During a low-index situation zonal flows are weaker and the zonal index alternates between positive values (eastward transport) and negative values (westward

transport). Furthermore, it follows from figure 5.10c that the planetary wave is more or less trapped. Since its phase with respect to the topographic maximum varies between 45° and 300°, the wave does not propagate throughout the entire channel. Each regime has its own period of transient oscillations: they are 2.6, 3.9 and 5.4 for the high-index, transitional and low-index regime, respectively. The corresponding values for ω/ω_N (0.17, 0.13 and 0.09) occur as peaks in the sample spectrum, see the arrows in figure 5.9a.

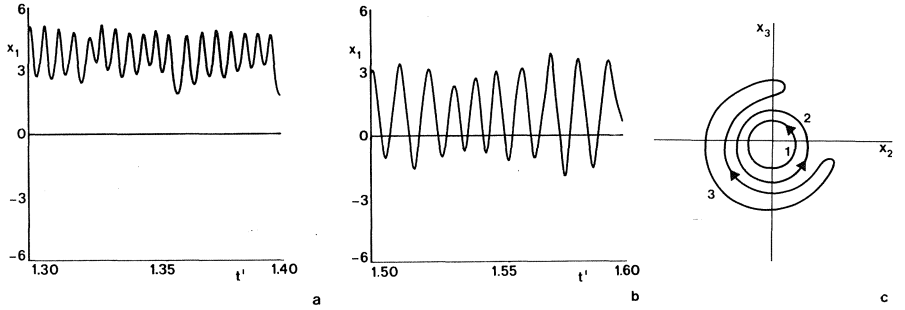

FIGURE 5.10a. Blow-up of figure 5.7a for $1.3<t'<1.4$ where the flow is of high-index type.

b. Blow-up of figure 5.7a for $1.5<t'<1.6$ where the flow is of low-index type.

c. Projection onto the x_2-x_3 plane of unstable periodic orbits to which solutions of the model are attracted (1: high-index orbit, 2: orbit of transitional type, 3: low-index orbit).

The mean residence times of the system in the different preferent regions in phase space give the mean life times of the weather regimes. They have been calculated by analysis of an asymptotic trajectory of the model, using the classification scheme discussed in section V.3.2. The results are

$$T_1 = 85.4, \quad T_2 = 1.5, \quad T_3 = 28.5 \tag{5.3}$$

for the mean residence times T_i in the high-index state ($i=1$), transitional state ($i=2$) and low-index state ($i=3$), respectively. They yield information about the probability of finding the system in a specific regime. In practice we are given an initial condition on the attractor, hence we know in which regime the system is at $t=0$. The evolution of the probability distribution over the regimes can be studied once we consider the vacillation behaviour of the spectral model as a stochastic process. In that case we may adapt the discrete-state Markov process model developed in section IV.5. Its dynamics is such that during a transition from state 1 to 3 or vice versa the system must visit state 2 and once it is in this state it has equal probability to go to state 1 or state 3. We recall the equations

$$\begin{aligned} \dot{p}_1 &= -(Q_{12}+Q_{21})p_1 - Q_{21}p_3 + Q_{21}, \\ \dot{p}_3 &= -Q_{21}p_1 - (Q_{32}+Q_{21})p_3 + Q_{21}, \\ p_2 &= 1-p_1-p_3, \end{aligned} \tag{5.4}$$

where p_i is the probability for the system to be in state i and Q_{ij} the transition probability per unit time for the system to go from state i to state j. Assuming that the Q_{ij}'s are constants (see the discussion in section IV.5) we have

$$Q_{12} = \frac{1}{T_1}\,, \quad Q_{21} = \frac{1}{2T_2}\,, \quad Q_{32} = \frac{1}{T_3} \tag{5.5}$$

The solution of the linear inhomogeneous system (5.4) is given in (4.47). It represents an exponentially decay towards the stationary probability distribution where the decay rates are measured by the two real eigenvalues λ_1 and λ_2 of the homogeneous system. They follow from (5.3)-(5.5) and read

$$\lambda_1 = -0.023\,, \quad \lambda_2 = -0.369. \tag{5.6}$$

We conclude that λ_1^{-1} (which is about fifty days in dimensional units) is a time scale on which the Markov model (5.4) yields more information about the system than the stationary probability distribution.

V.4. Static structure of the strange attractor and degrees of freedom of the flow.

Once the spectral system has settled down on its strange attractor only specific flow configurations are observed, because the attractor is confined to a subdomain of the phase space. Generally, the structure of the attractor is found from partitioning the N-dimensional phase space in cells with volume l^N and next generating a long time series of the chaotic system. From this we compute the probability p_i of finding a point of the attractor in cell-number i $(=1,2,\ldots,M(l))$. It is defined as

$$p_i = \lim_{t\to\infty} \frac{t_i}{t}\,, \quad \sum_{i=1}^{M(l)} p_i = 1, \tag{5.7}$$

where t is the length of the time series and t_i the time spend by the trajectory in cell i. We obtain a continuous distribution in the limit $l\to 0$. However, in practice this method meets serious difficulties because the boundary of a strange attractor is fractal and self-similar: its structure is frayed and is repeated on any (even microscopic) scale.

A global characterization of the static structure of strange attractors is given by its dimension of the (sub)space containing the whole attractor (Farmer et al., 1983). Dimensions of strange attractors are in general nonintegers because of their complicated structure. As shown by Hentchel and Procaccia (1983) there exists an infinite number of fractal dimensions $D^{(k)}$ which are related to the k-th powers of p_i via

$$D^{(k)} = \lim_{l\to o} \frac{1}{k-1} \frac{\ln[\sum_{i=1}^{M(l)} p_i^k]}{\ln l}\,, \quad k=0,1,2,\ldots\,. \tag{5.8}$$

We shall consider $D^{(0)}, D^{(1)}$ and $D^{(2)}$, which have a clear interpretation and can be computed relatively easy, in more detail. First we study the Hausdorff

dimension

$$D^{(0)} = -\lim_{l\to 0} \frac{\ln[M(l)]}{\ln l}. \tag{5.9}$$

It measures the exponential increase of the number of cells $M(l)$ with volume l^N, needed to cover the attractor, with decreasing l. The integer obtained from rounding off the value of $D^{(0)}$ upwards is defined as the embedding dimension. This is the lowest integer dimension of a subdomain containing the whole attractor. Physically, it gives the actual number of degrees of freedom of the flow represented by the spectral model. In other words the embedding dimension gives the number of determining modes needed to describe a turbulent flow, as is discussed in CONSTANTIN et al. (1985).

The Hausdorff dimension does not depend on the probability distribution, hence it does not yield information about the inhomogeneous structure of the strange attractor. Therefore it is useful to consider other dimensions. The next one in the hierarchy (5.8) is

$$D^{(1)} = \lim_{l\to 0} \frac{-\sum_{i=1}^{M(l)} (-p_i \ln p_i)}{\ln l} \equiv \lim_{l\to 0} \frac{-I(l)}{\ln l}. \tag{5.10}$$

This expression is obtained from (5.8) by expanding its right-hand side in powers of $(k-1)$ and making use of (5.7). Here the contribution of each cell is weighted by the factor $(-p_i \ln p_i)$. It can easily be shown that $D^{(1)} \leqslant D^{(0)}$, the equal sign holding if the attractor is homogeneous ($p_i = [M(l)]^{-1}$). Thus the difference between $D^{(1)}$ and $D^{(0)}$ measures the inhomogenity of the attractor. Since $I(l)$ in (5.10) is the information needed to locate the trajectory in a specific cell (SCHUSTER, 1987), $D^{(1)}$ is called the information dimension. It measures the exponential growth of information gain needed if $l \to 0$. In GRASSBERGER (1986) it is shown that an upper bound for $D^{(1)}$ is given by

$$D_{KY} = j + \frac{\sum_{i=1}^{j} \nu_i}{|\nu_{j+1}|}, \quad 0 < \sum_{i=1}^{j} \nu_i < |\nu_{j+1}|, \tag{5.11}$$

where $\{\nu_i\}_{i=1}^N$ are the Lyapunov exponents in decreasing order. It was conjectured by KAPLAN and YORKE (1977) that

$$D_{KY} = D^{(0)}, \tag{5.12}$$

which gives a way to compute the Hausdorff dimension numerically. The correctness of (5.12) has been verified for simple dynamical systems for which an alternative computation of $D^{(0)}$ can be carried out using a box-counting algorithm.

The information dimension is difficult to calculate, but it can be done rela-

tively easy for the correlation dimension

$$D^{(2)} = \lim_{l\to 0} \frac{\ln[\sum_{i=1}^{M(l)} p_i^2]}{\ln l}, \tag{5.13}$$

since

$$\sum_{i=1}^{M(l)} p_i^2 = \lim_{N_1\to\infty} \frac{1}{N_1^2} \sum_{i=1}^{N_1}\sum_{j=1}^{N_1} H[l-|x_i-x_j|] \equiv C(l). \tag{5.14}$$

Here $x_i (i=1,2,...,N_1)$ are points on the attractor and H is the Heavyside function. The correlation integral $C(l)$ is equivalent to the probability that two randomly chosen points on the attractor are within distance l and can be computed from a long time series. It appears that $D^{(2)} \leqslant D^{(1)}$, hence the correlation dimension is a lower bound for the information dimension.

We have computed both $D^{(0)}$ and $D^{(2)}$ for our 10-component model. From table 5.1, (5.11) and (5.12) we obtain for the Hausdorff dimension $D^{(0)}=7.91$. Consequently the embedding dimension of the strange attractor is 8. From this result we conclude that a model with eight degrees of freedom will represent the global strange attractor. In this specific case the model can be derived from the model of appendix C by neglecting the x_9- and x_{10}-components. The reduction does not affect the presence of topographic instability, barotropic instability and of the wave triad in the spectral model. Indeed, time series of this 8-component model are chaotic and show vacillatory behaviour. The reason we propose the 10-component model as minimum-order model containing a global strange attractor is that we a priori assume a rectangular truncation in wave-number space.

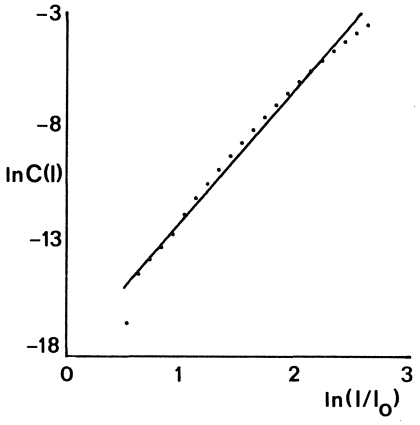

FIGURE 5.11. Correlation integral of the 10-component model. Here $l_0=0.1$, the symbols • denote data points and the straight line is the result of a least-square fitting.

In figure 5.11 the logarithm of the correlation integral $C(l)$ is shown as a function of the logarithm of the cell-size l. The linear slope for small l yields $D^{(2)}=5.8\pm0.8$. The rather large error estimate is an indication that points do not lie on a well-defined straight line. This is probably due to the finite length of the time series (Takens, pers. comm.). The correlation dimension is considerably smaller than the Hausdorff dimension. This implies that the attractor is strongly inhomogenous, which is consistent with the observations that trajectories spend most of their time in different preferent regions in phase space.

V.5. The predictability problem

V.5.1. Mathematical formulation

As already discussed in chapter III, a property of deterministic chaotic systems is their sensitive dependence on initial conditions. It appears that initially nearby orbits in phase space exponentially diverge during the evolution of the system. Since initial conditions are never known with infinite precision this implies that the future evolution of a flow represented by a chaotic spectral model can only be predicted for a finite period of time. In this section we will consider the effect of errors introduced in the initial conditions upon the predictability properties of the 10-component model. It is a dynamical system of the type

$$\dot{x} = f_\mu(x) = A + \underline{B}\cdot x + \underline{\underline{C}} : xx \quad \text{in } \mathbb{R}^N. \tag{5.15}$$

In this case (see appendix C) $N=10$, the vector A represents the external forcing, the linear terms include the beta effect, topography and dissipation while the nonlinear contributions describe the advection of vorticity by the flow.

In practice we obtain initial conditions x_0 for the atmospheric circulation from the adaption of observational data. We then define $x(t)$, with $x(0)=x_0$, as the principal orbit of (5.15). However, x_0 will generally differ from the true initial condition. Thus it becomes worthwhile to introduce a continuum of orbits $\tilde{x}(t)$ starting from the initial conditions $\tilde{x}(0)=x_0+\delta a$ where a is a vector with $|a|=1$ and $\delta<<1$. The set of $\tilde{x}(0)$ defines an 'error' sphere with center x_0 and radius δ. We wish to study the evolution of this error sphere along the principal orbit for different values of x_0 and δ. This is done by deriving dynamical equations for the deviations

$$\epsilon(t) = \tilde{x}(t) - x(t). \tag{5.16}$$

Since both $\tilde{x}(t)$ and $x(t)$ are solutions of (5.15), we have

$$\dot{\epsilon} = [\underline{B} + 2\underline{\underline{C}}\cdot x(t)]\cdot\epsilon + \underline{\underline{C}} : \epsilon\epsilon\,, \quad \epsilon(0)=\delta a. \tag{5.17}$$

The contributions on the right-hand side of (5.17) are linear, quasi-nonlinear and nonlinear, respectively. In order to determine the error evolution, an infinite number of solutions of (5.17) starting from each point of the error sphere are required. This complication is met by taking either the limit of

infinitesimal small error spheres ($\delta \to 0$) or by confining our analysis to a finite time interval $[0,t_c]$ on which the errors are small ($0<|\epsilon(t)|\ll 1$). Under these conditions the system (5.17), can be linearized. By setting

$$y = \epsilon/\delta\ ,\quad \underline{D}(t)=\underline{B}+2\underline{\underline{C}}\cdot x(t)=\tilde{\nabla} f_\mu(x(t)), \tag{5.18}$$

where $f_\mu(x)$ is given in (5.15) and the tilde denotes a transposed matrix, we obtain

$$\dot{y} = \underline{D}(t)\cdot y\ ,\quad y(0)=a. \tag{5.19}$$

This system describes the dynamics of first-order variations on the principal orbit. Note that matrix D is actually the matrix derivative of the vectorfield $f_\mu(x)$. Since it is quasi-nonlinear, N independent initial conditions are sufficient to determine the error evolution. The solution of (5.19) is

$$y(t) = \lceil \exp\{\int_0^t D(t')dt'\}\rceil \cdot y(0) = \underline{\Phi}(t)\cdot y(0), \tag{5.20}$$

where $\lceil\cdot\rceil$ denotes a time-ordening product (VAN KAMPEN, 1985) and $\Phi(t)$ the fundamental matrix. From this we conclude that the eigenvalues $\tilde{\lambda}_i(t)(i=1,2,...,N)$ of the matrix

$$\underline{E}(t) = \frac{1}{t}[\underline{\Phi}(t)-I] \tag{5.21}$$

are the mean error growth rates over the time interval $[0,t]$. Here I denotes the $(N\times N)$ unity matrix. In the subsequence the physical implications will be discussed.

V.5.2. Characterization by Lyapunov exponents and spatial error growth.
In WOLF et al. (1985) Eqs. (5.19) are considered in the limit $\delta \to 0$ and $t \to \infty$. In this case the system is characterized by its Lyapunov exponents $\{\nu_i\}_{i=1}^N$ which measure the long-term average exponential growth rates of the semi-axes of the error sphere. The sum of all exponents is the time-averaged divergence of the vectorfield which is negative for dissipative dynamical systems. Chaos is indicated by one or more positive Lyapunov exponents. It is difficult to associate a direction in phase space with a given exponent since the orientation of the deforming error sphere varies in a complicated way through the attractor. We only know that one exponent is identically zero and measures the slow error growth along the principal orbit.

The numerical results for the Lyapunov exponents of our chaotic spectral model were already presented in table 5.1 in section V.3. From this a mean time scale can be derived on which the system is predictable on the average. It reads

$$T = \frac{1}{K}\ln[|\epsilon(0)|^{-1}], \tag{5.22}$$

where the Kolmogorov entropy K is the sum of all positive Lyapunov exponents and $|\epsilon(0)|$ the norm of the initial error (SCHUSTER, 1987). For the

natural choice $|\epsilon(0)|=0.1$ we obtain a time scale of five days in dimensional units. This seems a reasonable value for the time scale on which the large-scale atmospheric circulation is predictable on the average.

The significance of Lyapunov exponents is limited, for their definition does not include the effect of initial conditions and the direction of the initial error in phase space. In practice meteorologists are also interested in local growth rates and the spatial distribution of error growth for different initial conditions. As noted in section V.5.1 this dependence is investigated from an eigenvalue-eigenvector analysis of the matrix $E(t)$ defined in (5.21). In the limit $t\to 0$ this matrix is approximated by $D(0)$. Obviously, the eigenvalues of the matrix derivative $D(t)$ of the vectorfield along the principal orbit measure the local exponential growth rates. The largest real part λ_m of all eigenvalues estimates the maximum growth rate and thus measures the reciprocal of the skill of a specific forecast. In figure 5.12 λ_m is shown as a function of time for the asymptotic chaotic trajectory of the 10-component model.

It appears that the growth rates vary strongly with time, implying that the local predictability properties strongly depend on the initial conditions. During the periods that λ_m is negative deviations between the true and approximate orbit become smaller. Relating this fact to weather predictions we state that during periods in which λ_m is negative it might be preferable to continue a previous forecast run instead of starting a new run. This is because small errors, introduced in the forecast model by an imperfect initial condition, have decreased during the integration. Thus, a re-initialisation would probably result in a larger difference between the true and the observed state. In principle λ_m can be computed for any spectral forecast model although computational difficulties will arise because of the large number of degrees of freedom.

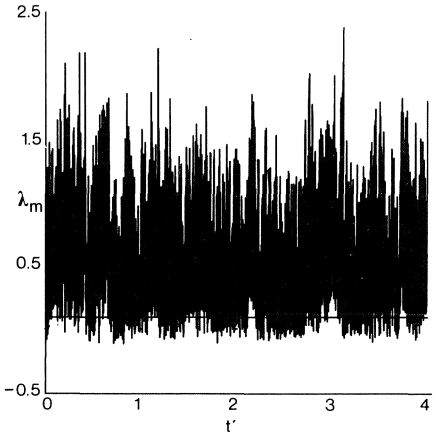

FIGURE 5.12. The maximum real part λ_m of the eigenvalues of the vectorfield linearized at each point of the chaotic trajectory of the 10-component model.

We have that

$$\bar{\lambda}_m = \lim_{t\to\infty} \frac{1}{t} \int_0^t \lambda_m(t')dt' \tag{5.23}$$

is an upper bound for the largest Lyapunov exponent. This is because the eigenvector corresponding to λ_m always gives the direction of maximum growth rate in phase space while the direction associated with λ_1 varies in a different way through the attractor. For our spectral model we have $\bar{\lambda}_m = 0.72$ while $\lambda_1 = 0.34$, see table 5.1. We may distinguish between error growth in the different preferent regimes. This was done by computing $\bar{\lambda}_m$ for the high-index (1), intermediate (2) and low-index regime (3). The results are $\bar{\lambda}_m(1) = 0.63$, $\bar{\lambda}_m(2) = 1.08$ and $\bar{\lambda}_m(3) = 0.82$. These values indicate that during a high-index flow the local error growth is small compared to the growth rates in the other regimes.

LEGRAS and GHIL (1985) argue that λ_m^{-1} is a local time scale of error growth. Generalizing this result, we state that the eigenvector(s) corresponding to the eigenvalue(s) with real part λ_m define the geographical distribution of the most probable error evolution over the physical domain. We have investigated the validity of these hypotheses for the 10-component model by integrating Eqs. (5.19) for several starting points (x_0) on the principal orbit. The $N(=10)$ independent initial conditions were taken to be the normalized eigenvectors corresponding to the eigenvalues of matrix $D(0)$. Eqs. (5.19) were integrated until the prediction time $t = T_p$ where the norm of the error is increased with a factor e. It appears that the dimensional prediction times vary between one and four days with an average of two days. No indication was found that T_p is given by $\lambda_m(0)^{-1}$. Furthermore the fastest growing error could not be related to an initial perturbation along the eigenvector(s) associated with $\lambda_m(0)$. This absence of correlations in our spectral model is due to the fact that the time scale on which the flow evolves is short compared to the time scale on which errors grow. Thus the direction in phase space associated with maximum instability changes much faster than the errors growing in a fixed direction. We expect that if

$$\eta \equiv \frac{|f_\mu(x_0)|}{\lambda_m(0)} \ll 1, \tag{5.24}$$

with $|f_\mu(x_0)|$ the norm of the vectorfield, $\lambda_m(0)^{-1}$ estimates the local prediction time of the system. This condition is never satisfied in our model: we find $\eta = \mathcal{O}(10)$. Instead we must apply an eigenvalue-eigenvector analysis to the matrix $E(t)$ defined in (5.21), as remains to be investigated. We finally remark that we expect η in (5.24) to be small in the models of REINHOLD and PIERREHUMBERT (1982) and LEGRAS and GHIL (1985), which show long periods of quasi-stationary behaviour.

V.6. Modelling the feedback between planetary-scale flow and synoptic-scale eddies

V.6.1. Formulation of the closure problem

From the results of the previous section it follows that the predictability of flows described by chaotic spectral models is limited. This is because small errors in the initial condition rapidly grow during the time evolution due to the chaotic dynamics. The same occurs to errors introduced by the finite difference scheme which is used to integrate the spectral equations numerically. On the other hand the predictability properties may also be affected by additional forcing mechanisms represented by $F(t)$ in Eqs. (1.1). They describe the effect of the modes and the physical processes not incorporated in the model. It is clear that an appropriate parametrization of the $F(t)$ would increase the validity of spectral forecast models.

In chapter IV of this tract we have adapted two types of ad hoc parametrization: the $F(t)$ were assumed to be Gaussian white noise and coloured noise, respectively. These choices are justified by the studies of Egger and Schilling (1983, 1984), Kruse and Hasselman (1986), and Barnett and Roads (1986) where observational data are compared with the results of spectral forecast models. From a theoretical point of view, Lindenberg and West (1984) and Kottalam et al. (1987) have studied the sole effect of neglected modes on truncated spectral models of the barotropic potential vorticity equation. They conclude that the resulting forcing terms have a stochastic nature. However, they cannot be parametrized by the simple processes considered in chapter IV.

In this section we will study properties of forcing terms which account for the effects of the neglected modes. Consider a finite-dimensional spectral model of the type

$$\dot{\tilde{x}} = \tilde{f}_\mu(\tilde{x}) \text{ in } \mathbb{R}^M, \tag{5.25}$$

where $\tilde{x}=(x_1,x_2,...,x_M)$ and $\tilde{f}_\mu(\tilde{x})$ is an M-dimensional vectorfield depending on $\tilde{x}$ and on parameters $\mu=(\mu_1,\mu_2,...,\mu_m)$. This system is assumed to give an *exact* representation of the atmospheric circulation. We now define $x=(x_1,x_2,...,x_N)$ as the planetary-scale modes and $y=(x_{N+1},x_{N+2},...,x_M)$ as the synoptic-scale modes. We recast (5.25) as

$$\boxed{\dot{x} = f_\mu(x)} + g_\mu(x,y), \tag{5.26a}$$

$$\dot{y} = h_\mu(x,y). \tag{5.26b}$$

Here $f_\mu(x)$ and $g_\mu(x,y)$ are N-dimensional vectorfields and $h_\mu(x,y)$ is an $(M-N)$-dimensional vectorfield. We define the planetary-scale subsystem in (5.26) between the dashed lines as our forecast model. Note that $g_\mu(x,0)=0$ by definition, but $h_\mu(x,0)\neq 0$, hence solutions of the subsystem are not solutions of the full model. In order to obtain equivalence between solutions of the forecast model and solutions of the full model projected onto the N retained modes, forcing terms $F(t)$ must be added to the forecast model. In

this case Eqs. (5.26a) can be considered as a dynamical system of the type (1.1) where

$$F(t) = g_\mu(x(t), y(t)). \tag{5.27}$$

They follow from an integration of the full model (5.26).

V.6.2. Results for the 10-component model

Here we define the 10-component barotropic spectral model of appendix C as the full model (5.26), hence $M=10$. As shown in section V.3 its solutions represent a flow resembling the large-scale atmospheric circulation. We take the six-component model in appendix C between the dashed lines as our forecast model, thus $N=6$. The three-component model is not appropriate because it cannot resolve the important forcing in the (0,2) zonal-flow mode. The stationary points of the six-component model for the parameter values $b=1.6$, $x_1^*=4$ and $x_4^*=-8$ are

$$\begin{aligned} Eq_1 &= (4.301,\ -0.846,\ 0.031,\ -7.855,\ -0.327,\ 0.000), \\ Eq_2 &= (0.902,\ 1.820,\ -0.323,\ -0.455,\ -0.701,\ 0.360), \\ Eq_3 &= (0.728,\ -2.498,\ -0.341,\ -0.758,\ 0.490,\ -0.150). \end{aligned} \tag{5.28}$$

Comparison with the results for the full model (see (5.2)) shows clear differences in the numerical values. Furthermore, Eq_3 is stable in the six-component model whereas EQ_3 is unstable in the 10-component model. Obviously the dynamics of the two models are considerably different.

From the equivalence between (5.26) and the model of appendix C it is possible to compute the six forcing terms defined in (5.27). They consist of a linear as well as a nonlinear part. The linear contributions, only present in the (1,2) modes, are due to the interactions between flow and topography not resolved by the subsystem. The nonlinear terms in the (1,1) and (1,2) modes are due to the wave triad, the nonlinearity in the (0,2) component comes in from the triad interaction between the (0,2), (2,1) and (2,2) modes. It can directly be seen that the (0,1) component is not forced, hence $F_1 \equiv 0$. The remaining five components have been computed along the asymptotic trajectory of the 10-component model considered throughout this chapter. Their time series are shown in figure 5.13. Clearly they have random character.

We have analysed the statistical properties of the time series by computing

$$\begin{aligned} \overline{F_i} &= \frac{1}{T}\int_0^T F_i(t)dt\ ,\ \ \overline{F_i^2} = \frac{1}{T}\int_0^T F_i(t)^2 dt\ , \\ \mu_{r,i} &= \frac{1}{T}\int_0^T \overline{[F_i(t)-\overline{F_i}]^r}\, dt\ , \end{aligned} \tag{5.29}$$

for $i=2,3,4,5,6$ and $r=2,3,4$. They are the means, intensities and order-r central moments, respectively. Here T is the length of the time interval, which must be large with respect to the characteristic lifes of the preferent regimes.

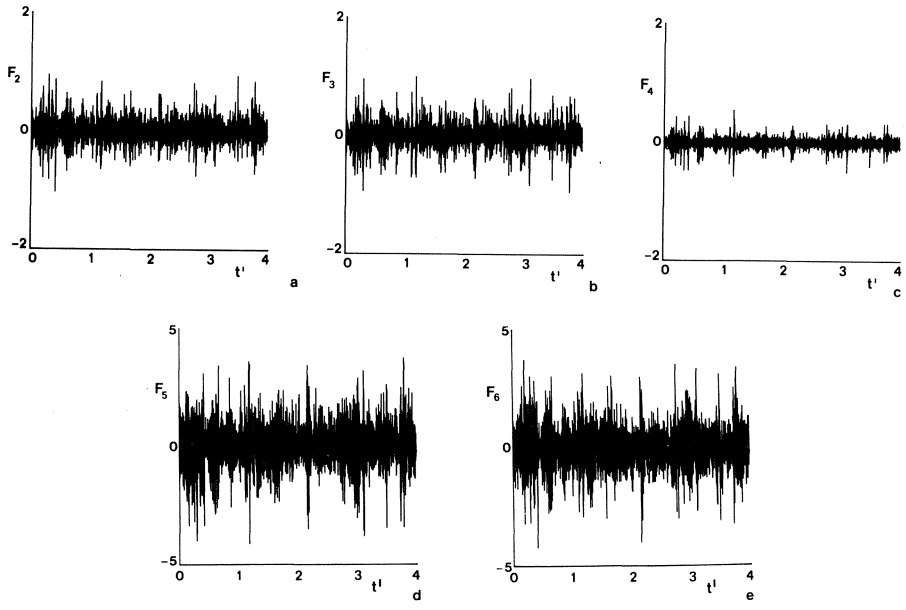

FIGURE 5.13. Time series of the forcing terms, added to the six-component model in order to obtain equivalence with the specified chaotic trajectory of the 10-component model.

From (5.29) we calculated

$$\sigma_i = \sqrt{\mu_{2,i}}\ , \quad S_i = \frac{\mu_{3,i}}{\sigma_i^3}\ , \quad K_i = \frac{\mu_{4,i}}{\sigma_i^4} - 3, \tag{5.30}$$

which are the standard deviations, skewnesses and kurtoses respectively. Here σ_i estimates the spread of the probability density distribution $p(F_i)$ around its average $\overline{F_i}$ and S_i measures the asymmetry of the distribution with respect to $\overline{F_i}$. Finally, K_i measures the long-tail deviation of $p(F_i)$ from a Gaussian distribution

$$G(F_i) = \frac{1}{\sqrt{2\pi}\,\sigma_i} \exp\{-(F_i - \overline{F_i})^2 / 2\sigma_i^2\}, \tag{5.31}$$

which is fully determined by a mean and standard deviation. For details we refer to PRIESTLY (1981). We found that the results, presented in table 5.3, did not depend on the particular time interval chosen hence the time series $F_i(t)$ are stationary. The processes F_5 and F_6 have been itemized in linear orographic contributions (F_{50},F_{60}) and nonlinear wave-wave contributions (F_{5w},F_{6w}). It appears that the intensities of the (1,2)-mode forcing terms are much larger than those which affect the (1,1) mode. In turn these intensities

are large compared to the one of the (0,2) mode. Furthermore, F_5 and F_6 are mainly determined by the contribution due to the wave triad: the contributions caused by flow-topography interactions are negligible. Obviously the presence of topography in the model is only important in order to allow for multiple weather regimes.

	F_2	F_3	F_4	F_5	F_6	F_{50}	F_{5w}	F_{60}	F_{6w}
mean	0.005	0.009	-0.009	0.020	-0.015	0.000	0.019	0.000	-0.015
intensity	0.154	0.158	0.074	0.729	0.698	0.027	0.728	0.027	0.697
st.dev.	0.154	0.157	0.073	0.729	0.698	0.027	0.728	0.027	0.697
skewness	0.191	0.090	-0.471	-0.177	-0.041	-0.043	-0.189	0.085	0.017
kurtosis	2.830	2.985	4.663	2.175	1.919	0.172	2.159	1.67	1.908

TABLE 5.3. Statistical properties of the forcing terms.

Since all forcing terms have nonzero skewnesses and kurtoses we conclude that their probability densities are non-Gaussian. This can also be seen from figure 5.14 where the numerically computed distributions are shown together with their Gaussian approximations obtained from (5.31) and table 5.3. Obviously the forcing terms cannot be parametrized by Gaussian noise processes as was done in chapter IV. We have also calculated statistical properties of the forcing terms in the different weather regimes. It was found that in the high-index regime the intensities of all forcing components are 10 to 15% below their overall averages. This can be explained as follows. For the parameter values used the six-component model has two different attractors: a periodic orbit of high-index type and a stationary point of low-index type, see section III.5. Since the periodic orbit is close to an unstable regular solution of the 10-component model, the intensity of the forcing terms is low in the high-index regime. Conversely, in the low-index regime the difference in dynamics of the two models is large so the forcing intensity is large. The large forcings occurring in the transitional regime are an indication that the six-component model cannot predict transitions between the high- and low-index weather regimes.

Information about the correlation times of the forcing terms is obtained from the autocorrelation functions

$$\rho_i(\tau) = \frac{\overline{[F_i(t)-\bar{F}_i][F_i(t+\tau)-\bar{F}_i]}}{\sigma_i^2} \quad \text{for } i=2,3,4,5,6, \tag{5.32}$$

see PRIESTLY (1981). They measure the statistical dependence between the processes $F_i(t)$ and $F_i(t+\tau)$. Since the time series $F_i(t)$ are stationary, the autocorrelation functions do not depend explicity on time. The results for $\rho_i(\tau)$ are presented in figure 5.15. The functions show oscillatory behaviour with an exponentially decreasing amplitude. Roughly, all curves can be fitted with

$$\rho_i(\tau) \sim e^{-\alpha\tau}\cos(\beta\tau)\ ;\ \alpha\sim 2,\ \beta\sim 7. \tag{5.33}$$

This behaviour is different from that of coloured-noise processes, see (4.9).

Thus, once more we conclude that in this case coloured noise is not an appropriate parametrization of the forcing terms.

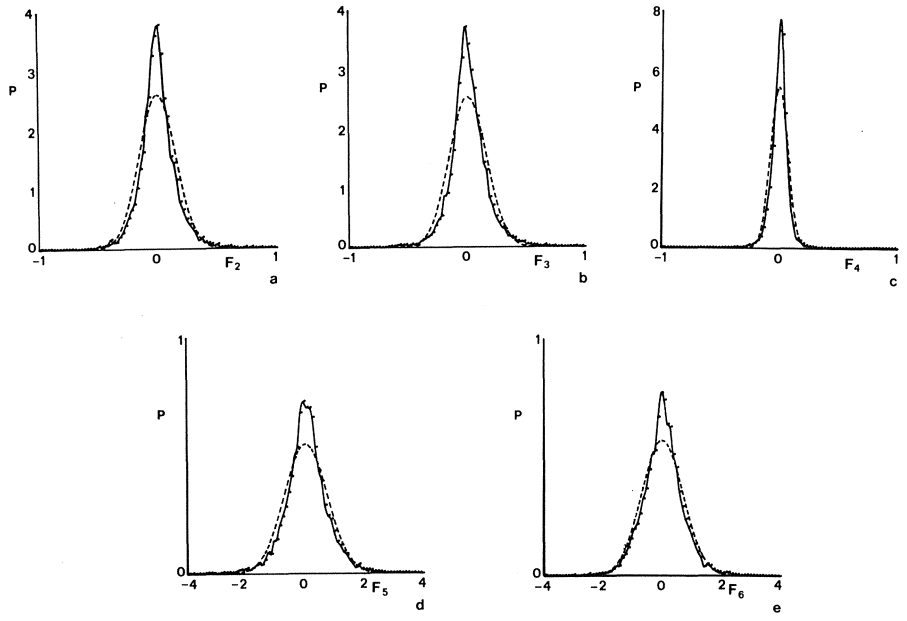

FIGURE 5.14. Numerical approximation of the probability distributions $p(F_i)$ (solid lines) of the forcing terms based on 8000 sampling points and 80 class intervals. The dashed lines represent the Gaussian distributions (5.31) where $\overline{F_i}$ and σ_i are obtained from table 5.3.

Finally, we have investigated the statistical dependence between the processes $F_i(t)$ and $F_j(t+\tau)$ by calculating the normalized correlation matrix $C(\tau)$ with components

$$(\underline{C})_{ij}(\tau) = \frac{\overline{[F_i(t)-\overline{F_i}][F_j(t+\tau)-\overline{F_j}]}}{\sigma_i \sigma_j} \tag{5.34}$$

Note that

$$C_{ij}(\tau) = C_{ji}(-\tau)\,, \quad C_{ii}(\tau) = \rho_i(\tau)\,, \tag{5.35}$$

where $\rho_i(\tau)$ is the autocorrelation function (PRIESTLY, 1981). The results are shown in figure 5.16. Correlations involving the process $F_4(t)$ are omitted since they are very small.

Although statistical significant correlations are observed between $F_2(t)$ and $F_3(t+0.25)$, $F_2(t)$ and $F_6(t+0.10)$ and $F_3(t)$ and $F_5(t+0.10)$, they are rather small and occur for only a small time interval.

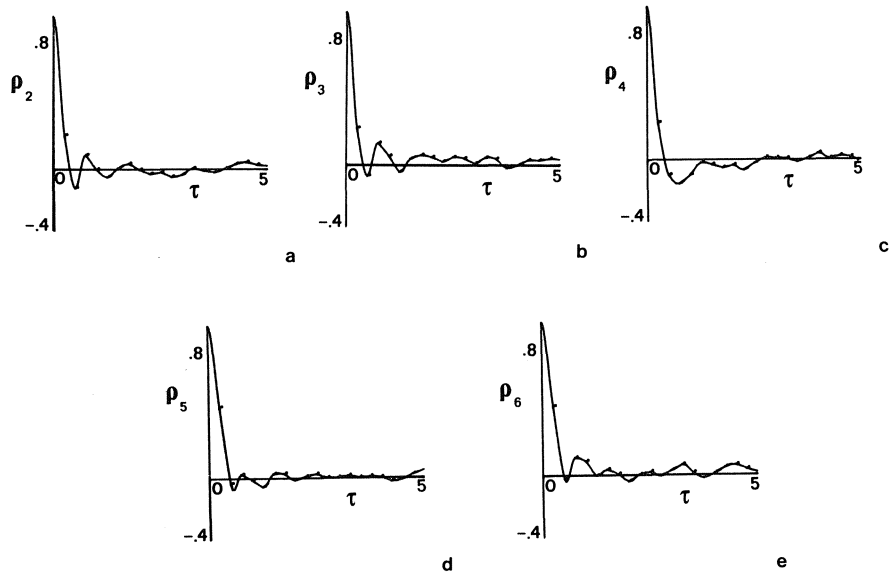

FIGURE 5.15. Autocorrelation functions $\rho_i(\tau)$ of the forcing terms $F_i(t)(i=2,3,4,5,6)$ acting on the six-component model.

V.7. CONCLUDING REMARKS

In this chapter we have studied a 10-component spectral model of the barotropic potential vorticity equation in a beta plane channel. We have shown that, using a rectangular truncation of the spectral expansions in wave-number space, it is the simplest model which represents most qualitative features of the atmospheric circulation. By this we mean that for a range of parameter values solutions are obtained modelling a finitely predictable circulation which alternately visits different weather regimes. In this case three preferent regions in phase space are found characterized by unstable periodic orbits of the model. They correspond to a high-index, transitional and low-index flow regime. This behaviour is due to the presence of a barotropic wave triad. It provides for a direct interaction between two distinct scales of motion: a planetary scale and synoptic scale. An index cycle occurs on a time scale of the order of months whereas on a a shorter time scale (order of days) oscillations are present which characterize the individual preferent regimes.

We have analysed the static and dynamical structure of the strange attractor of the 10-component model. Its embedding dimension, which is 8 in this case, estimates the actual number of degrees of freedom of the flow. In this case we could indeed select an 8-component subsystem of the full model which still represents a chaotic flow with vacillatory behaviour. Therefore, if we do not

adapt the condition of a rectangular truncation in wavenumber space, this 8-component system should be considered as a minimum-order spectral model of the atmospheric circulation.

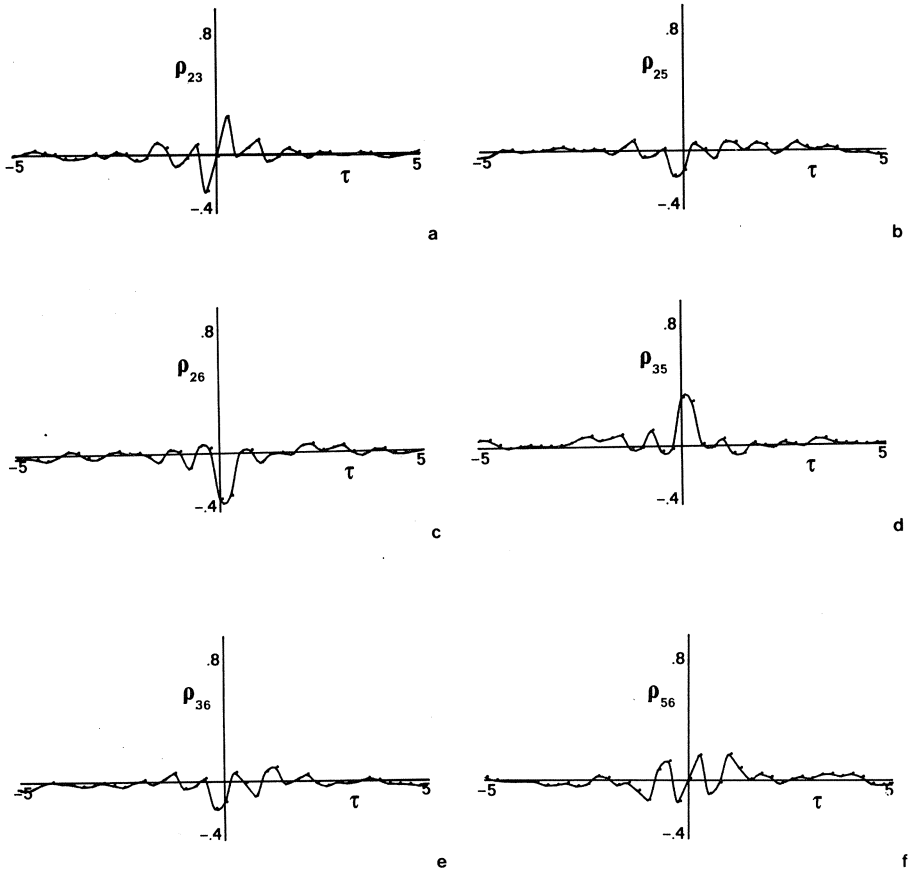

FIGURE 5.16. Correlations $C_{ij}(\tau)$ between the processes $F_i(\tau)$ and $F_j(t+\tau)$ as a function of the time shift τ.

The reciprocal of the sum of all positive Lyapunov exponents, which measure the exponential divergence between nearby orbits in phase space, defines an overall time scale (here of about four days) on which the flow is predictable. In order to to investigate local predictability properties of the flow the linearized error equations along a principal orbit were solved. It was proposed that the local eigenvalues of the matrix derivative of the vectorfield along the orbit estimate the error growth while the corresponding eigenvectors determine the geographical distribution of the errors. This implies that during periods

where all eigenvalues have negative real parts predictability of the flow is large, since small errors converge to the principal orbit. However, this concept is not successful when the flow itself evolves on a time scale which is comparable to the time scale of error growth. Consequently, the method cannot be applied to the 10-component model studied here, but the models of REINHOLD and PIERREHUMBERT (1982) and LEGRAS and GHIL (1985) may be appropriate because they show long periods of quasi-stationary behaviour. In this way the skill of a forecast can be predicted which is an important physical quantity, see the discussion in TENNEKES et al. (1986).

Finally we have investigated the closure problem for forcing terms which account for the effect of the neglected modes and physical processes not incorporated in the model. This was done by by assuming that the 10-component model gives an exact representation of the atmospheric dynamics. A six-component subsystem resolving only the planetary-scale motion, was chosen to be a forecast model. To the latter forcing terms were added such that solutions of both models are equivalent. In this case it appeared that the forcing terms cannot be parametrized by Gaussian coloured-noise processes as was done in chapter IV.

VI. Conclusions

In this final chapter we discuss the possible contribution of our investigations to a better understanding of the dynamics of the atmospheric circulation. To that end we return to chapter I where it was was noticed that the midlatitudinal circulation has two different scales of motion. We can distinguish between planetary-scale motion, characterized by a westerly background flow and ultra-long quasi-stationary planetary waves, and synoptic-scale motion having shorter length and time scales. Furthermore, as discussed in REINHOLD and PIERREHUMBERT (1982) and REINHOLD (1987), the feed-back between these two scales of motion leads to the occurrence of quasi-stable preferent flow configurations, called weather regimes. These results confirm the earlier, more intuitive, ideas of BAUR et al. (1944), HESS and BREZOWSKY (1969) and VAN-DIJK et al. (1974) who used atmospheric data to define large-scale preferent circulation patterns over Europe and the Atlantic. So far the existence of weather regimes has not been convincingly demonstrated by a systematic data analysis, although in some recent studies indications are found that the atmospheric circulation has a bimodal structure (DOLE, 1986; BENZI et al., 1986a,b).

The preceding description indicates that the atmosphere may be seen as a chaotic system that irregularly vacillates between different weather regimes. Thus, for the development of long-range weather forecast models it is important to obtain a better understanding of the vacillation properties of the circulation. In this tract this problem has been studied by constructing simplified models which represent the chaotic properties and vacillatory behaviour of atmospheric flow. Next we have investigated whether they provide clues to analyse more complicated models as well as atmospheric data.

A method to derive such models has been discussed in chapter II. First, by application of scale analysis, the equations of motion describing atmospheric flow are reduced to the quasi-geostrophic barotropic potential vorticity

equation. This implies that effects of nongeostrophic phenomena (for example gravity waves) and baroclinicity (vertical structure of the fluid) are neglected. It is shown that this equation in fact only models synoptic-scale motion. In order to take planetary-scale motions into account as well, a planetary-scale vorticity balance should be included together will additional contributions in the synoptic-scale vorticity balance. However, we have not considered such an extension in this tract.

The solution of the barotropic potential vorticity equation is represented as a series expansion in modes, where each mode is an eigenfunction of the Laplace operator satisfying the boundary conditions. Projecting the equation on a few modes yields a low-order spectral model which is a set of coupled nonlinear ordinary differential equations describing the time evolution of the modal amplitudes. There is no physical motivation to truncate the mode expansions at such low values. Nevertheless, models of extremely low-order already show features like multiple weather regimes and chaotic flow, see the review in DE SWART (1988). These models can be analysed with techniques originating from the theory of dynamical systems.

In this tract we have studied three different spectral models of the barotropic potential vorticity equation for a beta-plane channel geometry. They consist of three, six and ten components, respectively. We have investigated their internal dynamics as well as their response to random forcing terms representing the effect of the neglected modes and physical processes not incorporated in the model. Three different parametrization schemes have been considered: a white-noise forcing, a coloured-noise forcing and a forcing computed from time series of a higher-order spectral model. A sketch of the cases studied in this tract is presented in table 1.1 on page 9.

The three-component model, considered in section II.3, is the simplest nontrivial model of the atmospheric circulation. It describes the interaction of an externally forced zonal flow mode and a single Rossby wave. The properties of its asymptotic states are determined by a physical mechanism called topographic instability. In the absence of mountains one globally attracting steady state of the high-index type is found. If topographic forcing is introduced waves are generated and three steady states may occur for a range of parameter values. Two of these steady states (of high-index and low-index type) are stable and one (of transitional type) is unstable. Since their streamfunction patterns resemble large-scale atmospheric preferent states, CHARNEY and DEVORE (1979) have suggested that the presence of weather regimes is related to stationary points of spectral models.

However, the three-component model is unrealistic in the sense that its asymptotic states are always stationary. In order to obtain frequent transitions between the steady states, we have added in chapter IV stochastic perturbations of Gaussian white- and coloured-noise type to the spectral equations. These choices are motivated by data studies of EGGER and SCHILLING (1983, 1984) where it is shown that this forcing has a coloured-noise character. In our model the noise forces the system to visit alternately the two attraction domains of the stable equilibria. During a transition the system remains for

some time in the neighbourhood of the unstable equilibrium. This suggests that the latter may be important for the atmospheric dynamics. The expected residence times in domains close to the equilibria measure the persistence of the preferent states. They have been calculated by a combination of analytical and numerical methods. It appears that the results strongly depend on the model parameters, on the noise intensity and, to a less extent, on the correlation time of the noise.

The alternation of preferent states has been described as a discrete-state Markov process model. It consist of three states which are related to the equilibria of the unperturbed three-component model. Transition probabilities have been derived from the expected residence times of the stochastically forced dynamical system. The eigenvalues of the master equations of the Markov model yield information about the time scale over which the effect of an initial state is present in the system. Furthermore, we have found that to a good approximation transition probabilities are independent of time. As a consequence it follows that there is no dynamically preferred persistence time of a weather regime. This conclusion is in agreement with the observational results of DOLE and GORDON (1983) and DOLE (1986) and also with the model results of REINHOLD and PIERREHUMBERT (1982) and LEGRAS and GHIL (1985). We have compared our results with those of SPEKAT et al. (1983) who use a Markov model of the atmospheric circulation with transition probabilities derived from data. It follows that the expected residence times in our model are much larger (by a factor of 10) than those observed in the atmosphere.

In order to obtain better qualitative agreement with the atmospheric dynamics we have studied in chapter III the effect of including more modes in the spectral expansions. The result is a six-component model, containing the previous three-component model as a subsystem. It describes the evolution of two zonal flow modes and two Rossby waves. It appears that solutions of the subsystem are also solutions of the full model, but their stability properties may differ because perturbations have more degrees of freedom. The increased number of modes allows for a new type of nonlinear interaction involving one zonal flow mode and two different Rossby waves. This has the effect that either the zonal flow mode or one of the two waves may become barotropically unstable, depending on the width-length ratio of the beta-plane channel. As a consequence the asymptotic states of the six-component model can be more complicated than stationary points: we have also found periodic, quasi-periodic and chaotic solutions. These results were obtained from a numerical bifurcation analysis of the spectral equations, using the software package AUTO of DOEDEL (1986) in combination with time integration routines. Two routes leading to chaos were identified: a cascade of period-doubling bifurcations and the homoclinicity scenario. In the latter case periodic orbits become homoclinic for specific parameter values, i.e., they connect a stationary point with itself. For nearby parameter values chaotic orbits occur, in agreement with the theory of SILNIKOV (1965) and SPARROW (1982). The occurrence of chaotic solutions is of interest since they represent finitely predictable motion.

A quantitative characterization of chaos is provided by its Lyapunov exponents which measure the mean exponential divergence between nearby orbits in phase. They have been computed using a method developed by WOLF et al. (1985). The reciprocal of the sum of all positive Lyapunov exponents defines a time scale on which the flow is predictable on the average. However, we have not analysed the chaotic properties in detail since it appears that the strange attractors have a limited attraction domain in phase space. In this case chaotic orbits remain in the low-index regime forever, while for the same parameter value a stable stationary point or periodic orbit of high-index type exists. Consequently, although the six-component model has interesting properties it cannot show vacillatory behaviour. This is due to the presence of only one barotropic triad in the model which allows for either a single zonal flow mode or a single Rossby wave to become unstable.

In chapter IV a few remarks have been made concerning the effect of stochastic perturbations on the six-component model. It is demonstrated that the method developed to compute expected residence times of the system near equilbria of the unperturbed model, see DE SWART and GRASMAN (1987), is also applicable to spectral models with dimensions larger than 3. However, the use of this method is limited because it can deal with equilibria only, whereas the six-component model has also more complicated attractors. When the model possesses equilibria only, we found that its statistical properties do not differ from those of the randomly perturbed three-component subsystem.

In order to construct a spectral model with internal vacillation behaviour, we have extended in chapter V the six-component model by including two additional Rossby waves in the eigenfunction expansions. The resulting 10-component model contains three different barotropic triads of nonlinear interactions. This appears to be sufficient to turn all regular solutions unstable, provided that both zonal flow modes are externally forced. This implies that in this case the three-component model is not a subsystem of the full model. Furthermore, although the six-component model is a subsystem, its solutions are not solutions of the full model because of the presence of a new type of nonlinear interaction involving three different Rossby waves. This wave triad provides for a direct interaction between two different scales of motion: a planetary scale and a synoptic scale. For a sufficiently large external forcing, trajectories of the 10-component model move on a strange attractor in phase space and show vacillatory behaviour. Again three preferent regimes (of high-index, low-index and transitional type) have been found, which are characterized by unstable periodic orbits of the model instead of by stationary points. Vacillation occurs on a time scale of the order of months whereas on a shorter time scale (order of days) oscillations are present which characterize the different weather regimes. We conclude that the 10-component model is a minimum-order quasi-geostrophic spectral model describing a flow which shows transitions between different weather regimes and which is predictable for a finite time only. However, this result is based on the assumption of a rectangular truncation of the eigenfunction expansions in the wavenumber domain. We have calculated the actual number of degrees

of freedom of the chaotic flow from the fractal dimensions of the strange attractor and found this number to be 8. Indeed, in this case an 8-component subsystem of the 10-component model could be selected which allows for a global strange attractor and vacillatory behaviour. Thus, if we drop the condition about the rectangular truncation (which we have not done), the 8-component model should be considered as a minimum-order atmospheric model.

The regime predictability of the 10-component model has been studied by computing the mean residence times of the system in the different flow regimes. Using these results the alternation between the regimes has been simulated with a 3-state Markov model, similar to the one discussed in chapter IV. From this it follows a time scale on which, starting from a given initial condition, the Markov process model contains more information about the system than the stationary probability distribution. A time scale on which the flow itself is predictable on the average has been calculated from the sum of all positive Lyapunov exponents. Its value of about 4 days agrees with what is observed for the atmospheric circulation. However, as discussed by TENNEKES et al. (1986), of more interest to meteorologists are the local predictability properties of atmospheric flow. This problem has been investigated by solving the linearized error equations along a principal orbit of the 10-component model. It was concluded that the largest real part of all eigenvalues of the matrix derivative of the vectorfield along the orbit determines the error growth rate (which is a measure of predictability), provided that the time scale of error growth is small compared to the time scale on which the flow evolves. In our model this condition is not met, but it is suggested that the models of REINHOLD and PIERREHUMBERT (1982) and LEGRAS and GHIL (1985) may be appropriate. In that case the eigenvectors corresponding to the eigenvalues with largest real part determine the local geographical distribution of error growth.

Finally, a method has been developed to study the closure problem for the forcing terms in a low-order spectral model which represent the effect of the neglected modes. We have defined the 10-component model as an exact representation of the atmospheric dynamics and considered its six-component subsystem as a forecast model. To the latter, forcing terms have been added such that its solutions are identical to solutions of the 'exact' model projected onto the six-dimensional subspace. It has been demonstrated that these forcing terms have a complicated nature and that they cannot be parametrized by the simple stochastic processes used in chapter IV. This result is in agreement with the findings of LINDENBERG and WEST (1984) and KOTTALAM et al. (1987). Furthermore, it is not in contradiction with the results of EGGER and SCHILLING (1983, 1984) since the latter authors also include the effect of neglected physical processes in their definition of effect of the neglected small-scale motions.

Summarizing, we conclude that all barotropic models studied in this tract have three different weather regimes which are of high-index, low-index and transitional type, respectively. However, the regimes have different

characteristics in different models. In case an index cycle is simulated the mean life times of the regimes are a factor 10 larger than those observed in the atmosphere. Moreover, extremely large external forcing values (corresponding to an equator-pole temperature difference of more than 150 degrees) are needed in order to obtain internally generated vacillation behaviour. We expect these imperfections to become smaller if more realistic atmospheric models are used. As a first step we note that in barotropic models effects of topography are over-estimated because they act directly on the entire fluid column. Baroclinic, multi-level models of the quasi-geostrophic potential vorticity equation give better results at this point. Again multiple equilibria are found in low-order systems, but, although the low-index equilibria cannot exist without topography, their energy is extracted from the potential energy of the mean flow and not from a kinetic energy transfer via the mountain torque (CHARNEY and STRAUS, 1980; KÄLLÉN, 1983). The presence of the baroclinic instability mechanism causes equilibria to be less stable than in barotropic models. As argued in DE SWART (1988), the two-level 20-component spectral model of REINHOLD and PIERREHUMBERT (1982) is the simplest model containing all basic physical mechanisms. It allows for the presence of topographic, barotropic and baroclinic instability as well as the occurrence of wave triad interactions. This system also alternately visits three preferent weather regimes and shows a clear distinction between a quasi-stationary planetary scale and a transient synoptic scale. However, again we encounter the problem that an unrealistically large external, thermal forcing ($>100K$ over $5000km$) is required in order to obtain vacillatory behaviour. Moreover, the characteristic life times of the weather regimes are still too large compared to observational results. We argue once more that these imperfections are due to the severe truncation in both the horizontal and vertical direction. A better description of the circulation is expected from multi-level high-resolution models. However, they are difficult to analyse for their structure is extremely complicated. Alternatively, we may study lower-dimensional spectral models which include an appropriate parametrization of the effect of the neglected small-scale motions.

In conclusion, we think it is useful to study both deterministic and stochastically forced spectral models of the atmospheric circulation for various horizontal and vertical truncation numbers. The mathematical analysis of these systems may give insight in the qualitative dynamics of the model, such as the existence of preferent regions in phase space and transitions of the system between these regions. By combining physical motivations and modern mathematical techniques it may be possible to enlarge our knowledge of the dynamics of the atmospheric circulation.

Appendix A

Order estimation of $\partial\theta_\star/\partial z$ in the atmosphere

From (2.22) it follows that

$$\frac{\partial\tilde{\theta}_\star}{\partial\tilde{z}}=\frac{\partial^2\tilde{p}_\star}{\partial\tilde{z}^2}-\tilde{p}_\star\frac{d}{d\tilde{z}}\left(\frac{1}{\theta_s}\frac{d\theta_s}{d\tilde{z}}\right)-\frac{\partial\tilde{p}_\star}{\partial\tilde{z}}\frac{1}{\theta_s}\frac{d\theta_s}{d\tilde{z}}, \tag{A1}$$

with the tildes referring to nondimensional variables. Now

$$\frac{1}{\theta_s}\frac{d\theta_s}{d\tilde{z}}=\frac{H}{g}N^2,\quad \frac{d}{d\tilde{z}}\left(\frac{1}{\theta_s}\frac{d\theta_s}{d\tilde{z}}\right)=\frac{H^2}{g}\frac{d}{dz}(N^2),\quad N^2=\frac{g}{\theta_s}\frac{d\theta_s}{dz}, \tag{A2}$$

where N is the Brunt-Väisälä frequency. In GILL (1982) it is remarked that N^2 varies between $10^{-4}s^{-2}$ in the troposphere up to $4.10^{-4}s^{-2}$ at the lower bound of the stratosphere. Since $H=10^4m$ and $g=10ms^{-2}$, it follows

$$\frac{1}{\theta_s}\frac{d\theta_s}{d\tilde{z}}=\mathcal{O}(\epsilon),\quad \frac{d}{d\tilde{z}}\left(\frac{1}{\theta_s}\frac{d\theta_s}{d\tilde{z}}\right)=\mathcal{O}(\epsilon). \tag{A3}$$

Furthermore,

$$\frac{\partial^2\tilde{p}_\star}{\partial\tilde{z}^2}=\frac{H^2}{Fp_s}\frac{\partial^2 p_\star}{\partial z^2} \tag{A4}$$

and from table 2 of BRANSTATOR (1987) it follows $\partial^2 p_\star/\partial z^2 < 10$ mbar $/(10\,km)^2$ hence with $F=0.1$ and $p_s=10^5Nm^{-2}$ the result is

$$\frac{\partial^2\tilde{p}_\star}{\partial\tilde{z}^2}=\mathcal{O}(\epsilon). \tag{A5}$$

Substituting (A3) and (A5) in (A1) we find

$$\frac{\partial\tilde{\theta}_\star}{\partial\tilde{z}}=\mathcal{O}(\epsilon). \tag{A6}$$

Hence this contribution may be neglected in the derivation of (2.27) from (2.23e).

Appendix B

Interaction coefficients

for the eigenfunctions (2.49a,b)

Substitution of (2.49a,b) in (2.41) gives

$$c_{jlm} = 0\,, \tag{B1}$$

except for

A) $j = (0,j_2)$, $l = (l_1,l_2)$, $m = (-l_1,m_2)$; $j_2+l_2+m_2$ odd, then

$$c_{jlm} = \frac{i\sqrt{2}\,l_1}{\pi b}\left\{(l_2+m_2)\left[\frac{1}{j_2+l_2+m_2} - \frac{1}{j_2-l_2-m_2}\right]\right. \tag{B2}$$
$$\left. - (l_2-m_2)\left[\frac{1}{j_2+l_2-m_2} - \frac{1}{j_2-l_2+m_2}\right]\right\},$$

B) $j = (j_1,j_2)$, $l = (l_1,l_2)$, $m = (m_1,m_2)$, $j_1+l_1+m_1 = 0$, $j_2 \pm l_2 \pm m_2 = 0$, then

$$c_{jlm} = \begin{cases} \dfrac{i}{b\sqrt{2}}(l_1m_2 - l_2m_1) \;;\; j_2 = l_2+m_2\,, & \text{(B3a)} \\ \dfrac{i}{b\sqrt{2}}(l_1m_2 + l_2m_1) \;;\; j_2 = l_2-m_2\,, & \text{(B3b)} \\ \dfrac{-i}{b\sqrt{2}}(l_1m_2 + l_2m_1) \;;\; j_2 = l_2+m_2\,. & \text{(B3c)} \end{cases}$$

Furthermore

$$b_{jl} = 0 \tag{B4}$$

except for

$$j = (j_1,j_2),\;\; l = (l_1,l_2) \text{ with } j_1+l_1 = 0,\; j_2 = l_2,$$

then

$$b_{jl} = i\beta b^2 l_1 \tag{B5}$$

Also coefficients which follow from (B2), (B3) and (B5) by permutations of indices j,l and are nonzero, see (2.43).

Appendix C

Equations of the 10-component model

In chapter II the following ten-coefficient model of the quasi-geostrophic barotropic potential vorticity equation (2.34) is derived:

$$
\begin{array}{llllll}
\dot{x}_1 = & & \gamma^*_{11}x_3 & -C(x_1-x^*_1) & , & \\
\dot{x}_2 = & -(\alpha_{11}x_1-\beta_{11})x_3 & & -Cx_2 & -\delta_{11}x_4x_6 & -\rho_{11}(x_5x_8-x_6x_7)\,, \\
\dot{x}_3 = & (\alpha_{11}x_1-\beta_{11})x_2 & -\gamma_{11}x_1 & -Cx_3 & +\delta_{11}x_4x_5 & +\rho_{11}(x_5x_7+x_6x_8)\,, \\
\dot{x}_4 = & & \gamma^*_{12}x_6 & -C(x_4-x^*_4) & +\epsilon_1(x_2x_6-x_3x_5) & +\epsilon_2(x_7x_{10}-x_8x_9)\,, \\
\dot{x}_5 = & -(\alpha_{12}x_1-\beta_{12})x_6 & & -Cx_5 & -\delta_{12}x_3x_4 & +\rho_{12}(x_2x_8-x_3x_7) \quad +\gamma'_{12}x_8\,, \\
\dot{x}_6 = & (\alpha_{12}x_1-\beta_{12})x_5 & -\gamma_{12}x_4 & -Cx_6 & +\delta_{12}x_2x_4 & -\rho_{12}(x_2x_7+x_3x_8) \quad -\gamma'_{12}x_7\,, \\
\dot{x}_7 = & -(\alpha_{21}x_1-\beta_{21})x_8 & & -Cx_7 & -\delta_{21}x_4x_{10} & -\rho_{21}(x_2x_6+x_3x_5) \quad +\gamma'_{21}x_6\,, \\
\dot{x}_8 = & (\alpha_{21}x_1-\beta_{21})x_7 & & -Cx_8 & +\delta_{21}x_4x_9\,, & +\rho_{21}(x_2x_5-x_3x_6) \quad -\gamma'_{21}x_5\,, \\
\dot{x}_9 = & -(\alpha_{22}x_1-\beta_{22})x_{10} & & -Cx_9 & -\delta_{22}x_4x_8\,, & \\
\dot{x}_{10} = & (\alpha_{22}x_1-\beta_{22})x_9 & & -Cx_{10} & +\delta_{22}x_4x_7\,, &
\end{array}
$$

	advection	topography	forcing/dissipation	advection	wave triad	topography

where

$$
\alpha_{nm} = \frac{8\sqrt{2}n}{\pi}\frac{m^2}{4m^2-1}\frac{n^2b^2+m^2-1}{n^2b^2+m^2}\,,\quad \beta_{nm} = \frac{\beta nb^2}{n^2b^2+m^2}\,,
$$

$$
\delta_{nm} = \frac{64\sqrt{2}n}{15\,\pi}\frac{n^2b^2-(m^2-1)}{n^2b^2+m^2}\,,\quad \gamma^*_{nm} = \frac{4m}{4m^2-1}\frac{\sqrt{2}nb\gamma}{\pi}\,,
$$

$$
\epsilon_n = \frac{16\sqrt{2}n}{5\pi}\,,\quad \gamma_{nm} = \frac{4m^3}{4m^2-1}\frac{\sqrt{2}nb\gamma}{\pi(n^2b^2+m^2)}\,,
$$

$$
\rho_{nm} = \frac{9}{2}\frac{(n-2)^2b^2-(m-2)^2}{n^2b^2+m^2}\,,\quad \gamma'_{nm} = \frac{3b\gamma}{4(n^2b^2+m^2)}\,.
$$

It contains a six-component subsystem, denoted between the dashed lines, and a three-component subsystem denoted between the dotted lines. The relation between state variables and modal amplitudes of the streamfunction is given in (2.51). The α_{nm}-terms describe interactions between the (0,1) and (n,m) modes, the δ_{nm}- and ϵ_n-terms represent interactions between the (0,2), $(n, 1)$ and $(n, 2)$ modes and the terms involving ρ_{nm} are interactions between the (1,1), (1,2) and (2,1) modes. Furthermore the β_{nm}-contributions represent planetary vorticity advection and the $\gamma^*_{nm}, \gamma_{nm}$ and γ'_{nm}-terms the various couplings between flow and topography.

Appendix D

Bifurcation analysis of spectral models

Consider a spectral model which is a dynamical system of the type (1.1). We shall briefly discuss that the existence of strange attractors can be investigated from a systematic bifurcation analysis of its stationary points and periodic orbits. For more details we refer to GUCKENHEIMER and HOLMES (1983) and THOMPSON and STEWART (1986). The smooth vectorfield $f_\mu(x)$ generates a phase flow $\phi^t:\mathbb{R}\to\mathbb{R}^N$. Then $x(t)=\phi^t x_0$ defines an orbit or a trajectory of (1.1) in phase space having the initial condition $x(0)=x_0$. It is well-known that these solutions exist and are unique. The spectral models in this tract obey

$$\nabla\cdot f_\mu(x) = -a \; ; \; a>0, \tag{D1}$$

indicating that small volume elements in phase space always shrink. Moreover it can be shown that solutions are bounded.

Stationary points $\hat{x}$ satisfy

$$f_\mu(\hat{x}) = 0 \tag{D2}$$

and the system is said to be in equilibrium or in a steady state. The dynamics of small perturbations x' on this state is described by

$$\dot{x}' = \underline{D}\cdot x' + o(|x'|), \; (\underline{D})_{ij} = \partial f_{\mu,i}/\partial x_j \,|_{x=\hat{x}} . \tag{D3}$$

As long as the eigenvalues $\{\lambda_i\}_{i=1}^N$ of matrix D have no zero real parts they govern the stability of $\hat{x}$. If all real parts are negative $\hat{x}$ is stable, whereas if at least one eigenvalue has a positive real part the stationary point is unstable. Since the system obeys (D1) the sum of all eigenvalues equals $-a$, which is negative. Consequently unstable equilibria are of the saddle-point type: they have a stable manifold $W^s(\hat{x})$ as well as an unstable manifold $W^u(\hat{x})$, defined as

$$\begin{aligned} W^s(\hat{x}) &= \{x\in\mathbb{R}^N | \phi^t x\to\hat{x} \text{ for } t\to\infty\}, \\ W^u(\hat{x}) &= \{x\in\mathbb{R}^N | \phi^t x\to\hat{x} \text{ for } t\to-\infty\}. \end{aligned} \tag{D4}$$

Near the stationary point $W^s(\hat{x})(W^u(\hat{x}))$ is spanned by the eigenvectors corresponding to the eigenvalues of matrix D with negative (positive) real part. It may occur that a stable manifold of a stationary point $\hat{x}^{(i)}$ is contained in an unstable manifold of a stationary point $\hat{x}^{(j)}$ or vice versa. If $i=j (i\neq j)$ this gives rise to homoclinic (heteroclinic) connections, see figure D1.

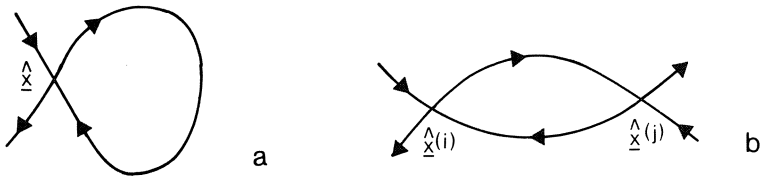

FIGURE D1. Visualization of homoclinic (a) and heteroclinic connections (b).

A procedure to compute branches of stationary points as a function of one control parameter μ_1 numerically is described in KELLER (1977). The method is implemented in the package AUTO of DOEDEL (1986) which is used in this tract. Generally, in this way we will encounter critical parameter values where one or more real parts of the eigenvalues of matrix D become zero. Near these bifurcation points we can no longer neglect the $o(|x'|)$ contributions in (D3). Important information about the behaviour of the dynamical system near such a point is provided by two theorems. The first states that the local behaviour is governed by the projection of the system onto the center manifold, which is locally spanned by the eigenvectors corresponding to the eigenvalues of D with zero real part. The second theorem states that the projected system can be transformed into a limited number of standard (normal) forms. In case of one control parameter μ_1 (codimension-1 bifurcations) there are four normal forms for the local bifurcations of stationary points. They read

$$\dot{x}_1 = \mu_1 + \alpha x_1^2 \quad : \text{saddle-node bifurcation,} \tag{D5a}$$

$$\dot{x}_1 = \mu_1 x + \alpha x_1^2 \quad : \text{transcritical bifurcation,} \tag{D5b}$$

$$\dot{x}_1 = \mu_1 x + \alpha x_1^3 \quad : \text{pitchfork bifurcation,} \tag{D5c}$$

$$\left.\begin{aligned} \dot{r} &= \mu r + \alpha r^3 \quad , \quad r^2 = x_1^2 + x_2^2 \\ \dot{\theta} &= 1 \qquad\quad , \quad \tan\theta = x_2/x_1 \end{aligned}\right] \quad : \text{Hopf bifurcation} \tag{D5d}$$

Here α can have the values -1 or 1, which refer to a supercritical and subcritical bifurcation, respectively. The behaviour of the solutions of (D5) for $\alpha = -1$ is shown in figure D2. The first three types correspond to a real eigenvalue passing through zero at $\mu_1 = 0$. In case of the saddle-node bifurcation $(\hat{x}_1, \mu_1) = (0,0)$ is not a singular point of the vectorfield since its derivative with respect to μ_1 is nonzero. Therefore it is called a turning point whereas in all other cases $(\hat{x}, \mu_1) = (0,0)$ is a bifurcation point. The pitchfork bifurcation requires invariance under the transformation $x_1 \to -x_1$. Finally the Hopf bifurcation generates a periodic orbit which at $\mu_1 = 0$ has amplitude zero and period $T = 2\pi/\lambda^{(i)}$, where $\pm\lambda^{(i)}$ are the imaginary parts of the eigenvalues of D with real parts zero.

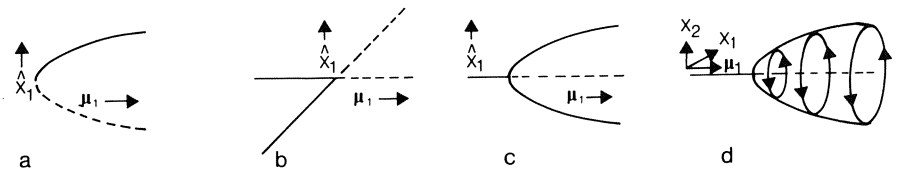

FIGURE D2. Bifurcation diagram of the supercritical saddle-node bifurcation (a), transcritical bifurcation (b), pitchfork bifurcation (c) and Hopf bifurcation (d). A solid line denotes that the solution is stable while a dashed line refers to an unstable solution.

However, more complicated situations may occur, where more than one control parameter is needed to describe the bifurcation adequately. A frequently occurring example is the case of a saddle-node bifurcation where the quadratic terms become nonzero ($\alpha=0$ in (D5a)). Then the generalized normal form

$$\dot{x}_1 = \mu_1 + \mu_2 x_1 + \alpha x_1^3 \tag{D6}$$

should be considered. This unfolding of the saddle-node bifurcation describes a codimension-2 bifurcation since we now have two control parameters instead of one. The set of bifurcation values (μ_1,μ_2) consists of two branches describing saddle-node bifurcations which coalesce at the cusp point $(\mu_1,\mu_2)=(0,0)$. Other complicated situations occur when matrix D in (D3) is more degenerated, for example that one real eigenvalue as well as the real parts of the complex conjugated eigenvalues become zero for a specific parameter value. As shown by LANGFORD (1981) the bifurcation structure may then involve homoclinic and heteroclinic connections, which are associated with a direct transition from regular to chaotic solutions.

We next consider the stability of T-periodic orbits $\gamma(t)$ of (1.1), thus $\gamma(t+T)=\gamma(t)$. The dynamics of small perturbations on this orbit is given by

$$\dot{x} = \underline{A}(t)\cdot x' + o(|x'|), \quad [\underline{A}(t)]_{ij} = \partial f_{\mu,i}/\partial x_j|_{\gamma(t)} \tag{D7}$$

Since $A(t)$ is a periodic matrix the linear part of (D7) is solved by defining $\Phi(t)$ as a fundamental matrix, having the elements

$$[\underline{\Phi}(t)]_{ij} = \partial x_i/\partial x_j|_{\gamma(t)}. \tag{D8}$$

The columns of this matrix contain N independent solutions of the linearized system in (D7). The eigenvalues $\{\rho_i\}_{i=1}^N$ of $\Phi(T)$ are called Floquet multipliers. One of them (say ρ_1) is always equal to one and is associated with perturbations along the periodic orbit. As long as all other multipliers have absolute values not equal to one they govern the stability of $\gamma(t)$. If all absolute values are smaller than 1 the periodic orbit is stable, wheres if at least one of the multipliers has absolute value larger than one $\gamma(t)$ is unstable. A numerical procedure to compute periodic orbits as a function of a control parameter

is discussed in SPARROW (1982). Besides we have used the continuation routines of the package AUTO which are based on a different approach, see DOEDEL (1986) and DOEDEL and KERNEVEZ (1987).

Bifurcations of periodic orbits can be analysed in a similar way as discussed for stationary points. In case of one control parameter there now appear to be five normal forms. Three of them correspond to a real Floquet multiplier passing through 1 and are again called a saddle-node, transcritical and pitchfork bifurcation. Their bifurcation diagrams are similar to those of figure D2a,b,c, except that $\hat{x}_1$ should be replaced by the period T of the orbit. If a real Floquet multiplier passes through -1 a period doubling bifurcation occurs. In the supercritical case, see figure D3a, we have for $\mu_1 < 0$ a stable T-periodic orbit. It becomes unstable at $\mu_1 = 0$, there by generating a stable $2T$-periodic orbit. The final possibility is that the absolute values of two complex conjugated multipliers become 1 at $\mu_1 = 0$, called a torus bifurcation. This situation corresponds to a transition from stable periodic to stable quasi-periodic motion, where the latter is characterized by two frequencies f_1 and f_2 with f_1/f_2 irrational.

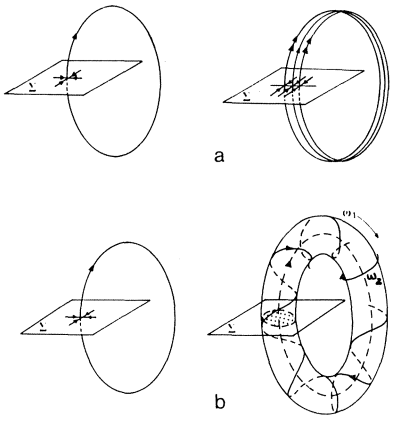

FIGURE D3. Phase flow behaviour for $\mu_1 < 0$ (left) and $\mu_1 > 0$ (right) in case of the supercritical period-doubling bifurcation (a) and torus bifurcation (b). Here Σ is a plane chosen such that it is intersected by the orbits.

There are several bifurcation scenarios which lead to the generation of strange attractors with associated chaotic motion. A frequently occurring example is the period-doubling route, where in a finite interval of the control parameter domain an infinitely long sequence of period-doubling bifurcations occurs, which beyond the accumulation point μ_1^c result in chaotic motion. Another way to obtain chaos is that a periodic orbit becomes homoclinic such that it connects a saddle point with it self. SILNIKOV (1965) first showed that for parameter values close to the homoclinic point chaotic orbits exist. This

scenario is discussed in more detail in chapter III of this tract. A third scenario is the Ruelle-Takens-Newhouse route in which chaos is obtained after one Hopf bifurcation and two torus bifurcations. This scenario is described in chapter V. Thus it appears that considering bifurcation properties of stationary points and periodic orbits is a way to investigate the generation of strange attractors.

Appendix E

Stability of zonal flow profiles

In HAARSMA and OPSTEEGH (1987) a method is developed to study the stability of zonal flow profiles. In this appendix the theory is extended to forced and dissipative systems, as well as to more complicated flow profiles. It can then be applied to the barotropic spectral models of appendix C.

Consider the barotropic potential vorticity equation (2.34) for $\gamma=0$ and $\psi^*=\psi^*(y)$. Then $\hat{\psi}=\psi^*$ is a stationary solution of the equation. Its stability is investigated by considering the dynamics of small perturbations ψ' on $\hat{\psi}$. We obtain

$$\begin{aligned} &(\frac{\partial}{\partial t}+u^*\frac{\partial}{\partial x})\nabla^2\psi' + (\beta-\frac{d^2u^*}{dy^2})\frac{\partial\psi'}{\partial x} + C\nabla^2\psi' = 0, \\ &u^*(y) = -\frac{d\psi^*}{dy} . \end{aligned} \tag{E1}$$

In the β-plane channel with the boundary conditions (2.48) each solution of the barotropic potential vorticity equation can be expanded in eigenfunctions defined in (2.49). In this case, because of (E1), we have

$$u^* = \sqrt{2}\sum_{l=1}^{\infty} u_l^* \sin(\frac{ly}{b}) ; \quad u_l^* = \frac{l\psi_l}{b} , \tag{E2a}$$

$$\psi' = \sqrt{2}e^{-i\sigma t}\left\{\sum_{m=1}^{\infty}\left[\psi_m' \cos(\frac{my}{b}) + \sum_{n=1}^{\infty}[\psi_{nm}'e^{inx} + (\psi_{nm}')^{cc}e^{-inx}]\sin(\frac{my}{b})\right]\right\}, \tag{E2b}$$

where u_l^* and ψ_l' are real coefficients, while ψ_{nm}' are complex amplitudes. Furthermore, *cc* denotes a complex conjugation. We ask for conditions resulting in growing perturbations, i.e.

$$\mathrm{Im}(\sigma)>0. \tag{E3}$$

Substituting (E2a,b) in (E1) and projecting on the spectral components, we obtain

$$\{\psi_m' = 0\}_{m=1}^{\infty} , \tag{E4a}$$

$$\{(\sigma+iC)(n^2+\frac{m^2}{b^2})n\beta\}\psi_{nm}'$$

$$+\sum_{q=1}^{\infty}\sum_{l=1}^{\infty}nu_l^*(n^2+\frac{q^2-l^2}{b^2})c_{mlq}\psi_{nq}'=0;\quad n,m=1,2,..., \tag{E4b}$$

with

$$c_{mlq}=\begin{cases}\frac{2q\sqrt{2}}{\pi}\left\{\frac{1}{(m-l)^2-q^2}-\frac{1}{(m+l)^2-q^2}\right\}, & \\ & \text{if } m+l+q \text{ odd},\\ 0 & \text{if } m+l+q \text{ even}.\end{cases} \tag{E5}$$

We now apply this method to the six-component model discussed in chapter III. Here m,l and q can take on the values 1 and 2, while $n=1$. Eqs. (E4b) reduce to

$$[(\sigma+iC)\kappa_1^2+\beta-\alpha_1u_1^*]\psi_{11}'-\tfrac{1}{2}\tilde{u}_2\psi_{12}'=0, \tag{E6a}$$

$$-\tfrac{1}{2}\tilde{u}_2(1-\kappa_2^2+\kappa_1^2)\psi_{11}'+[(\sigma+iC)\kappa_2^2+\beta-\alpha_2u_1^*]\psi_{12}'=0, \tag{E6b}$$

where

$$\begin{aligned}&\kappa_1^2=1+\frac{1}{b^2}\quad,\ \kappa_2^2=1+\frac{4}{b^2},\\ &\alpha_1=\frac{32\sqrt{2}}{15\pi}(1+\frac{3}{b^2})\ ,\ \alpha_2=\frac{8\sqrt{2}}{3\pi},\ \tilde{u}_2=64\frac{\sqrt{2}}{15\pi}u_2^*.\end{aligned} \tag{E7}$$

For nontrivial solutions of (E6a,b) the determinant of the coefficient matrix must be zero. This results in the quadratic equation

$$a_2\mu^2+a_1\mu+a_0=0 \tag{E8}$$

where

$$\begin{aligned}&\mu=\sigma+iC\ ,\ a_1=(\beta-\alpha_1u_1^*)\kappa_1^2+(\beta-\alpha_2u_1^*)\kappa_2^2,\\ &a_2=\kappa_1^2\kappa_2^2\ ,\ a_0=(\beta-\alpha_1u_1^*)(\beta-\alpha_2u_1^*)-\tfrac{1}{4}\tilde{u}_2^2(1-\kappa_2^2+\kappa_1^2).\end{aligned} \tag{E9}$$

From (E3) and the solutions of (E8) it then follows that the zonal flow profile is unstable if

$$a_1^2-4a_0a_2\leqslant-(2a_2C)^2\ . \tag{E10}$$

Solving for $\tilde{u}_2$ gives

$$\tilde{u}_2^2>\frac{(2\kappa_1^2\kappa_2^2C)^2+\{\beta(\kappa_2^2-\kappa_1^2)-(\alpha_2\kappa_2^2-\alpha_1\kappa_1^2)u_1^*\}^2}{(\kappa_2^2-\kappa_1^2-1)\kappa_1^2\kappa_2^2}=(u_{2,c}^*)^2. \tag{E11}$$

As a numerical example we have taken $b=1.6, C=0.1, \beta=1.25$, $u_1^*\equiv x_1^*=4$ and we ask for the critical amplitude

$$x^*_{4,c} = \frac{1}{2} u^*_2 = \frac{15\pi}{128\sqrt{2}} \tilde{u}_2, \tag{E12}$$

see (E2a) and (E7). Substituting the values in (E11) and developing (E12), we obtain

$$|x^*_4| > x^*_{4,c} = 0.3471. \tag{E13}$$

This agrees with the results of a numerical bifurcation analysis of the spectral model for the same parameter values.

For nonzero γ we still expect the theory presented here to have some validity for the high-index equilibrium. Although the flow is no longer purely zonal, the wave amplitudes are small compared to the zonal flow components. Because the waves have extracted energy from the zonal flow, the effective u^*_1 in (E11) will be smaller. Since

$$\alpha_2 \kappa_2^2 - \alpha_1 \kappa_1^2 = \frac{8\sqrt{2}}{15\pi} \frac{(b^2-2)(b^2+6)}{b^4} \tag{E14}$$

is positives for $b = 1.6$ we expect the effective (0,2) velocity component to be somewhat larger than in case $\gamma = 0$. This is confirmed by numerical experiments, which show for $\gamma = 1$ a (0,2) critical amplitude $|\hat{x}_4| = 0.393$ with a corresponding critical forcing $|x^*_{4,c}| = 0.402$.

Appendix F

Numerical integration of stochastic differential equations

Consider the finite difference scheme of (4.6), which reads

$$x(t+\Delta t) = x(t) + f_\mu(x(t))\Delta t + \epsilon\underline{\sigma}(x(t))\cdot\Delta W(t). \tag{F1}$$

For numerical simulations we make the substitution

$$\Delta W(t) \equiv W(t+\Delta t) - W(t) = B(\Delta t)G. \tag{F2}$$

Here the components of G are mutually independent Gaussian random generators with zero mean and unit standard deviation, a choice based on the properties of the Wiener process. Furthermore $B(\Delta t)$ is a function of the time step Δt which has to be chosen in such way that the parametrization (F2) does not affect the variances of the increments $<\Delta x(t)\Delta x(t)>$ in (F1) i.e.

$$<\Delta W(t)\Delta W(t)> = B^2(\Delta t)<GG> \tag{F3}$$

must hold. Using the property

$$<W(t)W(t+\tau)> = \min(t,t+\tau)\underline{I}\,, \tag{F4}$$

where I is a unity matrix, we find that the left-hand side of expression (F3) equals $\Delta t I$. For the chosen random generators $<GG>=I$, and thus from (F3)

$$B(\Delta t) = \sqrt{\Delta t}. \tag{F5}$$

Hence the numerical scheme for equation (F1) reads

$$x(t+\Delta t) = x(t) + f_\mu(x(t))\Delta t + \epsilon\underline{\sigma}(x(t))\cdot G\sqrt{\Delta t}. \tag{F6}$$

Finally we remark that there are two conditions on the time step. First,

$$\Delta t \ll 1, \tag{F7}$$

in order to avoid instabilities due to the deterministic integration. Secondly, in the limit $\epsilon\to 0$ we except the variance of the difference between the stochastic- and deterministic trajectories to be zero. Therefore we must also require

$$\Delta t = o(\epsilon);\ \epsilon\to 0. \tag{F8}$$

References

BALGOVIND, R., DALCHER, A., GHIL, M. and KALNAY, E. 1983. A stochastic-dynamic model for the spatial structure of forecast error statistics. *Mon. Wea. Rev.* **111,** 701-722.

BARNETT, T.P. and ROADS, J.O. 1986. Stochastic forcing and prediction of low-frequency planetary-scale flow. *J. Atmos. Sci.* **43,** 940-947.

BAUR, F., HESS, P. and NAGEL, H. 1944. *Kalender der Grosswetterlagen Europas 1881-1939.* Bad Homburg v. d. H..

BENZI, R., HANSEN, A.R. and SUTERA, A. 1984. On stochastic perturbation of simple blocking models. *Q. J. R. Meteorol. Soc.* **110,** 393-409.

BENZI, R., SALTZMAN, B. and WIIN-NIELSEN, A.C. 1986a. *Anomalous atmospheric flows and blocking.* Adv. in Geoph. 29, Academic Press, Orlando, 459 pp.

BENZI, R., MALGUZZI, P., SPERANZA, A. and SUTERA, A. 1986b. The statistical properties of the general atmospheric circulation: observational evidence on a minimal theory of bimodality. *Q. J. R. Meteorol. Soc.* **112,** 661-674.

BLACKMON, M., MADDEN, R.A., WALLACE, J.M. and GUTZLER, D.S. 1979. Geographical variations in the vertical structure of geopotential height fluctuations. *J. Atmos. Sci.* **36,** 2450-2466.

BRANSTATOR, G. 1987. A striking example of the atmosphere's leading traveling pattern. *J. Atmos. Sci.* **44,** 2310-2323.

BRUNS, T. 1985. Contribution of linear and nonlinear processes to the long-term variability of large-scale atmospheric flow. *J. Atmos. Sci.* **42,** 2506-2522.

CHARNEY, J.G. AND DEVORE, J.G. 1979. Multiple flow equilibria in the atmosphere and blocking. *J. Atmos. Sci.* **36,** 1205-1216.

CHARNEY, J.G. and STRAUS, D.M. 1980. Form-drag instability, multiple equilibria and propagating planetary waves in baroclinic, orographically forced, planetary wave systems. *J. Atmos. Sci.* **37,** 1157-1176.

CONSTANTIN, P., FOIAS, C., MANLEY, O.P. and TEMAM, R. 1985. Determining modes and fractal dimensions of turbulent flows. *J. Fluid Mech.* **150,** 427-440.

DE SWART, H.E. 1988. Low-order spectral models of the atmospheric circulation: a survey. *Acta Appl. Math.* **11,** 49-96.

DE SWART, H.E. and GRASMAN, J. 1984. Sources of stochastic behaviour in dynamical systems. In: Proc. Workshop *'The dynamics of long waves in the atmosphere'*, Kristineberg, Sweden, 147-152.

DE SWART, H.E. and GRASMAN, J. 1987. Effect of stochastic perturbations on a low-order spectral model of the atmospheric circulation. *Tellus* **39A,** 10-24.

DOEDEL, E.J. 1986. *AUTO 86 user manual, software for continuation and bifurcation problems in ordinary differential equations.* Concordia University, Montreal.

DOEDEL, E.J. and KERNEVEZ, J.P. 1987. Software for continuation problems

in ordinary differential equations with applications. Subm. to *SIAM J. Numer. Anal.*.

DOLE, R.M. 1986. Persistent anomalies of the extratropical Northern Hemisphere wintertime circulation: structure. *Mon. Wea. Rev.* **114,** 178-207.

DOLE, R.M. and GORDON, N.D. 1983. Persistent anomalies of the extratropical Northern Hemisphere wintertime circulation: geographical distribution and regional persistence characteristics. *Mon. Wea. Rev.* **111,** 1567-1586.

DUTTON, J. 1974. The nonlinear quasi-geostrophic equation: existence and uniqueness of solutions on a bounded domain. *J. Atmos. Sci.* **31,** 422-433.

ECKHAUS, W. 1979. *Asymptotic analysis of singular perturbations.* North-Holland Pu. Co., Amsterdam, 287 pp.

EGGER, J. 1981. Stochastically driven large-scale circulations with multiple equilibria. *J. Atmos. Sci.* **38,** 2608-2618.

EGGER, J. and SCHILLING, H.D. 1983. On the theory of the long-term variability of the atmosphere. *J. Atmos. Sci.* **40,** 1073-1085.

EGGER, J. and SCHILLING, H.D. 1984. Stochastic forcing of planetary scale flow. *J. Atmos. Sci.* **41,** 779-788.

FARMER, D.J., OTT, E. and YORKE, J.A. 1983. The dimension of chaotic attractors. *Physica* **7D,** 153-180.

FJØRTOFT, R. 1953. On the changes in the spectral distribution of kinetic energy for two-dimensional nondivergent flow. *Tellus* **5,** 225-230.

FRANCESHINI, V., TEBALDI, C. and ZIRONI, F. 1984. Fixed point limit behaviour of N-mode truncated Navier-Stokes equations as N increases. *J. Stat. Phys.* **35,** 387-397.

FREDERIKSEN, J.S. 1983. A unified three-dimensional instability theory of the onset of blocking and cyclogenesis II: teleconnection patterns. *J. Atmos. Sci.* **40,** 2593-2609.

GARDINER, C.W. 1983. *Handbook of stochastic methods for physics, chemistry and the natural sciences.* Springer Verlag, Berlin, 442 pp.

GASPARD, P., KAPRAL, R. AND NICOLIS, G. 1984. Bifurcation phenomena near homoclinic systems: a two-parameter analysis. *J. Stat. Phys.* **35,** 697-727.

GILL, A.E. 1982. *Atmosphere-ocean dynamics. Academic Press,* New York, 662 pp.

GLENDINNING, D. and SPARROW, C. 1984. Local and global behaviour near homoclinic orbits. *J. Stat. Phys.* **35,** 647-695.

GOLDSTEIN, H. 1980. *Classical mechanics,* 2nd edition. Addison-Wesley Pub. Co. Inc., Reading, 672 pp.

GOTTLIEB, D. and ORSZAG, S.A. 1977. *Numerical analysis of spectral methods.* Regional Conference Series in Applied Mathematics 26, SIAM, Philadelphia, 172 pp.

GRASSBERGER, P. 1986. Estimating the fractal dimensions and entropies of strange attractors. In: Holden, V. (ed.); *Chaos.* Manchester Univ. Press, Manchester, 302-317.

GUCKENHEIMER, J. and HOLMES, P. 1983. *Nonlinear oscillations, dynamical systems and bifurcations of vector fields.* Springer Verlag, New York, 453 pp.

HAARSMA, R. and OPSTEEGH, J.D. 1988. Barotropic instability of planetary-

scale flow. *J. Atmos. Sci.*, accepted.

HENTCHEL, H.G.E. and PROCACCIA, I. 1983. The infinite number of dimensions of probabilistic fractals and strange attractors. *Physica* **8D,** 435-449.

HESS, P. and BREZOWSKY, H. 1969. *Katalog der Grosswetteranlagen Deutschlands.* Ber. Dtsch. Wetterdienstes 113.

HOLLINGSWORTH, A., ARPE, K., TIEDTKE, M., CAPALDO, M. and SAVIJARVI, H. 1980. The performance of a medium-range forecast model in winter: impact of physical parameterizations. *Mon. Wea. Rev.* **108,** 1736-1773.

HOLLOWAY, G. and WEST, B.J. (eds.) 1984. *Predictability of fluid motions.* Amer. Inst. Phys., New York, 612 pp.

HOSKINS, B.J., JAMES, I.N. and WHITE, G.H. 1983. The shape, propagation and mean-flow interaction of large-scale weather systems. *J. Atmos. Sci.* **40,** 1595-1605.

JARRAUD, M. and BAEDE, A.P.M. 1985. The use of spectral techniques in numerical weather prediction. *Lect. Appl. Math.* **22,** 1-41.

KÄLLÉN, E. 1981. The nonlinear effects of orographic and momentum forcing in a low-order, barotropic model. *J. Atmos. Sci.* **38,** 2150-2163.

KÄLLÉN, E. 1982. Bifurcation properties of quasi-geostropic, barotropic models and their relation to atmospheric blocking. *Tellus* **34,** 255-265.

KÄLLÉN, E. 1983. A note on orographically induced instabilities in two layer models. *J. Atmos. Sci.* **40,** 500-505.

KAPLAN, J.L. and YORKE, J.A. 1979. Chaotic behaviour of multidimensional difference equations. In: PEITGEN, H.O. and WALTHER, H.D. (eds.), *Functional differential equations and approximation of fixed points,* Springer Verlag, Berlin, 204-228.

KELLER, H.B. 1977. Numerical solution of bifurcation and nonlinear eigenvalue problems. In: Rabinowitz, P. H. (ed.), *Applications of bifurcation theory,* Academic Press, New York, 359-384.

KOTTALAM, J., WEST, B.J. and LINDENBERG, K. 1987. Fluctuations and dissipation in multiple flow equilibria. Preprint Univ. of California at San Diego, La Jolla.

KRUSE, H.A. and HASSELMAN, K. 1986. Investigation of processes governing the large-scale variability of the atmosphere using low-order barotropic spectral models as a statistical tool. *Tellus* **38A,** 12-24.

LANGFORD, W.F. 1981. A review of interactions of Hopf and steady-state bifurcations. In: Barenblatt, G. I., Iooss, G. and Joseph, D. D. (eds.); *Nonlinear dynamics and turbulence.* Pitman, New York, 215-237.

LEGRAS, B. and GHIL, M. 1985. Persistent anomalies, blocking and variations in atmospheric predictability. *J. Atmos. Sci.* **42,** 433-471.

LINDENBERG, K. and WEST, B.J. 1984. Fluctuations and dissipation in a barotropic flow field. *J. Atmos. Sci.* **41,** 3021-3031.

LORENZ, E.N. 1963. Deterministic nonperiodic flow. *J. Atmos Sci.* **20,** 130-141.

LORENZ, E.N. 1969a. Three approaches to atmospheric predictability. *Bull. Amer. Meteorol. Soc.* **50,** 345-349.

LORENZ, E.N. 1969b. The predictability of a flow which possesses many scales

of motion. *Tellus* **21,** 289-307.

LUDWIG, D. 1975. Persistence of dynamical systems under random perturbations. *SIAM Rev.* **17,** 605-640.

MATKOWSKY, B.J. and SCHUSS, Z. 1977. The exit problem for randomly perturbed dynamical systems. *SIAM J. Appl. Math.* **33,** 365-382.

MATKOWSKY, B.J., SCHUSS, Z. and TIER, C. 1983. Diffusion across characteristic boundaries with critical points. *SIAM J. Appl. Math.* **43,** 673-695.

MATSUDA, Y. 1983. Classification of critical points and symmetry-breaking in fluid phenomena and its application to dynamic meteorology. *J. Meteorol. Soc. Japan* **61,** 771-788.

MORITZ, R.E. 1984. Predictability and almost intransitivity in a barotropic blocking model. In: Holloway, G. and West, B. J. (eds.), *Predictability of fluid motions,* Americ. Inst. Phys., New York, 419-439.

NAMIAS, J. 1950. The index cycle and its role in the general circulation. J. Meteorol. **7,** 130-139.

OPSTEEGH, J.D. 1988. De voorspelbaarheid van het weer. *Natuur en Techniek,* accepted.

OPSTEEGH, J.D. and VERNEKAR, A.D. 1982. A simulation of the January standing wave pattern including the effect of the transient eddies. *J. Atmos. Sci.* **39,** 734-744.

PALMÉN, E. and NEWTON, C.W. 1969. *Atmospheric circulation systems, their structure and physical interpretation.* Academic Press, New York, 603 pp.

PEDLOSKY, J. 1984. The equations of motion in the ocean. *J. Phys. Oceanogr.* **14,** 448-455.

PEDLOSKY, J. 1987. *Geophysical fluid dynamics,* 2nd edition, Springer Verlag, New York, 710 pp.

PHILLIPS, N.A. 1954. Energy transformations and meridional circulations associated with simple baroclinic waves in a two-level quasi-geostrophic model. *Tellus* **6,** 273-286.

PRIESTLY, M.B. 1981. *Spectral analysis and time series.* Academic Press, London. Volume 1: *univariate series;* volume 2: *multivariate series, prediction and control,* 890 pp.

REINHOLD, B.B. 1987. Weather regimes: the challenge in extended-range forecasting. *Science* **235,** 437-441.

REINHOLD, B.B. and PIERREHUMBERT, R.T. Dynamics of weather regimes: quasi-stationary waves and blocking. *Mon. Wea. Rev.* **110,** 1105-1145.

ROOZEN, H. 1986. Numerical construction of rays and confidence contours in stochastic population dynamics. CWI, Amsterdam, Note AM-N8602.

SCHUSTER, H.G. 1987. *Deterministic chaos, an introduction,* second ed.,Physik Verlag, G. m. b. H., Waldheim, 220 pp.

SALTZMAN, B. 1959. On the maintenance of the large-scale quasi-permanent disturbances of the atmosphere. *Tellus* **11,** 425-431.

SHUTTS, G.J. 1983. Parameterization of travelling weather systems in a simple model of large-scale atmospheric flow. *Adv. in Geophys.* **25,** 117-172.

SILBERMAN, I. 1954. Planetary waves in the atmosphere. *J. Meteorol.* **11,** 27-34.

SILNIKOV, L.P. 1965. A case of the existence of a denumerable set of periodic motions. *Sov. Math. Dokl.* **36,** 163-166.

SPARROW, C. 1982. *The Lorenz equations: bifurcations, chaos and strange attractors.* Springer Verlag, Berlin, 269 pp.

SPEKAT, A., HELLER-SCHULZE, B and LUTZ, M. 1983. 'Grosswetter' circulation analysed by means of Markov chains. *Meteorol. Rdsch.* **36,** 243-248.

TENNEKES, H. 1985. A comparitive pathology of atmospheric turbulence in two and three dimensions. In: Ghil, M., Benzi, R. and Parisi, G. (eds.); *Turbulence and predictability in geophysical fluid dynamics and climate dynamics.* North Holland, Amsterdam, 45-70.

TENNEKES, H., BAEDE, A.P.M. and OPSTEEGH, J.D. 1986. Forecasting forecast skill. In: Proc. ECMWF Workshop *'On predictability in the medium and extended range'*, 17-19 March 1986, ECMWF, Reading, 277-302.

THOMPSON, J.M.T. and STEWART, H.B. 1986. *Nonlinear dynamics and chaos: geometrical methods for engineers and scientists.* Wiley, Chichester, 376 pp.

VAN DIJK, W., SCHMIDT, F.H. and SCHUURMANS, C.J.E. 1974. Beschrijving en toepassingsmogelijkheden van gemiddelde topografieën van het 500 mb-vlak in afhankelijkheid van circulatietypen. KNMI, de Bilt, Wetenschappelijk Rapport WR 74-3.

VAN KAMPEN, N.G. 1985. *Stochastic processes in physics and chemistry,* 4nd edition. North Holland Pu. Co., Amsterdam, 419 pp.

VOIGT, R.G., GOTTLIEB, D. and YOUSOFF-HUSSAINI, M. (eds.) 1984. *Spectral methods for partial differential equations.* SIAM, Philadelphia, 267 pp.

WALLACE, J.M. and BLACKMON, M.L. 1983. Observations of low-frequency atmospheric variability. In: Hoskins, B. J. and Pearce, A. P. (eds.); *Large-scale dynamical processes in the atmosphere.* Academic Press, New York, 55-94.

WHITE, A.A. and GREEN, J.S.A., 1982. A nonlinear atmospheric long wave model incorporating parameterizations of transient baroclinic eddies. *Q. J. R. Meteorol. Soc.* **108,** 55-85.

WOLF, A., SWIFT, J.B., SWINNEY, H.L. and VASTANO, J.A. 1985. Determining Lyapunov exponents from a time series. *Physica* **6D,** 285-317.

YODEN, S. 1985. Bifurcation properties of a quasi-geostrophic, barotropic, low-order model with topography. *J. Meteorol. Soc. Japan* **63,** 535-546.

YODEN, S. and HIROTA, I. 1984. A numerical study on periodic and chaotic behaviour in a geophysical fluid system. In: Tatsumi, T. (ed.); *Turbulence and chaotic phenomena in fluids.* Elsevier Science, Amsterdam, 477-482.

Index

MATHEMATICAL CENTRE TRACTS

1 T. van der Walt. *Fixed and almost fixed points.* 1963.

2 A.R. Bloemena. *Sampling from a graph.* 1964.

3 G. de Leve. *Generalized Markovian decision processes, part I: model and method.* 1964.

4 G. de Leve. *Generalized Markovian decision processes, part II: probabilistic background.* 1964.

5 G. de Leve, H.C. Tijms, P.J. Weeda. *Generalized Markovian decision processes, applications.* 1970.

6 M.A. Maurice. *Compact ordered spaces.* 1964.

7 W.R. van Zwet. *Convex transformations of random variables.* 1964.

8 J.A. Zonneveld. *Automatic numerical integration.* 1964.

9 P.C. Baayen. *Universal morphisms.* 1964.

10 E.M. de Jager. *Applications of distributions in mathematical physics.* 1964.

11 A.B. Paalman-de Miranda. *Topological semigroups.* 1964.

12 J.A.Th.M. van Berckel, H. Brandt Corstius, R.J. Mokken, A. van Wijngaarden. *Formal properties of newspaper Dutch.* 1965.

13 H.A. Lauwerier. *Asymptotic expansions.* 1966, out of print; replaced by MCT 54.

14 H.A. Lauwerier. *Calculus of variations in mathematical physics.* 1966.

15 R. Doornbos. *Slippage tests.* 1966.

16 J.W. de Bakker. *Formal definition of programming languages with an application to the definition of ALGOL 60.* 1967.

17 R.P. van de Riet. *Formula manipulation in ALGOL 60, part 1.* 1968.

18 R.P. van de Riet. *Formula manipulation in ALGOL 60, part 2.* 1968.

19 J. van der Slot. *Some properties related to compactness.* 1968.

20 P.J. van der Houwen. *Finite difference methods for solving partial differential equations.* 1968.

21 E. Wattel. *The compactness operator in set theory and topology.* 1968.

22 T.J. Dekker. *ALGOL 60 procedures in numerical algebra, part 1.* 1968.

23 T.J. Dekker, W. Hoffmann. *ALGOL 60 procedures in numerical algebra, part 2.* 1968.

24 J.W. de Bakker. *Recursive procedures.* 1971.

25 E.R. Paërl. *Representations of the Lorentz group and projective geometry.* 1969.

26 European Meeting 1968. *Selected statistical papers, part I.* 1968.

27 European Meeting 1968. *Selected statistical papers, part II.* 1968.

28 J. Oosterhoff. *Combination of one-sided statistical tests.* 1969.

29 J. Verhoeff. *Error detecting decimal codes.* 1969.

30 H. Brandt Corstius. *Exercises in computational linguistics.* 1970.

31 W. Molenaar. *Approximations to the Poisson, binomial and hypergeometric distribution functions.* 1970.

32 L. de Haan. *On regular variation and its application to the weak convergence of sample extremes.* 1970.

33 F.W. Steutel. *Preservation of infinite divisibility under mixing and related topics.* 1970.

34 I. Juhász, A. Verbeek, N.S. Kroonenberg. *Cardinal functions in topology.* 1971.

35 M.H. van Emden. *An analysis of complexity.* 1971.

36 J. Grasman. *On the birth of boundary layers.* 1971.

37 J.W. de Bakker, G.A. Blaauw, A.J.W. Duijvestijn, E.W. Dijkstra, P.J. van der Houwen, G.A.M. Kamsteeg-Kemper, F.E.J. Kruseman Aretz, W.L. van der Poel, J.P. Schaap-Kruseman, M.V. Wilkes, G. Zoutendijk. *MC-25 Informatica Symposium.* 1971.

38 W.A. Verloren van Themaat. *Automatic analysis of Dutch compound words.* 1972.

39 H. Bavinck. *Jacobi series and approximation.* 1972.

40 H.C. Tijms. *Analysis of (s,S) inventory models.* 1972.

41 A. Verbeek. *Superextensions of topological spaces.* 1972.

42 W. Vervaat. *Success epochs in Bernoulli trials (with applications in number theory).* 1972.

43 F.H. Ruymgaart. *Asymptotic theory of rank tests for independence.* 1973.

44 H. Bart. *Meromorphic operator valued functions.* 1973.

45 A.A. Balkema. *Monotone transformations and limit laws.* 1973.

46 R.P. van de Riet. *ABC ALGOL, a portable language for formula manipulation systems, part 1: the language.* 1973.

47 R.P. van de Riet. *ABC ALGOL, a portable language for formula manipulation systems, part 2: the compiler.* 1973.

48 F.E.J. Kruseman Aretz, P.J.W. ten Hagen, H.L. Oudshoorn. *An ALGOL 60 compiler in ALGOL 60, text of the MC-compiler for the EL-X8.* 1973.

49 H. Kok. *Connected orderable spaces.* 1974.

50 A. van Wijngaarden, B.J. Mailloux, J.E.L. Peck, C.H.A. Koster, M. Sintzoff, C.H. Lindsey, L.G.L.T. Meertens, R.G. Fisker (eds.). *Revised report on the algorithmic language ALGOL 68.* 1976.

51 A. Hordijk. *Dynamic programming and Markov potential theory.* 1974.

52 P.C. Baayen (ed.). *Topological structures.* 1974.

53 M.J. Faber. *Metrizability in generalized ordered spaces.* 1974.

54 H.A. Lauwerier. *Asymptotic analysis, part 1.* 1974.

55 M. Hall, Jr., J.H. van Lint (eds.). *Combinatorics, part 1: theory of designs, finite geometry and coding theory.* 1974.

56 M. Hall, Jr., J.H. van Lint (eds.). *Combinatorics, part 2: graph theory, foundations, partitions and combinatorial geometry.* 1974.

57 M. Hall, Jr., J.H. van Lint (eds.). *Combinatorics, part 3: combinatorial group theory.* 1974.

58 W. Albers. *Asymptotic expansions and the deficiency concept in statistics.* 1975.

59 J.L. Mijnheer. *Sample path properties of stable processes.* 1975.

60 F. Göbel. *Queueing models involving buffers.* 1975.

63 J.W. de Bakker (ed.). *Foundations of computer science.* 1975.

64 W.J. de Schipper. *Symmetric closed categories.* 1975.

65 J. de Vries. *Topological transformation groups, 1: a categorical approach.* 1975.

66 H.G.J. Pijls. *Logically convex algebras in spectral theory and eigenfunction expansions.* 1976.

68 P.P.N. de Groen. *Singularly perturbed differential operators of second order.* 1976.

69 J.K. Lenstra. *Sequencing by enumerative methods.* 1977.

70 W.P. de Roever, Jr. *Recursive program schemes: semantics and proof theory.* 1976.

71 J.A.E.E. van Nunen. *Contracting Markov decision processes.* 1976.

72 J.K.M. Jansen. *Simple periodic and non-periodic Lamé functions and their applications in the theory of conical waveguides.* 1977.

73 D.M.R. Leivant. *Absoluteness of intuitionistic logic.* 1979.

74 H.J.J. te Riele. *A theoretical and computational study of generalized aliquot sequences.* 1976.

75 A.E. Brouwer. *Treelike spaces and related connected topological spaces.* 1977.

76 M. Rem. *Associons and the closure statement.* 1976.

77 W.C.M. Kallenberg. *Asymptotic optimality of likelihood ratio tests in exponential families.* 1978.

78 E. de Jonge, A.C.M. van Rooij. *Introduction to Riesz spaces.* 1977.

79 M.C.A. van Zuijlen. *Emperical distributions and rank statistics.* 1977.

80 P.W. Hemker. *A numerical study of stiff two-point boundary problems.* 1977.

81 K.R. Apt, J.W. de Bakker (eds.). *Foundations of computer science II, part 1.* 1976.

82 K.R. Apt, J.W. de Bakker (eds.). *Foundations of computer science II, part 2.* 1976.

83 L.S. van Benthem Jutting. *Checking Landau's "Grundlagen" in the AUTOMATH system.* 1979.

84 H.L.L. Busard. *The translation of the elements of Euclid from the Arabic into Latin by Hermann of Carinthia (?), books vii-xii.* 1977.

85 J. van Mill. *Supercompactness and Wallman spaces.* 1977.

86 S.G. van der Meulen, M. Veldhorst. *Torrix I, a programming system for operations on vectors and matrices over arbitrary fields and of variable size.* 1978.

88 A. Schrijver. *Matroids and linking systems.* 1977.

89 J.W. de Roever. *Complex Fourier transformation and analytic functionals with unbounded carriers.* 1978.

90 L.P.J. Groenewegen. *Characterization of optimal strategies in dynamic games.* 1981.

91 J.M. Geysel. *Transcendence in fields of positive characteristic.* 1979.

92 P.J. Weeda. *Finite generalized Markov programming.* 1979.

93 H.C. Tijms, J. Wessels (eds.). *Markov decision theory.* 1977.

94 A. Bijlsma. *Simultaneous approximations in transcendental number theory.* 1978.

95 K.M. van Hee. *Bayesian control of Markov chains.* 1978.

96 P.M.B. Vitányi. *Lindenmayer systems: structure, languages, and growth functions.* 1980.

97 A. Federgruen. *Markovian control problems; functional equations and algorithms.* 1984.

98 R. Geel. *Singular perturbations of hyperbolic type.* 1978.

99 J.K. Lenstra, A.H.G. Rinnooy Kan, P. van Emde Boas (eds.). *Interfaces between computer science and operations research.* 1978.

100 P.C. Baayen, D. van Dulst, J. Oosterhoff (eds.). *Proceedings bicentennial congress of the Wiskundig Genootschap, part 1.* 1979.

101 P.C. Baayen, D. van Dulst, J. Oosterhoff (eds.). *Proceedings bicentennial congress of the Wiskundig Genootschap, part 2.* 1979.

102 D. van Dulst. *Reflexive and superreflexive Banach spaces.* 1978.

103 K. van Harn. *Classifying infinitely divisible distributions by functional equations.* 1978.

104 J.M. van Wouwe. *Go-spaces and generalizations of metrizability.* 1979.

105 R. Helmers. *Edgeworth expansions for linear combinations of order statistics.* 1982.

106 A. Schrijver (ed.). *Packing and covering in combinatorics.* 1979.

107 C. den Heijer. *The numerical solution of nonlinear operator equations by imbedding methods.* 1979.

108 J.W. de Bakker, J. van Leeuwen (eds.). *Foundations of computer science III, part 1.* 1979.

109 J.W. de Bakker, J. van Leeuwen (eds.). *Foundations of computer science III, part 2.* 1979.

110 J.C. van Vliet. *ALGOL 68 transput, part I: historical review and discussion of the implementation model.* 1979.

111 J.C. van Vliet. *ALGOL 68 transput, part II: an implementation model.* 1979.

112 H.C.P. Berbee. *Random walks with stationary increments and renewal theory.* 1979.

113 T.A.B. Snijders. *Asymptotic optimality theory for testing problems with restricted alternatives.* 1979.

114 A.J.E.M. Janssen. *Application of the Wigner distribution to harmonic analysis of generalized stochastic processes.* 1979.

115 P.C. Baayen, J. van Mill (eds.). *Topological structures II, part 1.* 1979.

116 P.C. Baayen, J. van Mill (eds.). *Topological structures II, part 2.* 1979.

117 P.J.M. Kallenberg. *Branching processes with continuous state space.* 1979.

118 P. Groeneboom. *Large deviations and asymptotic efficiencies.* 1980.

119 F.J. Peters. *Sparse matrices and substructures, with a novel implementation of finite element algorithms.* 1980.

120 W.P.M. de Ruyter. *On the asymptotic analysis of large-scale ocean circulation.* 1980.

121 W.H. Haemers. *Eigenvalue techniques in design and graph theory.* 1980.

122 J.C.P. Bus. *Numerical solution of systems of nonlinear equations.* 1980.

123 I. Yuhász. *Cardinal functions in topology - ten years later.* 1980.

124 R.D. Gill. *Censoring and stochastic integrals.* 1980.

125 R. Eising. *2-D systems, an algebraic approach.* 1980.

126 G. van der Hoek. *Reduction methods in nonlinear programming.* 1980.

127 J.W. Klop. *Combinatory reduction systems.* 1980.

128 A.J.J. Talman. *Variable dimension fixed point algorithms and triangulations.* 1980.

129 G. van der Laan. *Simplicial fixed point algorithms.* 1980.

130 P.J.W. ten Hagen, T. Hagen, P. Klint, H. Noot, H.J. Sint, A.H. Veen. *ILP: intermediate language for pictures.* 1980.

131 R.J.R. Back. *Correctness preserving program refinements: proof theory and applications.* 1980.

132 H.M. Mulder. *The interval function of a graph.* 1980.

133 C.A.J. Klaassen. *Statistical performance of location estimators.* 1981.

134 J.C. van Vliet, H. Wupper (eds.). *Proceedings international conference on ALGOL 68.* 1981.

135 J.A.G. Groenendijk, T.M.V. Janssen, M.J.B. Stokhof (eds.). *Formal methods in the study of language, part I.* 1981.

136 J.A.G. Groenendijk, T.M.V. Janssen, M.J.B. Stokhof (eds.). *Formal methods in the study of language, part II.* 1981.

137 J. Telgen. *Redundancy and linear programs.* 1981.

138 H.A. Lauwerier. *Mathematical models of epidemics.* 1981.

139 J. van der Wal. *Stochastic dynamic programming, successive approximations and nearly optimal strategies for Markov decision processes and Markov games.* 1981.

140 J.H. van Geldrop. *A mathematical theory of pure exchange economies without the no-critical-point hypothesis.* 1981.

141 G.E. Welters. *Abel-Jacobi isogenies for certain types of Fano threefolds.* 1981.

142 H.R. Bennett, D.J. Lutzer (eds.). *Topology and order structures, part 1.* 1981.

143 J.M. Schumacher. *Dynamic feedback in finite- and infinite-dimensional linear systems.* 1981.

144 P. Eijgenraam. *The solution of initial value problems using interval arithmetic; formulation and analysis of an algorithm.* 1981.

145 A.J. Brentjes. *Multi-dimensional continued fraction algorithms.* 1981.

146 C.V.M. van der Mee. *Semigroup and factorization methods in transport theory.* 1981.

147 H.H. Tigelaar. *Identification and informative sample size.* 1982.

148 L.C.M. Kallenberg. *Linear programming and finite Markovian control problems.* 1983.

149 C.B. Huijsmans, M.A. Kaashoek, W.A.J. Luxemburg, W.K. Vietsch (eds.). *From A to Z, proceedings of a symposium in honour of A.C. Zaanen.* 1982.

150 M. Veldhorst. *An analysis of sparse matrix storage schemes.* 1982.

151 R.J.M.M. Does. *Higher order asymptotics for simple linear rank statistics.* 1982.

152 G.F. van der Hoeven. *Projections of lawless sequences.* 1982.

153 J.P.C. Blanc. *Application of the theory of boundary value problems in the analysis of a queueing model with paired services.* 1982.

154 H.W. Lenstra, Jr., R. Tijdeman (eds.). *Computational methods in number theory, part I.* 1982.

155 H.W. Lenstra, Jr., R. Tijdeman (eds.). *Computational methods in number theory, part II.* 1982.

156 P.M.G. Apers. *Query processing and data allocation in distributed database systems.* 1983.

157 H.A.W.M. Kneppers. *The covariant classification of two-dimensional smooth commutative formal groups over an algebraically closed field of positive characteristic.* 1983.

158 J.W. de Bakker, J. van Leeuwen (eds.). *Foundations of computer science IV, distributed systems, part 1.* 1983.

159 J.W. de Bakker, J. van Leeuwen (eds.). *Foundations of computer science IV, distributed systems, part 2.* 1983.

160 A. Rezus. *Abstract AUTOMATH.* 1983.

161 G.F. Helminck. *Eisenstein series on the metaplectic group, an algebraic approach.* 1983.

162 J.J. Dik. *Tests for preference.* 1983.

163 H. Schippers. *Multiple grid methods for equations of the second kind with applications in fluid mechanics.* 1983.

164 F.A. van der Duyn Schouten. *Markov decision processes with continuous time parameter.* 1983.

165 P.C.T. van der Hoeven. *On point processes.* 1983.

166 H.B.M. Jonkers. *Abstraction, specification and implementation techniques, with an application to garbage collection.* 1983.

167 W.H.M. Zijm. *Nonnegative matrices in dynamic programming.* 1983.

168 J.H. Evertse. *Upper bounds for the numbers of solutions of diophantine equations.* 1983.

169 H.R. Bennett, D.J. Lutzer (eds.). *Topology and order structures, part 2.* 1983.

CWI TRACTS

1 D.H.J. Epema. *Surfaces with canonical hyperplane sections.* 1984.

2 J.J. Dijkstra. *Fake topological Hilbert spaces and characterizations of dimension in terms of negligibility.* 1984.

3 A.J. van der Schaft. *System theoretic descriptions of physical systems.* 1984.

4 J. Koene. *Minimal cost flow in processing networks, a primal approach.* 1984.

5 B. Hoogenboom. *Intertwining functions on compact Lie groups.* 1984.

6 A.P.W. Böhm. *Dataflow computation.* 1984.

7 A. Blokhuis. *Few-distance sets.* 1984.

8 M.H. van Hoorn. *Algorithms and approximations for queueing systems.* 1984.

9 C.P.J. Koymans. *Models of the lambda calculus.* 1984.

10 C.G. van der Laan, N.M. Temme. *Calculation of special functions: the gamma function, the exponential integrals and error-like functions.* 1984.

11 N.M. van Dijk. *Controlled Markov processes; time-discretization.* 1984.

12 W.H. Hundsdorfer. *The numerical solution of nonlinear stiff initial value problems: an analysis of one step methods.* 1985.

13 D. Grune. *On the design of ALEPH.* 1985.

14 J.G.F. Thiemann. *Analytic spaces and dynamic programming: a measure theoretic approach.* 1985.

15 F.J. van der Linden. *Euclidean rings with two infinite primes.* 1985.

16 R.J.P. Groothuizen. *Mixed elliptic-hyperbolic partial differential operators: a case-study in Fourier integral operators.* 1985.

17 H.M.M. ten Eikelder. *Symmetries for dynamical and Hamiltonian systems.* 1985.

18 A.D.M. Kester. *Some large deviation results in statistics.* 1985.

19 T.M.V. Janssen. *Foundations and applications of Montague grammar, part 1: Philosophy, framework, computer science.* 1986.

20 B.F. Schriever. *Order dependence.* 1986.

21 D.P. van der Vecht. *Inequalities for stopped Brownian motion.* 1986.

22 J.C.S.P. van der Woude. *Topological dynamix.* 1986.

23 A.F. Monna. *Methods, concepts and ideas in mathematics: aspects of an evolution.* 1986.

24 J.C.M. Baeten. *Filters and ultrafilters over definable subsets of admissible ordinals.* 1986.

25 A.W.J. Kolen. *Tree network and planar rectilinear location theory.* 1986.

26 A.H. Veen. *The misconstrued semicolon: Reconciling imperative languages and dataflow machines.* 1986.

27 A.J.M. van Engelen. *Homogeneous zero-dimensional absolute Borel sets.* 1986.

28 T.M.V. Janssen. *Foundations and applications of Montague grammar, part 2: Applications to natural language.* 1986.

29 H.L. Trentelman. *Almost invariant subspaces and high gain feedback.* 1986.

30 A.G. de Kok. *Production-inventory control models: approximations and algorithms.* 1987.

31 E.E.M. van Berkum. *Optimal paired comparison designs for factorial experiments.* 1987.

32 J.H.J. Einmahl. *Multivariate empirical processes.* 1987.

33 O.J. Vrieze. *Stochastic games with finite state and action spaces.* 1987.

34 P.H.M. Kersten. *Infinitesimal symmetries: a computational approach.* 1987.

35 M.L. Eaton. *Lectures on topics in probability inequalities.* 1987.

36 A.H.P. van der Burgh, R.M.M. Mattheij (eds.). *Proceedings of the first international conference on industrial and applied mathematics (ICIAM 87).* 1987.

37 L. Stougie. *Design and analysis of algorithms for stochastic integer programming.* 1987.

38 J.B.G. Frenk. *On Banach algebras, renewal measures and regenerative processes.* 1987.

39 H.J.M. Peters, O.J. Vrieze (eds.). *Surveys in game theory and related topics.* 1987.

40 J.L. Geluk, L. de Haan. *Regular variation, extensions and Tauberian theorems.* 1987.

41 Sape J. Mullender (ed.). *The Amoeba distributed operating system: Selected papers 1984-1987.* 1987.

42 P.R.J. Asveld, A. Nijholt (eds.). *Essays on concepts, formalisms, and tools.* 1987.

43 H.L. Bodlaender. *Distributed computing: structure and complexity.* 1987.

44 A.W. van der Vaart. *Statistical estimation in large parameter spaces.* 1988.

45 S.A. van de Geer. *Regression analysis and empirical processes.* 1988.

46 S.P. Spekreijse. *Multigrid solution of the steady Euler equations.* 1988.

47 J.B. Dijkstra. *Analysis of means in some non-standard situations.* 1988.

48 F.C. Drost. *Asymptotics for generalized chi-square goodness-of-fit tests.* 1988.

49 F.W. Wubs. *Numerical solution of the shallow-water equations.* 1988.

50 F. de Kerf. *Asymptotic analysis of a class of perturbed Korteweg-de Vries initial value problems.* 1988.

51 P.J.M. van Laarhoven. *Theoretical and computational aspects of simulated annealing.* 1988.

52 P.M. van Loon. *Continuous decoupling transformations for linear boundary value problems.* 1988.

53 K.C.P. Machielsen. *Numerical solution of optimal control problems with state constraints by sequential quadratic programming in function space.* 1988.

54 L.C.R.J. Willenborg. *Computational aspects of survey data processing.* 1988.

55 G.J. van der Steen. *A program generator for recognition, parsing and transduction with syntactic patterns.* 1988.

56 J.C. Ebergen. *Translating programs into delay-insensitive circuits.* 1989.

57 S.M. Verduyn Lunel. *Exponential type calculus for linear delay equations.* 1989.

58 M.C.M. de Gunst. *A random model for plant cell population growth.* 1989.

59 D. van Dulst. *Characterizations of Banach spaces not containing l^1.* 1989.

60 H.E. de Swart. *Vacillation and predictability properties of low-order atmospheric spectral models.* 1989.